A Handheld Dual Particle Imager for Imaging and Characterizing Special Nuclear Material

by

William M. Steinberger

A dissertation submitted in partial fulfillment
of the requirements for the degree of
Doctor of Philosophy
(Nuclear Engineering and Radiological Sciences)
in The University of Michigan
2021

Doctoral Committee:

Professor Sara A. Pozzi, Chair
Professor Jeffrey A. Fessler
Professor Igor Jovanovic
Dr. Peter Marleau, Sandia National Laboratories

William M. Steinberger

wmst@umich.edu

ORCID iD: 0000-0002-8293-5701

To my grandmother, Vera Zubko (Baba).

ACKNOWLEDGEMENTS

Colossians 3: 16-17

"16 Let the word of Christ dwell in you richly in all wisdom; teaching and admonishing one another in psalms and hymns and spiritual songs, singing with grace in your hearts to the Lord.

17 And whatsoever ye do in word or deed, do all in the name of the Lord Jesus, giving thanks to God and the Father by him."

First and foremost, I would like to thank Professor Pozzi for bringing me on as part of the Detection for Nuclear Nonproliferation Group (DNNG). The opportunities I've had under this group have been incredible and you've set up a fantastic network for students to learn and become a part of the nuclear nonproliferation community. Thank you so much for supporting me and letting me be a part of it! I'd also like to thank the rest of DNNG for their help and support. Dr. Clarke has been a great mentor through this research, and my writing abilities have greatly improved under his guidance. Special thanks as well to Nathan Giha, Chris Meert and Stefano Marin for their contributions to this project.

Special thanks as well to Dr. Marleau. Thank you for being part of my committee and helping guide and focus this research. I would also like to thank Professor Jovanovic and Professor Fessler. I greatly appreciate you taking your time to serve on my committee.

Mom, Dad, Jay, Uncle Billy, Aunt Kathy, I couldn't have done this without your support and help along the way! Thank you! To my friends who have listened to me

talk about this research nonstop for the past five years, thank you for listening and your support!

I also want to thank the sponsors. This work was funded in-part by the Consortium for Verification Technology under Department of Energy National Nuclear Security Administration award number DE-NA0002534 and the Department of Defense, Defense Threat Reduction Agency under contract number HDTRA117C0046. Any opinions, findings and conclusions or recommendations expressed in this material are those of the author(s) and do not necessarily reflect the views of the Defense Threat Reduction Agency or other funding organizations.

TABLE OF CONTENTS

LIST OF FIGURES

Figure

LIST OF TABLES

Table

ABSTRACT

Localizing and monitoring sources of radiation is a difficult problem for national security and nuclear safeguard applications. Terrorists attempting to accumulate nuclear materials will most likely hide them in remote or entrenched locations where large or heavy detector systems cannot practically be deployed. Inspectors attempting to monitor or verify the location of a source may also be constrained in the size and weight of a detector they can deploy in a facility. Current deployed detectors typically measure relative count or dose rates to localize or verify a source; this approach requires the user to go near a source to begin to determine its location. These detectors can be subject to fluctuations in background radiation due to natural fluctuations, the surrounding environment, or potential shielding around a source that may cause it to not follow a $1/r^2$ trend. Imaging systems such as neutron scatter cameras (NSCs) or Compton cameras can be used to localize a source much faster than current simplistic systems because they are not subject to background in the same manner. However, these imaging systems are prohibitively large or heavy due to cooling systems, battery systems or multiple photomultiplier tubes (PMTs). Using silicon photomultipliers (SiPMs) in place of PMTs, however, can greatly reduce the size of a scintillator-based imaging system since SiPMs are much more compact and are comparable photodetectors. A handheld dual-particle imager (H2DPI) composed of twelve stilbene pillars (6x6x50.5 mm^3) and eight $CeBr_3$ cylinders coupled to J-Series SensL SiPMs has been designed and built. The H2DPI localizes neutron sources by reconstructing double-scatter neutron events between stilbene pillars and localizes gamma-ray sources by reconstructing gamma-ray double-scatter events be-

tween stilbene pillars and $CeBr_3$ cylinders. This Compton imaging methodology has been shown to be able to localize and identify special nuclear material sources such as highly enriched uranium and plutonium when both sources are in the same field of view. The neutron imaging capability also enables for neutron spectroscopy. The H2DPI is capable of isolating and identifying the (α,n) spectrum emitted by a PuBe source from the Watt spectrum emitted by a ^{252}Cf source. Characterization that was used to accurately reconstruct sources was also applied to a simulated model of fully-realized system composed of 64-pillars of stilbene coupled to J-series SensL SiPMs. Simulations were validated and it was found that the intrinsic neutron efficiency of a fully-realized system would be 0.94-1.25 % depending on the orientation of the stilbene crystals.

CHAPTER I

Introduction

1.1 Motivation

Discovery of nuclear fission in 1939 opened a new area of research to the physics community to better understand the structure and nature of the nucleus. Application of this new-found understanding and the energy released during fission quickly lead to its weaponization and the first nuclear weapons test in 1945. Proliferation of this technology came relatively quickly due to the magnitude of devastation from these weapons [5]. This proliferation escalated tensions between nations, but has since created a kind of stability with the further refinement of deterrence policies. Along with deterrence policies, treaties such as the Treaty on the Non-Proliferation of Nuclear Weapons [6] and the New Strategic Arms Reduction Treaty [7] have aided in further transparency and stability between nation states by limiting the spread of nuclear weapons and reducing the number of nuclear weapons. There is concern, however, over the peaceful use of nuclear technology, and the possibility of special nuclear materials (SNM), materials capable of being used to produce a nuclear explosion, being acquired and used by non-state actors. SNMs are highly regulated and monitored by organizations such as the International Atomic Energy Agency, which has the mission to promote and monitor the safe, secure and peaceful use of nuclear technologies [8]. The ability to ensure the safeguarding, verification and quantification of radioac-

tive materials is paramount to these kinds of organizations. A key component to accomplish these tasks is nondestructive assay (NDA). NDA includes instrumentation and analysis techniques that provide accurate identification or quantification of nuclear materials [9]. This thesis will analyze the development and application of a detector system to further increase the monitoring, characterization, and localization capabilities of deploy-able detector systems.

1.2 Neutron and Gamma-Ray Detection and Imaging

Radioactive decay is the process in which an unstable nucleus releases energy by the emission of radiation. This radiation comes in predominantly four forms: alpha particles, beta particles, photons, and neutrons. Both alpha and beta particles are charged particles that generally do not have ranges that transport them significantly out of a radioactive source. Neutrons and photons, however, are not charged particles and have much greater penetrating power. Radioactive materials tend to emit characteristic gamma rays that can be used to identify a particular radioisotope. Gamma-ray detection can then be a useful tool for the identification of a radioactive source. The majority of background radiation, however, is composed of photons and photons can be shielded by dense materials with a high atomic number such as lead or tungsten. Neutrons are not typically emitted by natural radioactive materials and the majority of background neutrons are produced from cosmic ray showers in the upper atmosphere [10, 11]. A key property of SNM is that it emits neutrons and gamma rays, either passively or when actively interrogated [12]. Thus, detecting neutrons above a low and reasonably understood background can be a strong indicator of the presence of SNM.

Neutron detection has been traditionally performed with ^{3}He proportional counter tubes surrounded by polyethylene or some other kind of moderator [9]. These types of detectors work well since the thermal-neutron capture cross section is very high.

However, these gas systems require high voltage, are bulky, and were recently limited due to a shortage of ^{3}He [13, 14]. This shortage prompted research into alternative neutron-detection systems. Particular advancements were made in the development of pulse shape discrimination (PSD) capable organic scintillators. These are scintillators that can differentiate between a neutron and gamma-ray interaction [15, 16, 17, 18]. These types of scintillators were developed early on in instrumentation development [19, 20, 21], but have come to prominence due to the ^{3}He shortage and refinement of the application of fast-neutron detectors. Thermal-neutron detectors require neutrons to be moderated prior to detection, which reduces the timing information capable of being acquired and energy information. This information can be particularly useful for source identification and fast-neutron imaging.

Once a source is detected, it can be useful to discern the exact location of the source. Inspectors could use this capability to verify the location of a source in a safeguards scenario or emergency responders and war-fighters could use this capability to isolate a source. Several types of neutron imagers have been developed to accomplish this task, including coded-aperture imagers [22, 23], time-encoded imagers [24], and neutron scatter cameras (NSCs) [25, 26, 27, 28, 29, 30, 31]. NSCs can be made significantly more compact and lighter than coded aperture or time-encoded imagers because no attenuating material or moving parts are necessary [32]. Previously designed scatter-based imaging systems, however, have not been particularly deployable due to their large size and the space occupied by PMTs [33, 34, 31]. The following section will discuss the application of SiPMs as a an alternative to PMTs.

1.3 Application of Silicon Photomultipliers

Scatter-based radiation imaging systems have shown to be effective tools to localize sources of radiation. Compton cameras localize gamma-ray emitting sources by reconstructing the scattering angle of gamma-ray double-scatter events that undergo

Compton scattering and then photoelectric absorption. These types of cameras are typically made from higher-density non-organic materials [35, 36, 37, 38]. NSCs localize neutron sources by measuring and comparing the time-of-flight (TOF) energy of a neutron double-scatter interaction with the total measured energy of the incident neutron [25, 26, 27, 29, 30]. NSCs are typically composed of organic materials that allow for significant amounts of neutron elastic-scattering off hydrogen. A system capable of imaging both types of particles is of particular interest to nonproliferation, nuclear safeguards and emergency response scenarios where the detection or monitoring of SNM is paramount. Systems such as the Dual Particle Imager [39, 33, 40] and the Neutron Spectroscope Instrument [31] are combined Compton cameras and NSCs that have been shown to isolate and identify various sources of radiation in the same field of view. These systems, however, are quite large and bulky due to the use of PMTs and the necessary neutron flight paths. One could be installed in a facility for a monitoring application or deployed on a truck in a search scenario, but these scenarios would require the logistics to be available for the given application.

SiPMs or microchannel plate photomultipliers (MCP-PMs) have shown to be comparable to traditional PMTs for detection of scintillation light, time resolution and PSD capability [41, 42, 43, 44]. SiPMs have additional benefits over traditional PMTs: they are significantly more compact, negligibly affected by external magnetic fields, and have a low operating voltage. A compact system, preferably human-portable, allows for ease of deployment, and there has been significant research to develop such a system for nuclear security applications [44, 45, 46, 47, 48]. This dissertation will build upon previous research to determine the feasibility of a compact scatter-based imaging system.

1.4 Contributions to this Work

The goal of this dissertation was to assess the feasibility of a handheld dual-particle imager (H2DPI) composed of organic and inorganic scintillators coupled to SiPMs. This assessment was completed by demonstrating imaging capabilities with an initial prototype system composed only of organic scintillators coupled to SiPMs. Results of this system are detailed in Steinberger et al. [49] and demonstrate localization of kilogram-quantities of SNM by neutron and gamma-ray imaging. While this initial prototype was capable of reconstructing single gamma-ray sources, it lacked spectroscopic capabilities and the ability to accurately reconstruct multiple gamma-ray emitting sources in the same field of view.

To improve the gamma-ray imaging capabilities, inorganic scintillators were incorporated into the design of the system. Rigorous testing and analysis was performed to determine which scintillator to incorporate. This testing culminated in the analysis of two miniaturized Compton cameras that yielded a clear choice for the scintillator to incorporate. The placement of these inorganic scintillators was then optimized using a structural similarity processing technique on simulated designs to converge on the layout of an upgraded prototype system [50]. This optimized prototype H2DPI was built and tested. Neutron imaging and spectroscopic capabilities were assessed and results show that the system is capable of imaging and differentiating a Watt spectrum from an (α,n) spectrum emitted by a PuBe source with both sources in the same field of view. Gamma-ray imaging of special nuclear material was also demonstrated. The optimized prototype H2DPI was able to passively image the gamma-rays emitted by two SNM sources in the same field of view: highly-enriched uranium (HEU) and weapons-grade plutonium.

Simulations of the H2DPI were further refined by significant characterization of the system [51]. Experimental results were incorporated into simulations to produce validated simulation models. Validated simulation models were then applied to a

simulated fully-realized system to determine the intrinsic efficiencies of such a system. Results of this simulation work yielded a neutron intrinsic imaging efficiency of 0.94-1.25 % depending on the crystal orientation of the stilbene scintillators.

1.5 Thesis Overview

Chapter II discusses the initial prototype H2DPI that was characterized and used to image neutrons and gamma-rays emitted by kilogram quantities of SNM. This chapter also introduces the scatter-based imaging techniques used for source localization. Chapter III further breaks down scatter-based imaging to better understand the point-spread functions obtained from the initial prototype and the mechanisms that contribute to the images. Chapter IV details the methodology applied to choose an inorganic scintillator to incorporate into the design as well as the optimization technique that was used to converge on an optimized prototype design. The optimized system was then thoroughly characterized, which is detailed in Chapter V. Once characterized, the system was tested with various source configurations and types of sources. Results of these tests are included in Chapter VI. The characterization data was then applied to simulations in Chapter VII to assess the feasibility of a fully realized system. Finally, Chapter VIII provides final remarks and suggestions for future research on the characterization and development of compact imaging systems.

CHAPTER II

Imaging SNM with an 8-Pillar H2DPI

2.1 The Initial H2DPI

Three aspects are required to create a compact NSC: small photo-detectors, sufficient time resolution between interactions and low-power photo-detectors so that a cooling system is not required. To assess the feasibility of a compact imaging system, substantial research was performed using stilbene organic scintillators coupled to SiPMs to develop a NSC. This research did not focus on the development of compact electronics or data acquisition systems for such a system. SiPMs have recently become a viable choice as a compact and low-voltage photo-detector for scintillation light [41]. Stilbene could be used for the active volume of a NSC because it has high light-output relative to other hydrogenous scintillators, and can achieve PSD at lower energies compared to other hydrogenous scintillators [15, 16]. Testing also demonstrated that stilbene crystals coupled to SensL C-Series SiPMs have sufficient time resolution (280 ps standard deviation) and PSD capability to be used in a NSC [43, 42]. In addition, an average position resolution of 4.9 mm along the length of a $6\times6\times50$ mm^3 pillar of stilbene was achieved in previous work by reading out both ends of the pillar using SiPMs [52]. Utilizing pillars of scintillator with position resolution capability across the pillar allows for increased overall efficiency of a system without adding additional channels or more smaller scintillators. Encouraged from

these measurements and guided by MCNPX-PoliMi simulations [53], a prototype eight-pillar system was designed, constructed and tested (Figure 2.1).

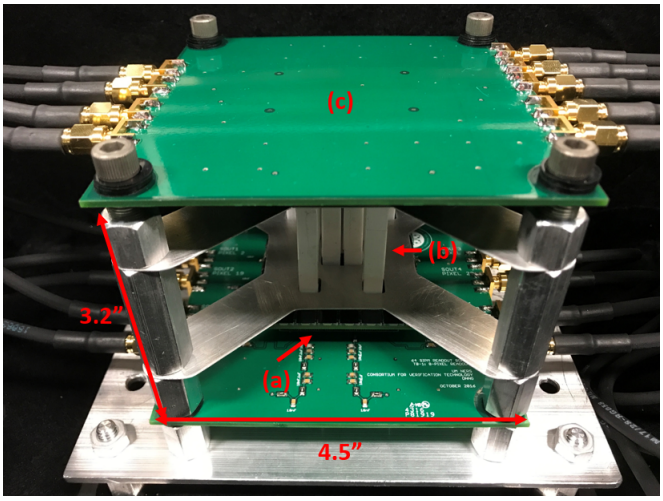

Figure 2.1: Photograph of the prototype handheld dual-particle imager composed of (a) two SensL C-Series SiPM arrays, (b) eight stilbene pillars wrapped in polytetrafluoroethylene tape and (c) two custom printed circuit boards [1].

Eight pillars of Inrad Optics stilbene with dimensions of $6\times6\times50$ mm^3 were coupled on both ends to two arrays of ArrayC-60035-64P-PCB SensL SiPMs [54] using $6\times6\times1$ mm^3 EJ-560 optical interfaces [55]. The layout of the pillars is shown in Figure 2.2 and was based on an optimized configuration detailed by Ruch [32]. Custom electronics were developed to apply voltage bias and passively break out the signals from the SiPM arrays. Each SiPM array is electronically coupled to a custom circuit board, which provides voltage bias to every relevant pixel and passively reads out the signals. The circuit is entirely passive and relatively simple. A negative voltage bias is applied at the anode of each SiPM pixel while the cathode is referenced to ground. The signal from the SiPM is then read out to a v1730 CAEN digitizer with a 14 bit resolution, 2.0 V dynamic range, and 500 MHz digitization rate. A low-pass RC filter was implemented to attenuate any low frequency noise from the bias supply. A shunt resistance of $1k\Omega$ was chosen in accordance with the recommended design from the manufacturer. The following section details results from this prototype system,

demonstrating neutron and gamma-ray imaging capability with in-lab sources and kilogram-quantities of SNM.

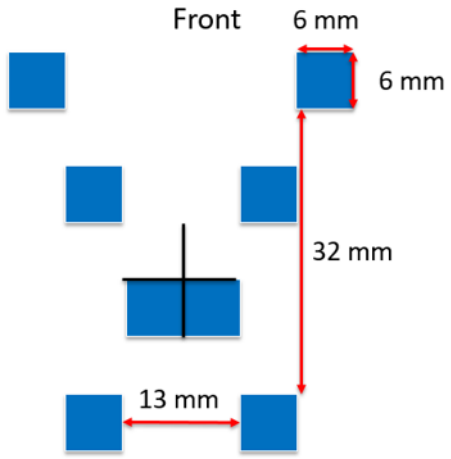

Figure 2.2: Layout of the stilbene pillars on the SiPM array.

2.2 Neutron Imaging

NSCs function by using the subset of interactions in which a neutron scatters twice in the system between two independent volumes. A depiction of a neutron double-scatter interaction is shown in Figure 2.3. The scattering angle between the first interaction and the point of origin is derived by the kinematics of the multiple elastic scatters on hydrogen. If the time resolution is insufficient to resolve coincident interactions, then the sequencing of those interactions between the two independent volumes will have significant associated uncertainty with regards to which interaction happened first [56]. Incorrectly sequencing the interactions will cause the kinematic reconstruction to point in the wrong direction, ultimately producing artifacts in the images. The energy of the neutron after the first interaction is determined by the time-of-flight (TOF) between interactions, or E_{TOF}. E_{TOF} is derived by the velocity as determined by the distance and time between the first and second interactions. Poor time resolution therefore directly impacts the estimation of E_{TOF} leading to

poor scattering angle reconstruction. Poor position resolution between interaction locations also reduces image quality by increasing uncertainty in E_{TOF}, broadening cone pointing vectors and scattering angle projections in simple backprojection (SBP). The effects of poor position resolution and time resolution can be mitigated by increasing the distance between neutron interactions, but this change would increase the size of the imaging system, decrease the efficiency for double scatter interactions, and reduce the portability of such a system.

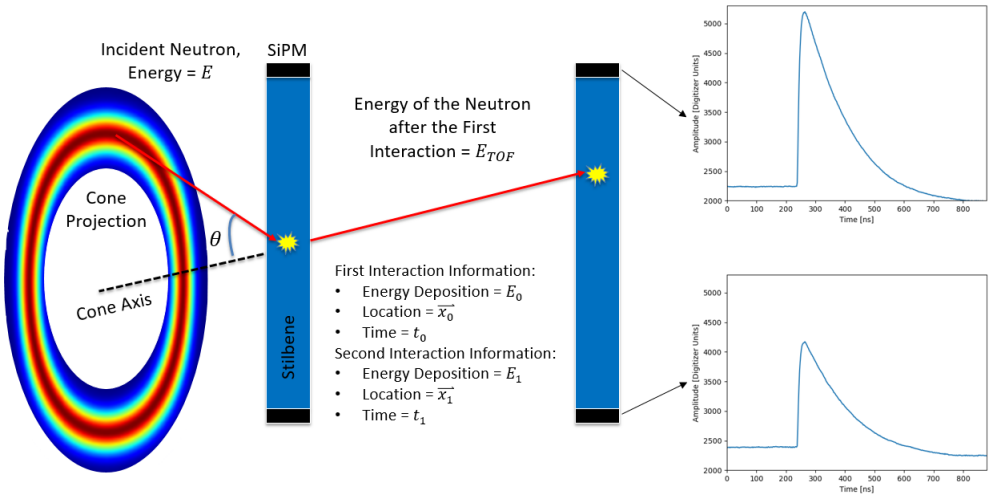

Figure 2.3: Diagram showing a neutron double-scatter event between two pillars of stilbene and the dual-readout system used to acquire information for a given event.

A NSC works by detecting a neutron interaction in one detector and detecting the same neutron in another detector. The cosine squared of the angle, θ', at which the neutron scattered in the first interaction relative to the cone axis or "lever arm", the vector between the two points of interaction, is

$$\alpha = \cos(\theta')^2 = \frac{E_{\mathrm{TOF}}}{E_{\mathrm{TOF}} + E_0}. \tag{2.1}$$

E_{TOF} is the energy of the neutron after the initial scatter. In 2.1, E_0 is the energy deposited in the initial interaction. In

$$E_{\text{TOF}} = \frac{1}{2} m_n \left(\frac{||\vec{x}_0 - \vec{x}_1||}{\Delta t} \right)^2, \tag{2.2}$$

$\vec{x}_0$ and $\vec{x}_1$ are the first and second interaction locations and Δt is the time difference between the two interactions. We used the method described by Ruch et al. [52] to reconstruct the interaction location along the pillar. Ratios that yielded positions outside the length of the pillar were assigned positions at the end of the pillar. This characterization will be discussed in detail in Chapter V.

Once a scattering angle is determined for an event, the event must be projected onto a sphere. To do this, a sphere of some radius is created and pixelated. Each pixel, b, has some position, $\vec{x}_b$, relative to the center of the detector. Determining a value for each pixel for a given cone, d, requires determining a Gaussian distribution for each interaction described in the following relation:

$$C_{d,b} = e^{\frac{-(\beta_b - \alpha)^2}{2(\sigma_\beta^2 + \sigma_\alpha^2)}}. \tag{2.3}$$

Equation 2.3 describes a Gaussian distribution with some effective mean denoted by α and all other points β_b with associated variance, σ^2, for each. β_b,

$$\beta_b = \cos(\theta'')^2 = \frac{((\vec{x}_0 - \vec{x}_1) \cdot (\vec{x}_b - \vec{x}_0))^2}{|\vec{x}_0 - \vec{x}_1|^2 |\vec{x}_b - \vec{x}_0|^2}, \tag{2.4}$$

is equal to $cos(\theta'')^2$ where θ'' is the angle between the cone axis, $(\vec{x}_0 - \vec{x}_1)$, and the vector between the initial interaction location and any pixel location on the projected sphere where the pixel location is denoted as $\vec{x}_b$. The variances for both α and β_b were determined for each location where uncertainties were propagated through the error propagation formula [57]:

$$\sigma_\alpha^2 = \left(\frac{\partial \alpha}{\partial \vec{x}_0} \sigma_{\vec{x}_0} \right)^2 + \left(\frac{\partial \alpha}{\partial \vec{x}_1} \sigma_{\vec{x}_1} \right)^2 + \left(\frac{\partial \alpha}{\partial \Delta t} \sigma_{\Delta t} \right)^2 + \left(\frac{\partial \alpha}{\partial E_0} \sigma_{E_0} \right)^2 \tag{2.5}$$

and

$$\sigma_{\beta_b}^2 = \left(\frac{\partial \beta_b}{\partial \vec{x}_0}\sigma_{\vec{x}_0}\right)^2 + \left(\frac{\partial \beta_b}{\partial \vec{x}_1}\sigma_{\vec{x}_1}\right)^2. \tag{2.6}$$

Solving Equation 2.3 for all pixel values on the projected sphere for a given neutron double-scatter event produces a single cone projection. Cone projections are normalized and summed as described in

$$I_b = \sum_{d=1}^{D} \frac{C_{d,b}}{\sum_{b'=1}^{B} C_{d,b'}}. \tag{2.7}$$

In Equation 2.7, the summation from $d = 1$ to D denotes a summation over all cone projections and the summation from $b' = 1$ to B denotes a summation over all pixel values in a cone projection. Uncertainties are propagated based on individual events, which means some events will be broader than others. Normalizing the cones ensures that broader cones do not bias the result. To generate SBP images, a $1.2{\times}10^7$ n/s ^{252}Cf spontaneous fission source was measured using the H2DPI, depicted in Figure 2.1, for 30 minutes with the source 58.4 cm from the center of the system. SBP images composed of 20, 252 and 1453 imageable events are shown in Figure 2.4. These three images correspond to measurement times of 25 seconds, 5 minutes and 30 minutes demonstrating that the location of neutron sources can begin to be identified with a low number of imageable events. For an event to be imageable, the minimum requirement is that a neutron must scatter twice in the imager in two different pillars. The light output from the first interaction is used to calculate the energy deposition by assuming the energy was deposited through elastic scattering off of hydrogen. The energy of the neutron after the first interaction, E_{TOF}, is determined by the TOF of the neutron and the distance between interactions. The summation of these two energies yields the incident energy of the neutron. This feature makes the H2DPI a neutron spectrometer as well. Figure 2.5 shows the neutron spectrum from the

image in Figure 2.4. A Watt spectrum, normalized to the measured value in terms of counts for the 3.25 mega-electron volts (MeV) energy bin, that is not efficiency-corrected is overlaid with the measured neutron energy spectrum and shows good agreement past 3 MeV. The reason for the insensitivity at lower energies is due to a 100 kilo-electron equivalent (keVee) light output threshold set on all interactions. 100 keVee corresponds to an energy deposition of 0.74 MeV because the conversion from light output to energy deposition is quenched for neutron interactions [58]. The conversion relationship for the stilbene pillars was measured in a time-of-flight experiment using a ^{252}Cf in a similar experimental setup as described by Enqvist et al [59]. Thus, the minimum energy neutron required to produce an imageable event would be just under 1.5 MeV. This threshold was chosen to reduce artifacts in the images produced by interactions with higher relative uncertainty. The following thresholds were also applied to the data: the minimum time difference between coincident neutron events is required to be greater than 250 ps and E_{TOF} has to be greater than the energy deposition in the second interaction. The first threshold of 250 ps is a single standard deviation of the measured time resolution of the system and is assumed to be constant for all coincident events. This threshold ensures that coincident neutron events are sequenced in the correct time order and sets an upper limit for E_{TOF} to be about 21.5 MeV. Approximately 5.6% of events that are classified as neutron double-scatter events by PSD thresholds are rejected due to this timing threshold. The other threshold is put in place to ensure physical events by rejecting chance coincident gamma-neutron events. A neutron cannot deposit more energy in the second interaction than its calculated E_{TOF}.

To determine the most likely origin of neutrons from a measured source, list mode maximum likelihood expectation maximization (LM-MLEM) is applied to the image [60, 61]. LM-MLEM is an iterative algorithm that converges on the most likely angular distribution from which the detected neutrons in the list originated. Mathematically,

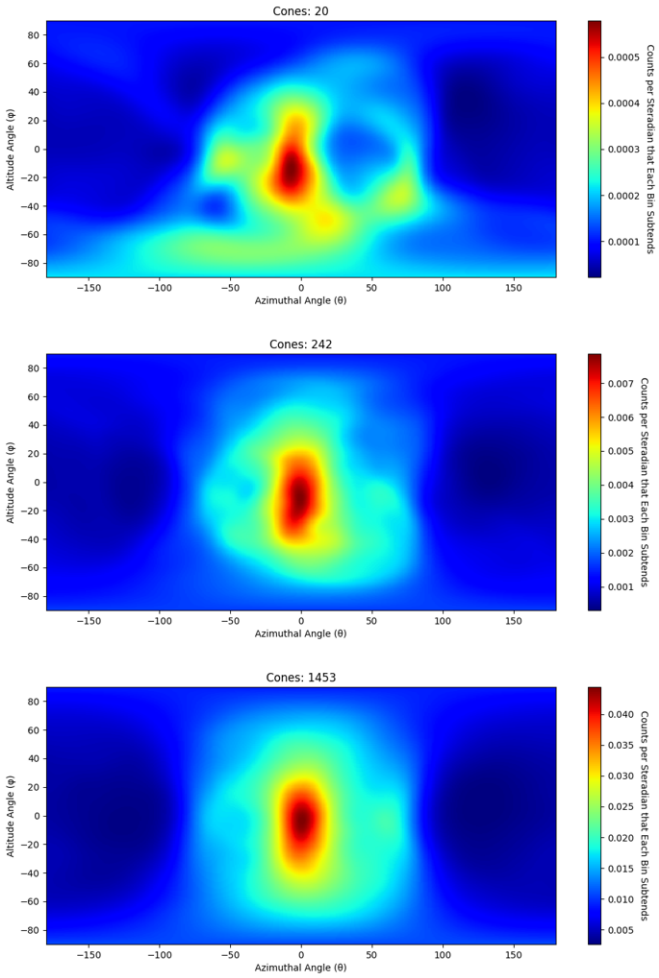

Figure 2.4: Neutron SBP images of a 1.2×10^7 n/s ^{252}Cf spontaneous fission source measured for 25 seconds (20 cones), 5 minutes (242 cones) and 30 minutes (1453 cones) at 58.4 cm from the center of the prototype H2DPI.

LM-MLEM is described in Equation 2.8. In

$$\lambda_b^{\text{New}} = \lambda_b^{\text{old}} \sum_{d=1}^{D} \frac{n_d^* C_{d,b}}{\sum_{b'=1}^{B} \lambda_{b'}^{old} C_{d,b'}}, \tag{2.8}$$

λ_b^{New} is the posterior source distribution, λ_b^{old} is the prior source distribution and n_d^* is the observation vector. The observation vector stores the number of times each observation type occurs within a data set. For LM-MLEM, each observation type occurs once unless you happen to get two identical events. Thus, for LM-MLEM, n^* is just a vector of ones [32, 60, 61]. The summation from $d = 1$ to D, for this

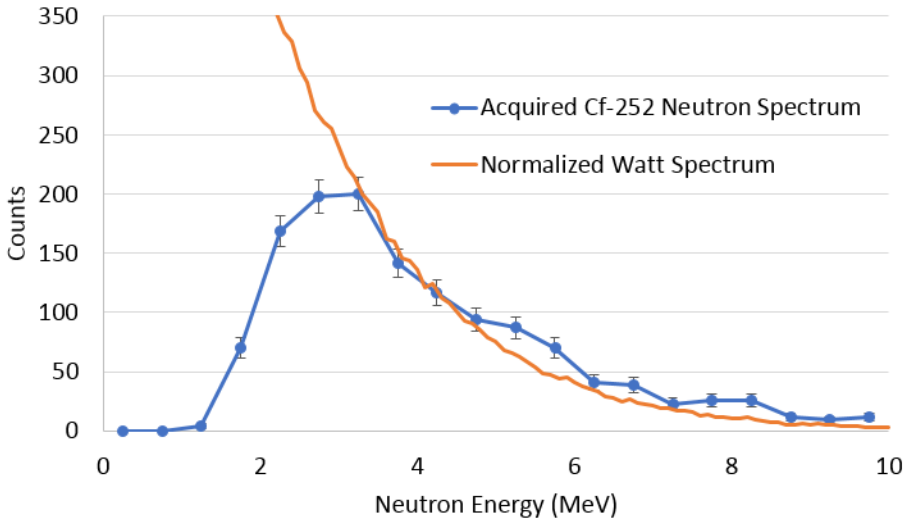

Figure 2.5: Acquired neutron energy spectrum from a 30 minute measurement of a $1.2{\times}10^7$ n/s ^{252}Cf spontaneous fission source at 58.4 cm from the center of the prototype H2DPI overlaid with a normalized Watt spectrum.

application, refers to the summation over all events and the summation from $b' = 1$ to B refers to the summation over all pixels in the image. To begin the iteration process, λ_b^{old} is the initial SBP image. For further iterations, the posterior source distribution becomes the prior source distribution. This analysis examined how non-uniformly the images changed as a function of iteration value to determine a stopping criterion. In

$$\text{Variance}_{\Delta I} = \text{Var}(I_{i+1} - I_i), \tag{2.9}$$

i denotes the iteration value for LM-MLEM and I is the array of values making up the image for a given iteration value. Plotting this parameter, as a function of iteration value yields Figure 2.6. The variance of the image difference changes significantly at low iteration values but begins to level off relative to the initial change around 30 iterations. The exact stopping criteria for neutron images was chosen to be the iteration value just under 2% the maximum value in the distribution seen in Figure 2.6. The stopping criterion used to create the image in Figure 2.7 made up of 20 cones, however, used a stopping criterion of 10%. Figure 2.6 was created with the

data set of 1453 cones shown in Figure 2.4. A stopping criterion of 10% was also chosen for the gamma-ray images.

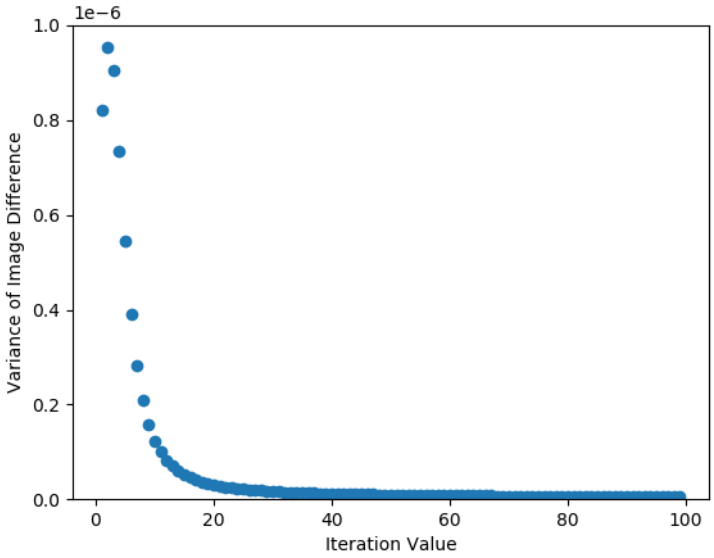

Figure 2.6: Variance in image difference as a function of iteration value.

Each data set shown in Figure 2.4 had LM-MLEM applied to produce the images shown in Figure 2.7. The stopping criterion yielded an iteration value of 23 for the image containing 20 cones, 50 for the image containing 242 cones and 27 for the image containing 1453 cones.

To characterize the quality of the images from the prototype H2DPI, a data set consisting of 16,241 cones from a 6-hour measurement of a ^{252}Cf source was analyzed using a bootstrapping technique. A random cone was sampled from the data set 1000 times and the following 1000 cones after that randomly sampled cone were analyzed to create an image. The location of the most likely pixel and full-width at half maximum (FWHM) in both the altitude and azimuthal directions were recorded. The average and standard deviation of the most likely pixel location was determined to be $(0.66 \pm 0.56^o, -1.82 \pm 2.82^o)$. The FWHM in the azimuthal and altitude directions were determined to be 9.65 ± 0.94^o and 22.59 ± 5.81^o and are reported as the neutron image resolution of the system. The actual location of the ^{252}Cf source was at 0^o in

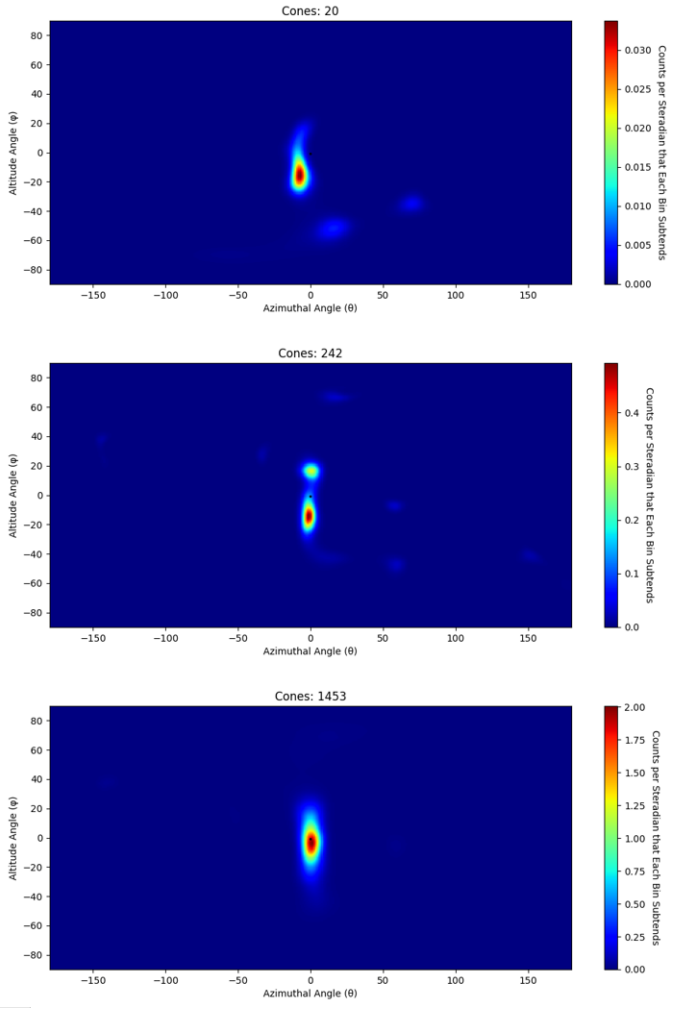

Figure 2.7: Neutron images of a 1.2×10^7 n/s ^{252}Cf spontaneous fission source measured for 25 seconds (20 cones with 23 iterations of LM-MLEM applied to the image), 5 minutes (242 cones with 50 iterations of LM-MLEM applied to the image) and 30 minutes (1453 cones with 27 iterations of LM-MLEM applied to the image) at 58.4 cm from the center of the prototype H2DPI.The source location is represented as a black dot.

the azimuthal direction and -0.8^o in the altitude direction. The size of the source is assumed to be a point source since the mass of ^{252}Cf is in the μg range. The actual locations are within a single standard deviation of the experimentally found altitude position and within 1.2 standard deviations of the azimuthal position.

2.3 Neutron Imaging of Kilogram-Quantites of SNM

Measuring common neutron sources such as ^{252}Cf demonstrate basic neutron-imaging capabilities, but ^{252}Cf does not generate the same radiation in terms of gamma-ray flux as actual SNM. To demonstrate that the H2DPI can image neutrons from kilogram quantities of SNM, a 15.8 hour measurement of a sphere of 4.5 kg of metal alpha-phase weapons-grade plutonium (WGPu) known as the BeRP ball was performed with the object approximately centered in the azimuthal direction and 58 cm from the center of the H2DPI. The neutron flux emitted by the BeRP ball was estimated to be 8.4×10^5 n/s. This estimate was found by simulating the spontaneous fissioning of ^{238}Pu, ^{240}Pu and ^{242}Pu in the BeRP ball using MCNPX-PoliMi [62] given an initial isotopic concentration of the BeRP ball [63]. With the same thresholds used for the ^{252}Cf analysis above, 1660 imageable events were analyzed to create a SBP image. LM-MLEM was applied to the data set of 1660 cones and the same stopping criterion used for the ^{252}Cf source yielded an iteration value of 27 for the data set. Figure 2.8 shows the image of the BeRP ball with 27 iterations of LM-MLEM applied along with an outline of the BeRP ball that shows its approximate location.

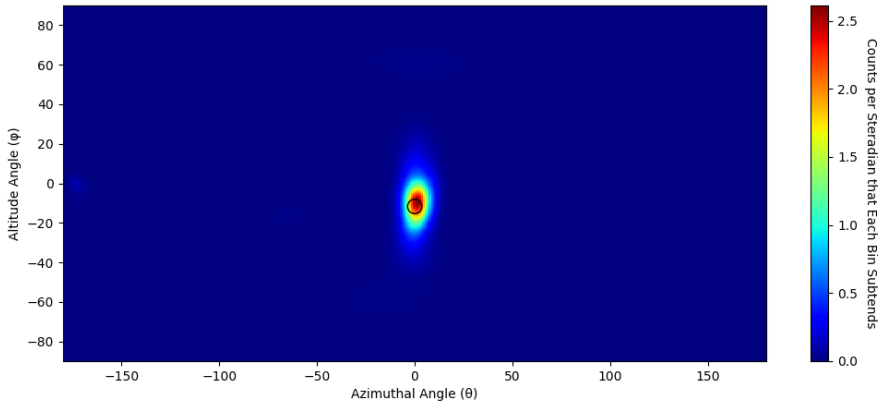

Figure 2.8: Neutron image of the BeRP ball (1660 cones with 27 iterations of LM-MLEM applied to the image). The approximate location and outline of the BeRP ball is shown in black

To further test the capabilities of the H2DPI, a 15.3 hour measurement of both the BeRP ball and a plutonium oxide canister (3.4 kg of 7% ^{240}Pu and 93% ^{239}Pu in oxide) was performed with the materials separated by 50 cm, and 57 cm away from the center of the H2DPI. This measurement acquired 1283 imageable events. Applying the convergence criterion yielded a stopping iteration value of 31 iterations and is shown in Figure 2.9. Two hot spots at (20, -10) and (-25, -5) show the BeRP ball and plutonium oxide canister respectively. An outline of the approximate location of the BeRP ball and the canister containing plutonium oxide are shown in black and white. An outline of the plutonium oxide within the canister is not shown since the exact placement and geometry of the active volume of the plutonium oxide in the canister is not known.

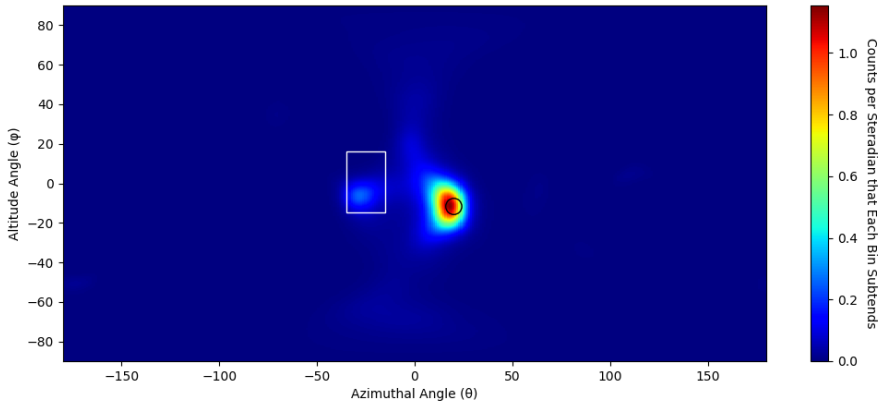

Figure 2.9: Neutron image of the BeRP ball (right) and a plutonium oxide canister (left) 57 cm away and separated by 50 cm (1283 cones with 31 iterations of LM-MLEM applied to the image). The approximate location and outline of the BeRP ball and the plutonium oxide canister is shown in black.

2.4 Compton Imaging using Stilbene

Compton cameras determine the scattering angle of a gamma ray by analyzing the energy deposition of the first interaction and the total energy of the gamma ray.

Traditional Compton cameras require the gamma ray to deposit a portion of its energy in the first interaction, and the rest in the second [37], requiring the gamma ray to undergo photo-electric absorption in the second interaction. The dominant interaction mechanism for gamma rays in organic scintillators, however, is Compton scattering. Approximate Compton imaging is still possible with only organic scintillators even though the full energy of the gamma ray is not deposited [27]. Two adjustments must be made to image gamma rays using organic scintillators: the total energy of the gamma ray must be inferred based on the two interactions and the sequencing of the interactions must be determined. MCNPX-PoliMi [62] was used to determine a correction factor, k, to apply to the energy deposited and solve for α in the following manner:

$$\alpha = \cos(\theta')^2 = \left(1 + m_e c^2 [\frac{1}{E} - \frac{1}{k * E_2}]\right)^2. \tag{2.10}$$

In Equation 2.10, $m_e c^2$ is the rest mass of an electron, E is the energy of the incident gamma ray, k is the correction factor, and E_2 is the energy deposited in the second interaction. E is defined as

$$E = E_1 + k * E_2, \tag{2.11}$$

where E_1 is the energy deposited by the gamma ray in the first interaction. Mono-energetic gamma rays were simulated incident on the stilbene pillars with the arrangement shown in Figure 2.1. The value of k was solved for double-scatter events by using Equation 2.11 since E is known in simulation. It was found that the average value of k was 2.0 and the average value did not change significantly as a function of energy. This value of k was applied to solve for the incident energy of the gamma ray. Sequencing was determined by analyzing gamma-ray interaction events with a time difference between two standard deviations of the time resolution, 0.5 ns, and

three standard deviations of the time resolution, 0.75 ns. The largest flight time of a gamma ray in the H2DPI is 0.27 ns over a flight path of 8 cm. Events occur within the defined window of 0.5-0.75 ns due to the time resolution of the system. Events could also occur due to chance coincidence, but we assume chance coincidence is negligible. We assumed that events within the defined time window can be correctly sequenced by timing. Applying these methods to the BeRP ball data set yields Figure 2.10.

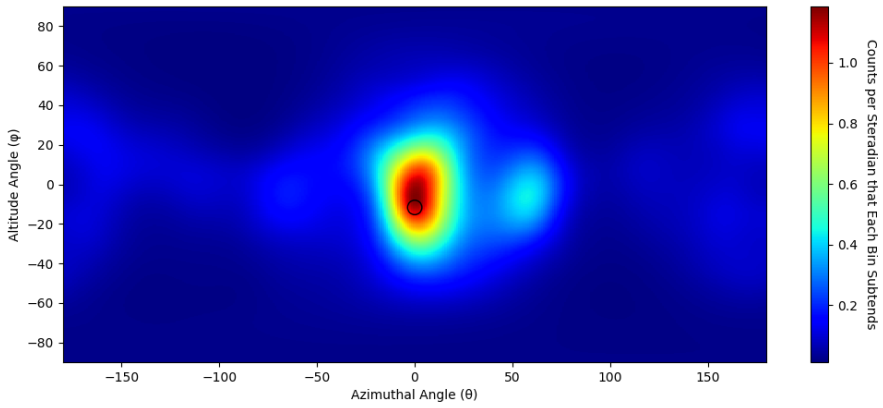

Figure 2.10: Gamma-ray image of the BeRP ball (12,352 cones with 41 iterations of LM-MLEM applied to the image). The approximate location and outline of the BeRP ball is shown in black.

An additional gamma-ray image was produced from a measurement of a 6 kg sphere of neptunium that was placed 55 cm away from the center of the H2DPI. The sphere is composed of mostly ^{237}Np [64] and emits $8700 n/s$ [65], which is about 1% of the neutron intensity of the BeRP ball. We were not able to produce a neutron image of the sphere in the 45 minute acquisition time but were able to produce a gamma-ray image of the sphere as shown in Figure 2.11.

2.5 Conclusions

Neutron images are presented for a ^{252}Cf spontaneous fission source, the BeRP ball (4.5 kg of alpha-phase WGPu), and the BeRP ball along with a plutonium oxide

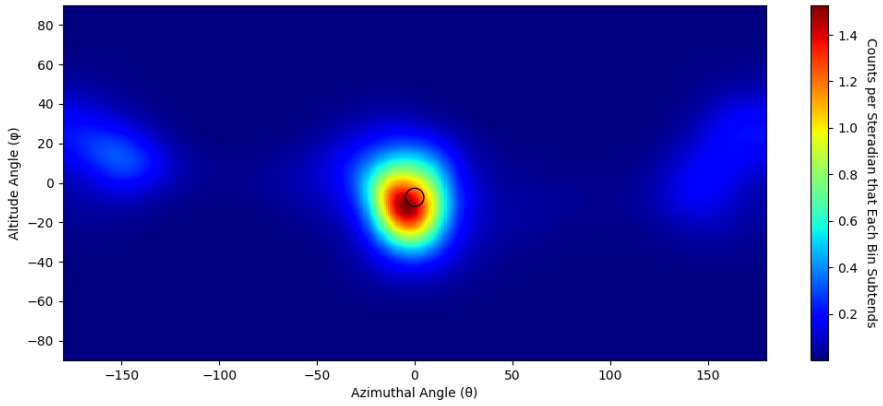

Figure 2.11: Gamma-ray image of a 6 kg sphere of neptunium (7441 cones with 180 iterations of LM-MLEM applied to the image). The approximate location and outline of the sphere of neptunium is shown in black

canister in the same field of view. For the ^{252}Cf point source, the image resolution was found to be 9.65 ± 0.94^o in the azimuthal direction and 22.59 ± 5.81^o in the altitude direction. Image characteristics from the BeRP ball did not significantly deviate from those measured with the ^{252}Cf source. These results demonstrate that the H2DPI can image both sources in the laboratory and kilogram quantities of SNM. The image resolution was also validated by imaging multiple sources in the same field of view. The BeRP ball and a plutonium oxide canister were separated by 47^o relative to the center of the H2DPI. Figure 2.9 shows the two sources separated by 45^o with distinct space between the sources, meaning that both sources are resolved. The reason that the plutonium oxide source image is not as intense as the BeRP ball image is that the plutonium oxide yielded about half the number of incident neutrons on the H2DPI as the BeRP ball. LM-MLEM then converges on the most likely source distribution. Since it is more likely a neutron originates from the more intense BeRP ball, the image will converge more on that source. If the sources had the same neutron emission rate and spectrum, then the sources would converge with the same intensity [66, 67]. Nevertheless, we were still able to resolve and image the two sources.

National security missions may require versatile detector systems to be able to detect SNM under a wide range of conditions, including complex shielding scenarios. In these cases, any information that can be acquired from a source can be useful to detect and localize it. For instance, being able to detect and image both gamma rays and fast neutrons allows for multiple methods to determine the location of a source of plutonium. This approach was demonstrated with the BeRP ball where the H2DPI was able to successfully produce neutron and gamma-ray images of the source. The ability to image both types of radiation is also beneficial for scenarios where only one type of particle may be present. The scenario detailed in this work is with ^{237}Np, which does not emit a significant amount of neutrons relative to other spontaneous fission sources. We were not able to acquire any imageable neutron double scatter events over the 45 minute acquisition time. However, we were able to acquire 7441 imageable gamma-ray events to produce Figure 2.11. Being able to image both neutrons and gamma rays can also help verify a source's location. We were able to generate a gamma-ray image of the BeRP ball, giving two methods to image or verify the same source. Comparing the gamma-ray images to the neutron images, it can be seen that there are significantly more artifacts in the gamma-ray images. There is a significant artifact at 50 degrees in the azimuthal direction in Figure 2.10. These artifacts are most likely due to a combination of incorrect sequencing and incorrect determination of the incident energy of the gamma ray. A user seeing these artifacts in an image would have to determine if another weaker source was present or if the resulting image intensity was indeed an artifact. Incorporation of inorganic scintillators can mitigate these image artifacts by allowing for Compton imaging of gamma rays instead of the approximate method presented since inorganic scintillators have the density and atomic numbers necessary for photoelectric absorption of the gamma rays. Inorganic scintillators are generally not sensitive to fast neutrons and some optimization will have to be performed to determine how

many scintillators should be incorporated and where the scintillators should be placed as to not significantly impact the neutron-imaging efficiency. To better understand how the placement of the inorganic scintillators and choice of inorganic scintillator will impact image reconstruction, Chapter III breaks down and analyzes the three components of scatter-based image reconstruction.

CHAPTER III

Fundamentals of Scatter-Based Imaging

3.1 On the Generation of Simple Backprojection Images

Three components impact the generation of SBP images: the lever arm or cone axis ($\vec{x}_0 - \vec{x}_1$), the scattering angle (θ') and the uncertainties in the cone projection ($\sigma_\beta^2 + \sigma_\alpha^2$). The uncertainties in α and β are defined in Equations 2.5 and 2.6. The lever arm dictates the location for where the scattering angle will be projected around and the uncertainties dictate the width of the projection. All the uncertainty propagation and location reconstruction detailed in the previous chapter feed into generating these three components. It is not intuitive how these components interact to generate SBP images. Therefore, the reconstruction of SBP images will be thoroughly explored in the following sections.

3.2 Modeling Simple Backprojection Images

In order to determine how the three components impact the generation of SBP images, a model was developed where ranges of these three parameters could be input to generate a given image. The first image generated is shown in Figure 3.1 and will be the "target" or "ideal" image that other generated images in this chapter will be compared. The image in Figure 3.1 is composed of 80,100 cone projections where the

cone projections had a scattering angle range from (1^o to 90^o) in 1^o increments and each cone projection was broadened in a range from (10% to 100%) in 10% increments. Broadening was applied to each scattering angle and cone such that nine cones were produced for a given scattering angle and lever arm location. Each angle was then symmetrically projected around the source location of (0^o, 0^o) 100 times to generate a uniform lever arm distribution. A subset of the lever arm distribution is shown in Figure 3.2 where the lever arm locations are plotted in terms of azimuthal and altitude angle. These azimuthal and altitude points were determined based on where the cone axis, $(\vec{x}_0 - \vec{x}_1)$, intersects with the pixelated sphere discussed in Section 2.2. Each lever arm location is equal to the scattering angle degrees away from the source location of (0^o, 0^o) such that each cone projection will intersect the center location.

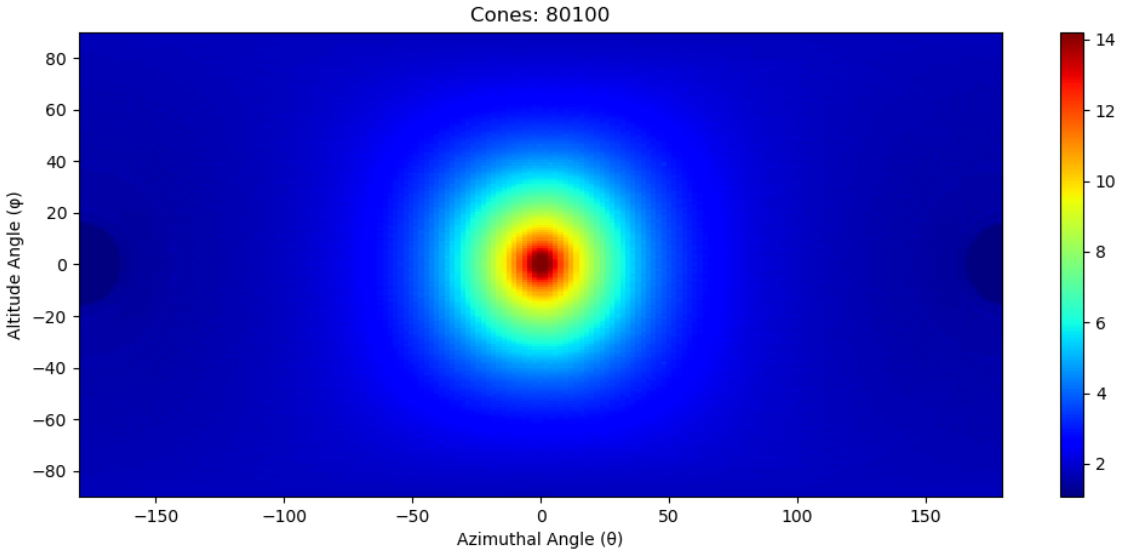

Figure 3.1: Target SBP image composed of scattering angles from (1^o to 90^o) in 1^o where each scattering angle was broadened from (10%-100%) in 10% increments. Each angle was then projected symmetrically about the center of the image 100 times.

Broadening for the cone projections was determined by taking a fraction of the α and β value used in the projection. For instance, a 10% cone uncertainty or broadening for σ_α would be

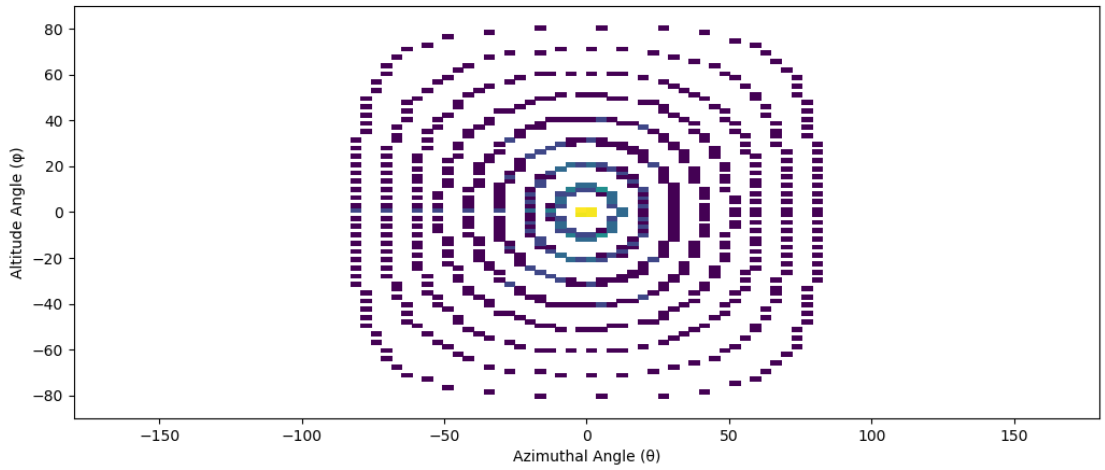

Figure 3.2: Two-dimensional histogram showing the azimuthal and altitude locations for a subset of the lever arms making up Figure 3.1.

$$\sigma_\alpha = 0.1 * \alpha. \tag{3.1}$$

Each angle cone projection making up Figure 3.1 was broadened using this methodology so that each lever arm location had nine cone projections from the given location. This methodology was chosen to see how a uniform distribution of these parameters generate a SBP image.

Analyzing Figure 3.1 yields an azimuthal FWHM of 41.6^o and altitude FWHM of 36.2^o. Comparing this image to the image previously obtained from the ^{252}Cf point source shown in Figure 2.7, it is apparent that the image is more symmetric in terms of azimuthal and altitude angles. The SBP image of the ^{252}Cf point source has a larger altitude FWHM whereas the target image shown in Figure 3.1 has a slightly larger azimuthal FWHM. To understand this difference in these images, the following sections break down the three components to determine why a less uniform response is being obtained in the reconstructed neutron image.

3.2.1 Lever Arm Distributions

Figure 3.3 shows three cone projections with a scattering angle of 25^o and relative uncertainty of 10%. The lever arm locations for these three projections are (25^o, 0^o), (0^o, -25^o) and (-25^o, 0^o) and shown as black dots on each image. Each projection intersects the center of the image, (0^o, 0^o), which is shown as a white dot. This figure explicitly shows how the cone projections are projected relative to the placement of the lever arm. Having many lever arms, such as were used to generate Figure 3.1, produces a relatively symmetric image. Limiting the number of lever arms, however, produces asymmetric images. An example of such an image and lever arm distribution is shown in Figure 3.4.

Figure 3.4 (b) was generated using the lever arm distribution shown in (a). Figure 3.4 (a) shows four bands which represent the normalized lever arms, $(\vec{x}_0 - \vec{x}_1)$, used to project cones. The lever arms were equally spaced around the source location in terms of angle. Limiting the distribution of lever arms to four distinct bands produces a SBP image with a cross shape. Simply increasing the number of bands from 4 to 25 in the lever arm distribution, shown in Figure 3.5, greatly increases the symmetry of the image. The lever arms making up Figure 3.5 are symmetrically projected about the center of the image. Making the lever arm distribution asymmetric about the center position significantly changes the shape of the image. An example of an asymmetric lever arm distribution and the resulting image is shown in Figure 3.6.

The image shown in Figure 3.6 (b) has an azimuthal FWHM of 21.8^o and an altitude FWHM of 46.4^o. The reason that the altitude FWHM is so much greater than the azimuthal FWHM is due to how the cone projections are being overlaid. A diagram depicting how the cone projections intersect is shown in Figure 3.7. The lever arm distribution in Figure 3.6 is effectively a series of vertical lines across the azimuthal direction. When the cone projections intersect the source location, they overlay in the altitude direction. This effect can be visualized in Figure 3.6 where the

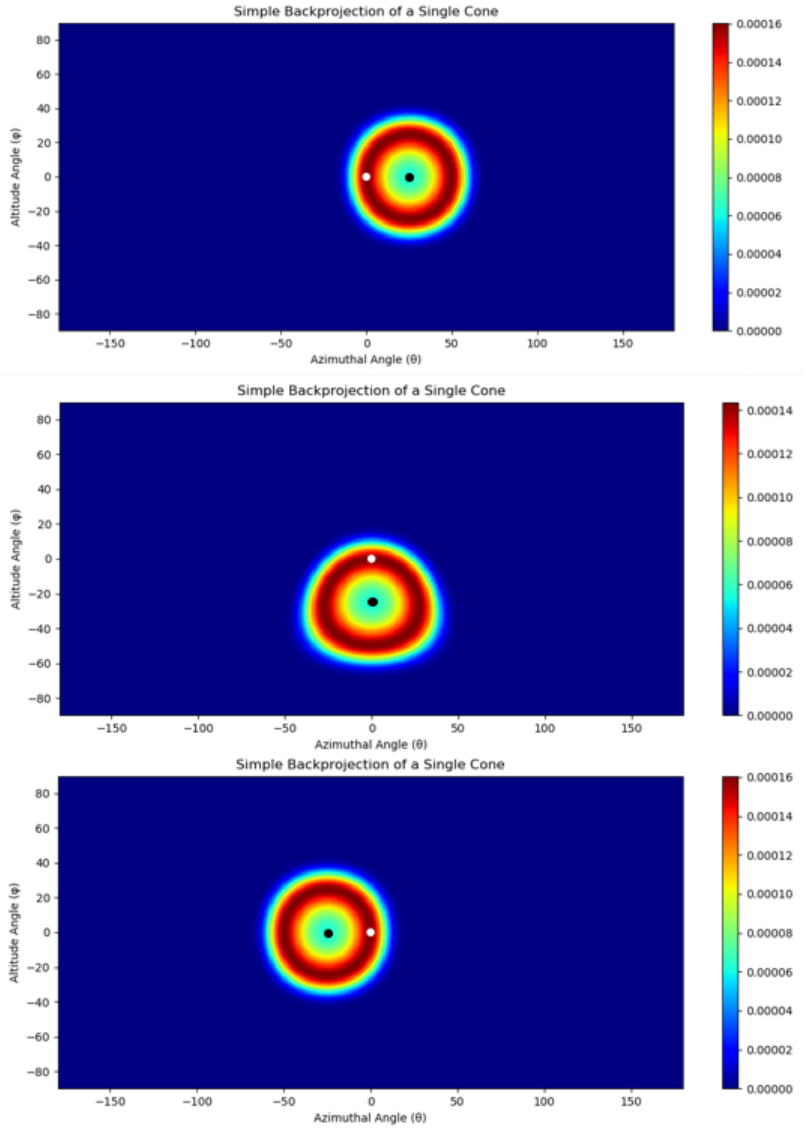

Figure 3.3: Simulated cone projections with a relative uncertainty of 10%, scattering angle of 25^o and lever arm positions at (a) (25^o, 0^o), (b) (0^o, -25^o) and (c) (-25^o, 0^o) shown as black dots. The source location is shown as a white dot in each image.

blue cone projections are above and below the source location, but not to the sides of the source location. This result explains why the altitude FWHM is much greater than the azimuthal FWHM for the reconstruction of the ^{252}Cf point source using the initial H2DPI. The initial H2DPI has an asymmetric lever arm distribution much like what is shown in Figure 3.7; giving the reconstruction an asymmetric shape.

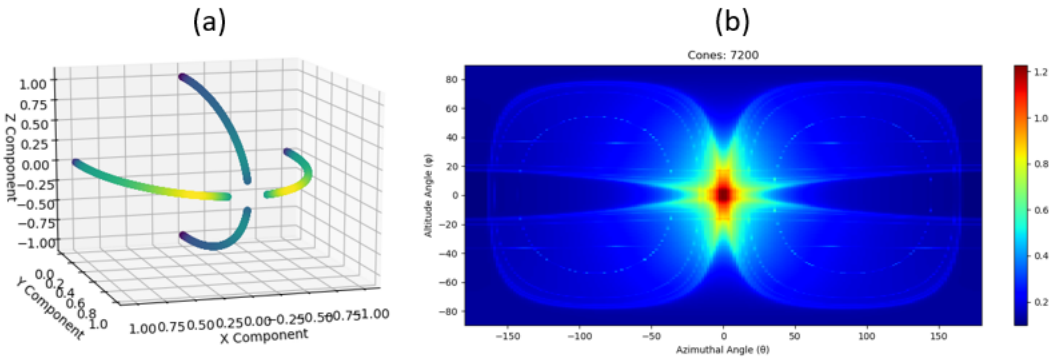

Figure 3.4: The (a) symmetric lever arm distribution composed of four lever arms used to generate (b) a SBP image using a relative uncertainty range from (10%-100%) in 10% increments and scattering-angle range from (10^o - 170^o) in 1^o increments.

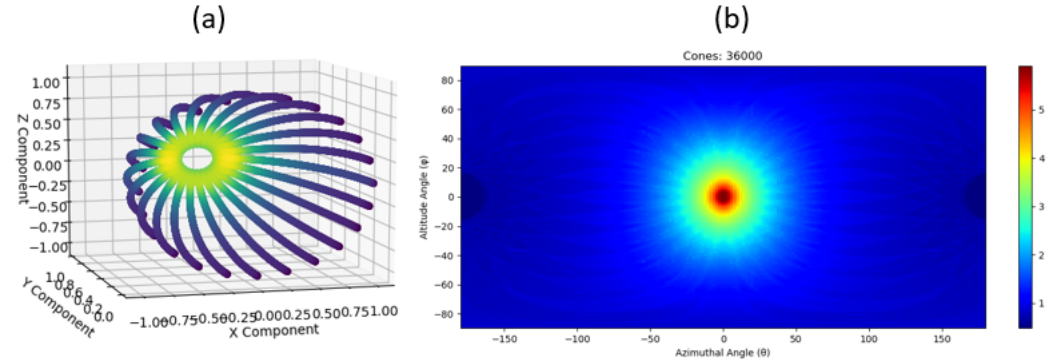

Figure 3.5: The (a) symmetric lever arm distribution composed of twenty-five lever arms used to generate (b) a SBP image using a relative uncertainty range from (10%-100%) in 10% increments and scattering-angle range from (10^o - 170^o) in 1^o increments.

3.2.2 Scattering Angles

The scattering angle, θ, is directly used to solve for α as shown in Equation 2.1. Figure 3.8 shows three scattering angle cone projections, (25^o, 45^o and 60^o), where each cone projection intersects with the source location at (0^o, 0^o) and has a relative uncertainty of 10%. While the relative uncertainty in the scattering angle was kept constant between the images shown in Figure 3.8, the overall width of the projection decreases significantly as the angle increases. This effect is due to the nature of

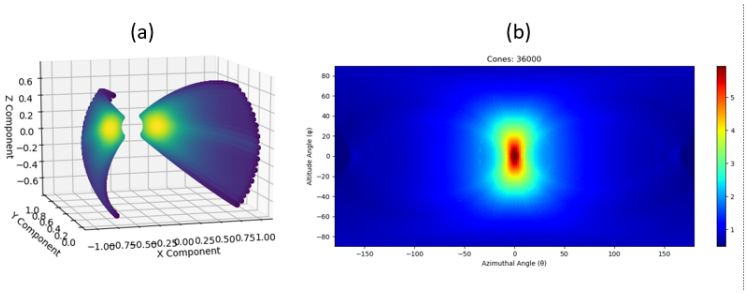

Figure 3.6: The (a) asymmetric lever arm distribution composed of twenty-five lever arms used to generate (b) a SBP image using a relative uncertainty range from (10%-100%) in 10% increments and scattering-angle range from (10^o - 170^o) in 1^o increments.

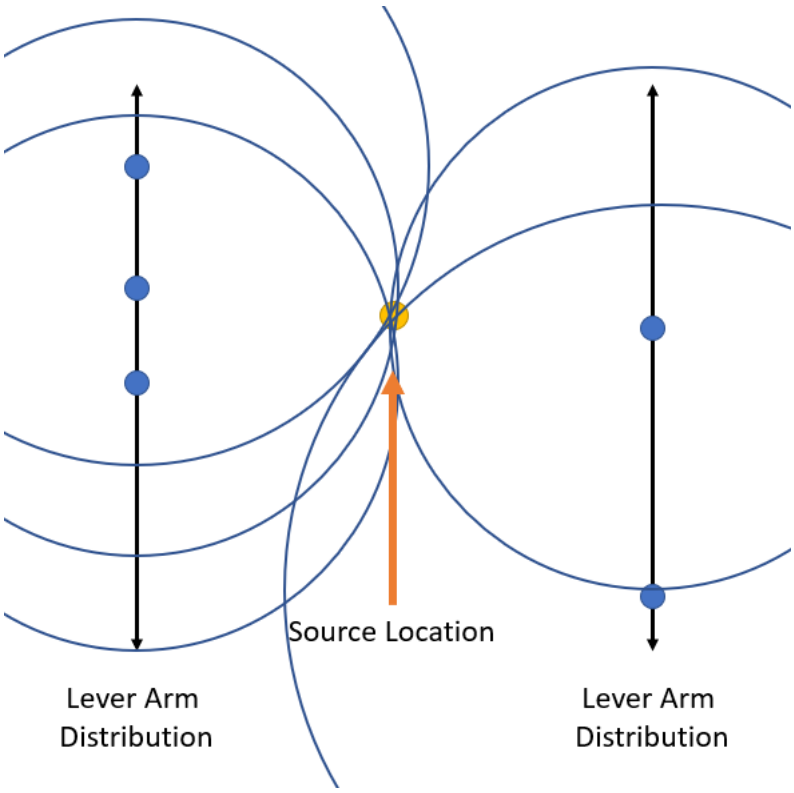

Figure 3.7: Diagram depicting the overlay of cone projections (shown as blue lines) along two linear lever arm distributions.

how the relative uncertainty is being accounted for with the scattering angle. As θ approaches 90^o, $\cos(\theta)$ goes to zero. Taking a fractional value of α to maintain constant relative uncertainty will then make angles that are closer to 90^o have smaller overall uncertainties. Generating images with variable scattering angle distributions

then directly impacts the resolution of the image as shown in Figure 3.9.

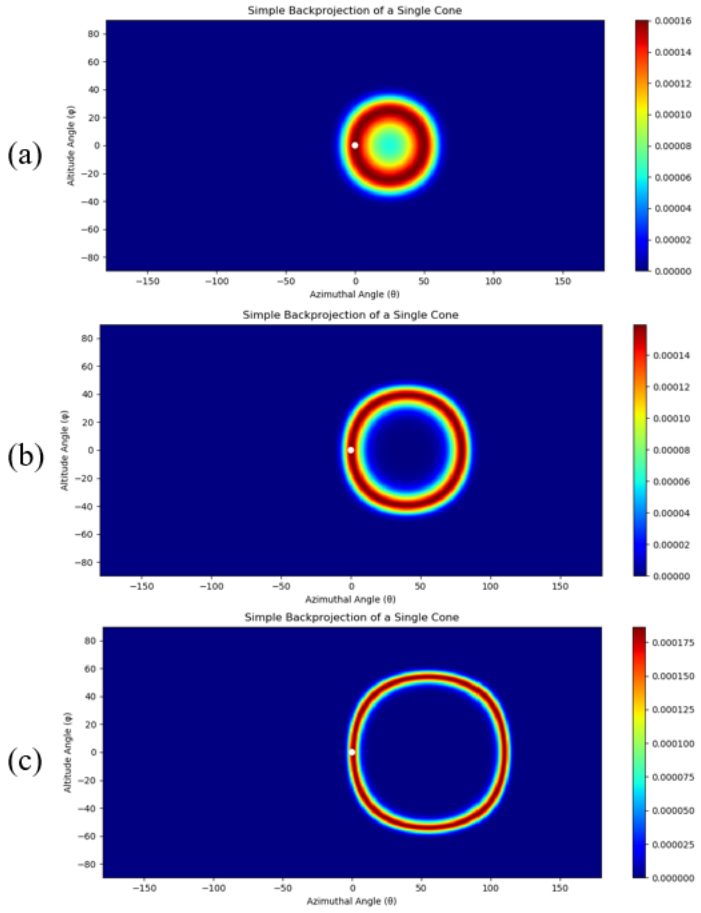

Figure 3.8: Simulated cone projections with a relative uncertainty of 10% and the following scattering angle and lever arm locations: (a) 25^o scattering angle with a lever arm at (25^o, 0^o), (b) 45^o scattering angle with a lever arm at (45^o, 0^o), and (c) 60^o scattering angle with a lever arm at (60^o, 0^o).

The azimuthal and altitude FWHMs for the images in Figure 3.9 are (a) (34.5^o, 29.1^o) and (b) (22.2^o, 17.2^o). Removing the scattering angles closer to 0^o and 180^o significantly improves the resolution of the image. Both images in Figure 3.9, however, have better resolution than the target image in Figure 3.1. This difference is because more scattering angles closer to 90^o were used to generate the images shown in Figure 3.9. Those cone projections closer to 90^o, while having the same relative uncertainty, converge better on the source location because the widths of the projections are not as broad as the higher and lower scattering angles.

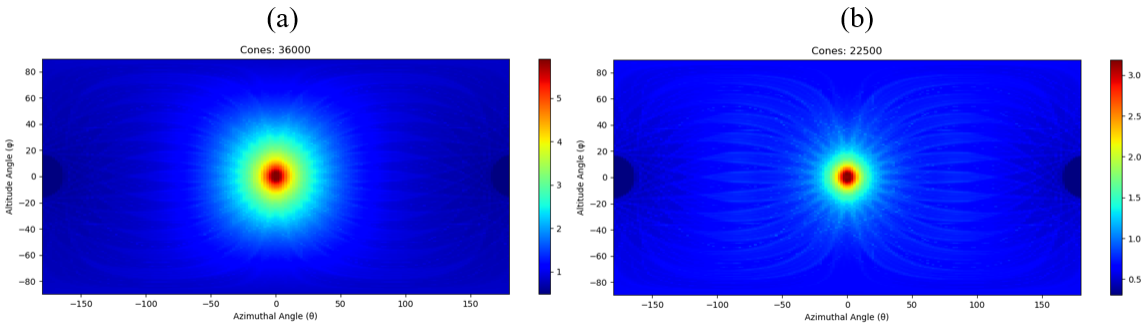

Figure 3.9: Comparison between images generated using (a) scattering angles from (10^o - 170^o) in 1^o increments and (b) (40^o - 140^o) in 1^o increments. Both images were generated using a relative uncertainty range from (10%-100%) in 10% increments along with twenty-five lever arms distributions symmetrically around the center of the image.

3.2.3 Cone Projection Uncertainty

The final aspect that impacts the generation of SBP images is the relative uncertainty in the projection. The previous images in this chapter have all been generated using a relative uncertainty range from (10%-100%) in 10% increments. Figure 3.10 shows the impact from modifying the relative uncertainty in the cone projection for a 25^o cone projection with a lever arm location at (25^o, 0^o). Due to the normalization of each cone projection, the relative intensity of the projection decreases as the uncertainty increases. This normalization ensures that cone projections with higher relative uncertainty are not treated the same as projections with lower relative uncertainty.

Changing the distribution of uncertainties in the generated SBP images directly impacts the resolution of the image. Figure 3.11 compares an image generated with (a) relative uncertainties from (10%-100%) in 10% increments and (b) (7.5%-27.5%) in 2.5% increments where all other aspects of the image generation process were kept constant. As expected, the image with the lower relative uncertainty distribution has a better resolution than the image with the higher relative uncertainty distribution. The azimuthal and altitude FWHMs for the two images are (a) (34.5^o, 29.1^o) and (b)

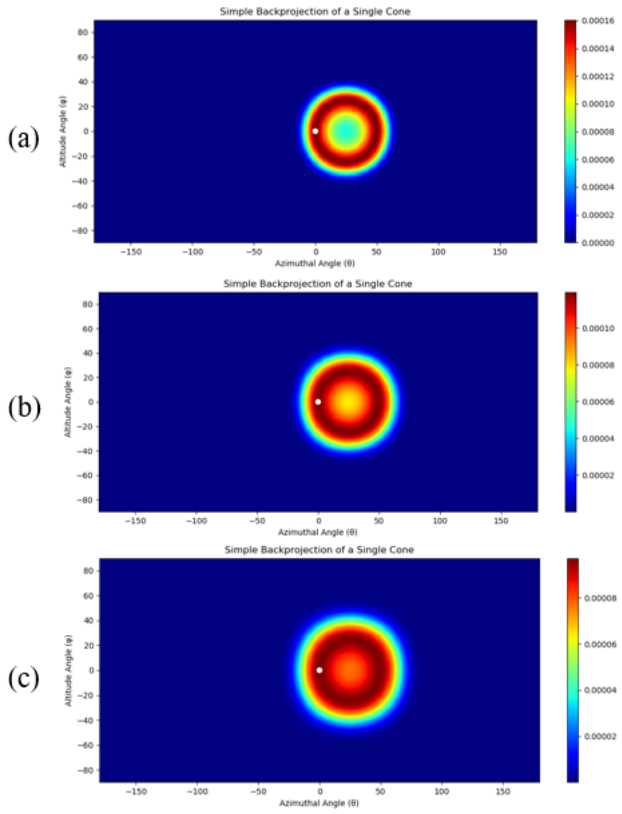

Figure 3.10: Simulated cone projections with a scattering angle of 25^o and a lever arm at (25^o, 0^o) with relative uncertainties of (a) 10%, (b) 50% and (c) 100%.

(29.5^o, 28.3^o). The improvement in image resolution is not as significant as the case where the scattering angles were limited, however, a more uniform image is acquired with the lower relative uncertainty distribution.

3.3 Conclusions

Breaking down scatter-based imaging into the three fundamental components allows one to visualize and better understand the image generation process. Both the scattering angle distribution and relative uncertainty distribution directly impact the resolution of an imaging system while the lever arm distribution directly impacts the symmetry and shape of a generated image. Results also demonstrate the importance in the number of lever arm distributions in image generation. Having too few lever

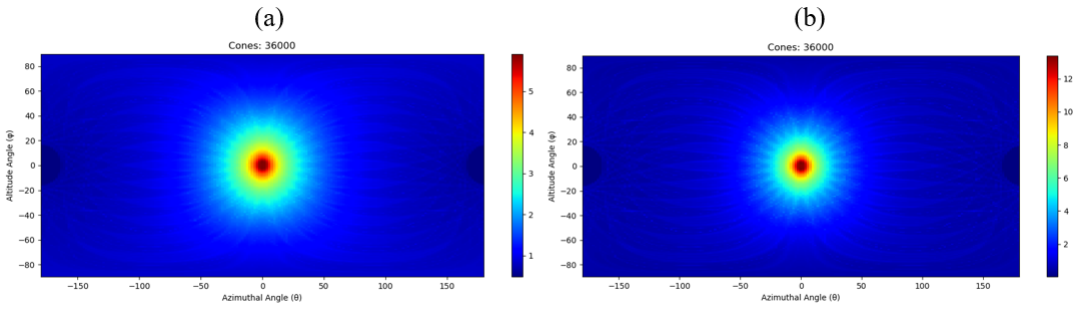

Figure 3.11: Comparison between images generated using (a) relative uncertainties from (10%-100%) in 10% increments and (b) (7.5%-27.5%) in 2.5% increments. Both images were generated using scattering angles from (10^o - 170^o) in 1^o increments along with twenty-five lever arms distributions symmetrically around the center of the image.

arms will generate odd shapes such as those shown in Figure 3.4. If the number of lever arms were to be further reduced, image artifacts can be generated based on the allowable and intensity of the scattering angles. This specific effect will be further discussed in Section 4.2.2. These parameters, however, can also be exploited in the design of a system. As shown in Figure 3.6, the azimuthal resolution can be directly adjusted to increase resolution across the azimuthal direction at the expense of resolution in the altitude direction. If a system required finer directional capabilities in the azimuthal direction than the altitude direction, such a system could be designed with a asymmetric lever arm distribution to meet that criterion. Chapter IV details the characterization of various inorganic scintillators, the process used to choose an inorganic scintillator to incorporate into the H2DPI, and the optimization process used to place the inorganic scintillators into the prototype. Choice of a specific inorganic scintillator directly impacts the relative uncertainty in the cone projections due to the energy resolution of the scintillator, and the placement of the scintillators will impact the scattering angle and lever arm distributions. Results from the above analysis demonstrate the need for a symmetric lever arm distribution to acquire a uniform system response. This symmetric response is of interest so that the H2DPI can image and resolve sources uniformly in 4π.

CHAPTER IV

Incorporation of Inorganic Scintillators into the H2DPI

Reconstructing gamma-ray images using only organic scintillators can result in image artifacts due to incorrect sequencing of the interactions or inaccurate determination of the incident energy of the gamma ray. A user applying this methodology to image a gamma-ray emitting source would need to verify if a source was present at the artifact location. To mitigate the generation of artifacts in the reconstructed images, inorganic scintillators are incorporated into the design. Inorganic scintillators have sufficient density and effective atomic value so that photoelectric absorption of gamma rays is possible. This chapter analyzes several types of inorganic scintillators and presents a methodology for the incorporation of the scintillators into the design of a 16-pillar prototype H2DPI.

4.1 Characterizing Inorganic Scintillators

The following inorganic scintillators were tested for incorporation into the H2DPI: NaI(Tl), CsI(Na), CLYC, CLLBC, LYSO, and $CeBr_3$. Figure 4.1 shows a photograph of several of the types of scintalltors acquired. Both small versions of cubes or cylinders with heights of six millimeters and pillars with heights of fifty millimeters were

acquired for testing. Initial testing of the pillars showed some promise, but a primary issue removed them from consideration. The variance in the length of the inorganic pillars was greater than the coupling tolerance. For the pillars of $CeBr_3$, while lengths were requested to be 50 mm, lengths ranged from 49 to 50.5 mm. Using optical interfaces with a width of 0.5 mm made it so the various scintillators could not be appropriately coupled to the SiPMs within the system. This result pushed the future design of the H2DPI to be composed of the smaller versions of the scintillators where a support system would be implemented so that the scintillators could be coupled within the system. Figure 4.2 shows a photograph of two sets of $CeBr_3$ scintillators coupled to the top and bottom array of ArrayJ-60035-64P-PCB SensL SiPMs [68] in a "sandbox" version of the H2DPI. A sandbox version of the H2DPI was built specifically for the testing of these inorganic scintillators so that an accurate response of the scintillators could be acquired for modeling the response of a potential system.

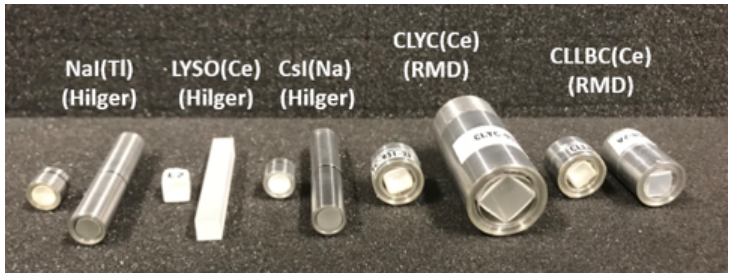

Figure 4.1: Photograph of several of the types and geometries of tested inorganic scintillators.

Table 4.1 shows the results of testing various inorganic scintillators with a 100 μCi ^{137}Cs source. The rise time listed is the average and standard deviation of the time it takes the pulses to go from 10% of the pulse amplitude to 90% of the pulse amplitude before the peak. The fall time listed is the time it takes the pulses to go from 90% of the pulse amplitude to 10% of the pulse amplitude after the peak of the pulse. The dynamic range is the maximum energy detectable without a pulse being clipped using a 2-V dynamic range and a v1730 CAEN digitizer. Photopeak efficiency is defined as

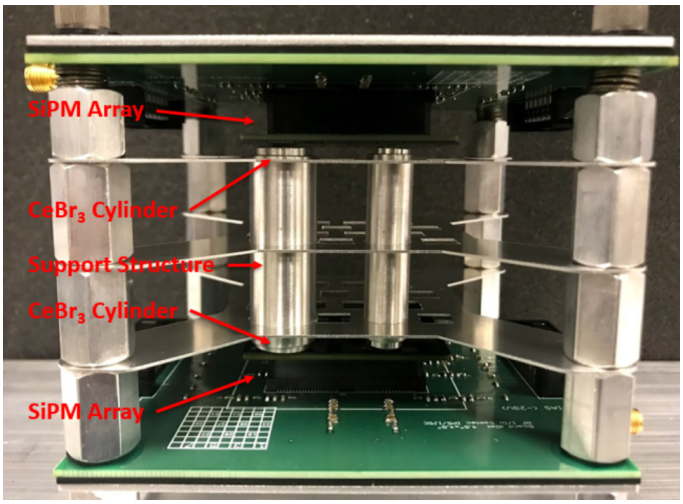

Figure 4.2: Photograph showing the coupling and testing of $CeBr_3$ scintillators within a sandbox version of the H2DPI.

the integral of the photopeak over the integral of the background-subtracted energy spectrum above 50 keV. A threshold of 50 keV was set to ensure that there was not significant bias from the ^{137}Ba X-rays.

Table 4.1: Measured responses of tested inorganic scintillators.

Parameter of Interest	NaI(Tl) (Hilger Crystals)	CsI(Na) (Hilger Crystals)	LYSO(Ce) (Hilger Crystals)	CLYC(Ce) (RMD)	CLLBC(Ce) (RMD)	$CeBr_3$ (Advatech)
Resolution (% at 662 keV)	7.3	9.2	9.8	10.3	5.2	4.5
Rise Time (ns)	130±26	196±54	40±5	144±55	98±28	21±11
Fall Time (ns)	595±37	1310±193	583±54	1151±199	756±89	309±19
Energy Range (MeV)	3.0	5.6	1.6	7.3	6.1	-
Photopeak Efficiency (% at 662 keV)	11.7	15.8	30.6	9.1	9.8	8.4

The initial testing narrowed down the analysis to two scintillators based on their

measured efficiency, energy resolution and pulse shape: LYSO(Ce) and $CeBr_3$. LYSO(Ce) has a density of 7.1 $\frac{g}{cm^3}$ and an effective atomic number of 66. These two parameters make LYSO(Ce) excellent at stopping gamma rays, which is apparent based on the result for the photopeak efficiency. LYSO(Ce) has the best efficiency out of the tested scintillators in Table 4.1. Intrinsic efficiency is of interest to the development of compact imaging systems since absolute efficiency will be small due to the size of the system. The other primary benefit to LYSO(Ce) is that the pulse shape is not significantly different than that of stilbene. Having various scintillators within the system that yield the same pulse shape means that only a single acquisition time window is needed to acquire all pulses from all channels. The primary drawback from this testing to LYSO(Ce) is the energy resolution. Energy resolution, however, is where $CeBr_3$ performed the best out of the tested scintillators. $CeBr_3$ also has a similar pulse shape relative to the stilbene response in the tested system. Comparing the two scintillators, LYSO(Ce) and $CeBr_3$, there is effectively a trade off between efficiency and energy resolution. To quantify the impact of these differences in a system, miniaturized versions of the H2DPI were built and tested.

4.2 Choosing an Inorganic Scintillator

4.2.1 Compton Imaging Methodology

A new Compton imaging methodology was developed in order to test a system composed of organic and inorganic scintillators. The previous approximate Compton imaging methodology suffered from incorrect sequencing and significant uncertainty in the energy of the incident gamma ray. Incorporation of inorganic scintillators into the H2DPI solves both of these issues. Both LYSO(Ce) and $CeBr_3$ have densities and effective atomic numbers that allow for photoelectric absorption in the range of gamma-ray energies of interest. These characteristics of the scintillators mean

that the incident energy of the gamma ray can be directly measured in a coincident event assuming the gamma ray undergoes Compton scattering in a stilbene pillar and photoelectric absorption in an inorganic scintillator volume. This assumption also solves for the sequencing of the interactions. Gamma rays in the energy range of interest will not undergo photoelectric absorption in stilbene. If a photopeak in a coincident energy spectrum is measured, that means that the gamma rays must have undergone Compton scattering in a stilbene pillar and then photoelectric absorption in an inorganic scintillator volume. To demonstrate the validity of this assumption, an MCNP-PoliMi model of a 16-pillar version of the H2DPI was made composed of stilbene pillars and $CeBr_3$ cylinders. A ^{137}Cs source was simulated 45 cm from the center of the system. Figure 4.3 shows the resulting coincident energy gamma-ray spectrum along with the correct and incorrect sequencing of events. In this case, incorrect sequencing is defined as the gamma ray interacting with a $CeBr_3$ volume first and then with a stilbene volume. Figure 4.3 shows that events within the photopeak at 662 keV are accurately sequenced using this methodology. Events within the photopeak can then be imaged using the same methodology as neutron imaging except $\cos(\theta')$, where θ' is the incident scattering angle of the gamma ray, is equal to

$$\cos(\theta') = 1 + m_e c^2 (\frac{1}{E} - \frac{1}{E_2}). \tag{4.1}$$

In Equation 4.1, E_2 is the energy deposited in the second interaction, E is the summation of the two energy depositions in both interactions, and $m_e c^2$ is the rest mass of an electron in MeV.

Figure 4.4 shows the resulting SBP image from reconstructing events within the defined summed photopeak shown in Figure 4.3. Figure 4.4 accurately converges on the correct source location shown as a white circle.

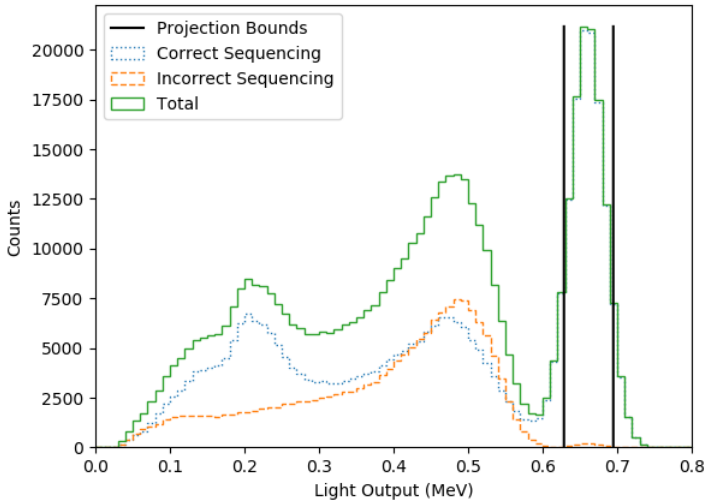

Figure 4.3: Simulated coincident spectrum from a ^{137}Cs source 45 cm from the center of one of the possible designs of the H2DPI containing $CeBr_3$.

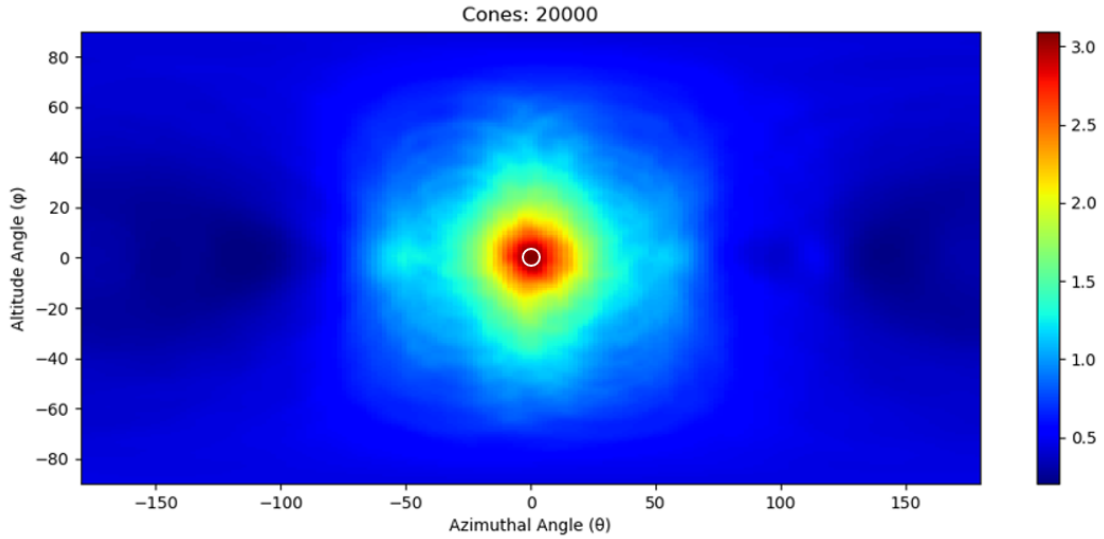

Figure 4.4: SBP image composed of 20,000 cone projections from a ^{137}Cs source at (0^o, 0^o) and 45 cm from the center of the system for the energy spectrum shown in Figure 4.3.

4.2.2 Testing a Miniaturized System

Validation of the proposed Compton imaging methodology in simulation may not take into account all aspects of an experimental system. In the words of Marie Curie, "Well, we might try it all the same." Therefore, it is necessary to test a physical

system to ensure all aspects are taken into account in simulation. To decide on the incorporation of a scintillator, miniature versions of the H2DPI were built composed of either LYSO(Ce) or $CeBr_3$ and stilbene cubes. Figures 4.5 and 4.6 show photographs of both systems along with layouts of the placement of the scintillators. Five stilbene cubes with dimensions of $6 \times 6 \times 6\ mm^3$ were used in both systems. Three stilbene cubes were placed in front of the inorganic scintillators to allow for forward scattering interactions and two cubes were placed behind the inorganic scintillators to allow for backscatter interactions. The dimensions of the LYSO(Ce) cubes were $6 \times 6 \times 6$ mm^3 and the dimensions of the $CeBr_3$ cylinders were $6 \times 6\phi$ mm^3.

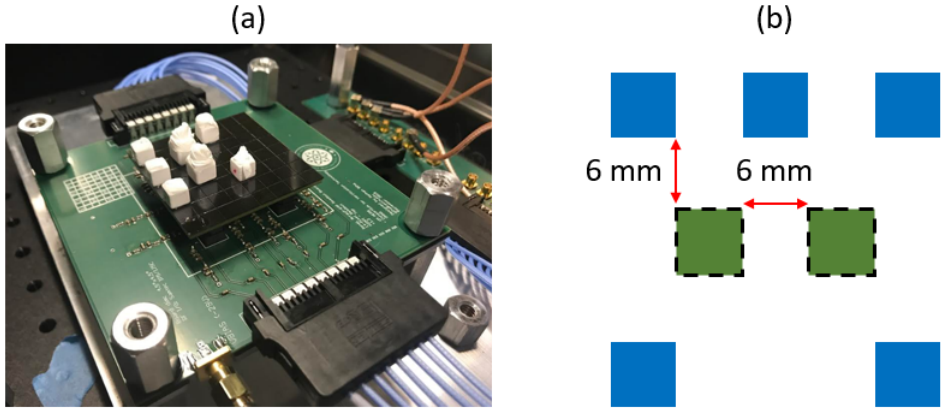

Figure 4.5: A photograph of the miniature version of the H2DPI composed of five stilbene cubes and two LYSO(Ce) cubes is shown in (a). A layout of the scintillators is shown in (b) where blue squares depict the location of the stilbene cubes and green squares with dashed borders depict the location of the LYSO(Ce) cubes.

Both systems shown in Figures 4.5 and 4.6 were tested with a 100 μCi ^{137}Cs source placed 40.64 cm from the center of each system. Spectra were acquired and images were generated from the measured data sets. The resulting images of the ^{137}Cs source shown as a white circle in the images are shown in Figures 4.7 and 4.8 for the LYSO(Ce) and $CeBr_3$ systems respectively.

Both reconstructed images shown in Figures 4.7 and 4.8 have artifacts surrounding the source location that appear as cone projections on either side of the correct

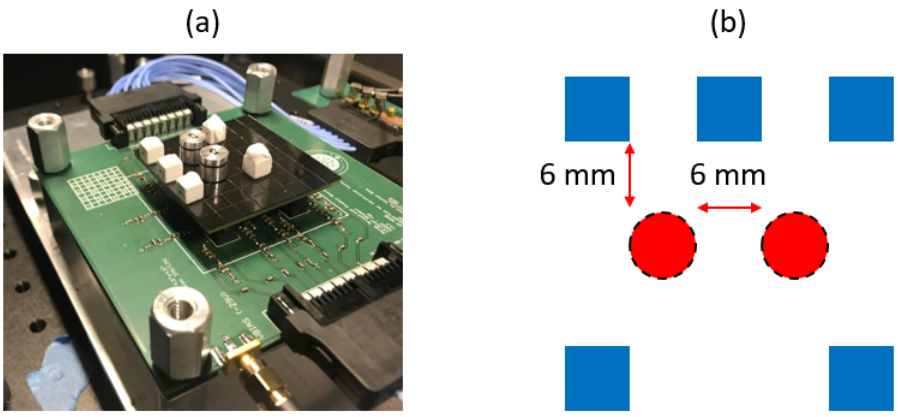

Figure 4.6: A photograph of the miniature version of the H2DPI composed of five stilbene cubes and two $CeBr_3$ cylinders is shown in (a). A layout of the scintillators is shown in (b) where blue squares depict the location of the stilbene cubes and red circles with dashed borders depict the location of the $CeBr_3$ cylinders.

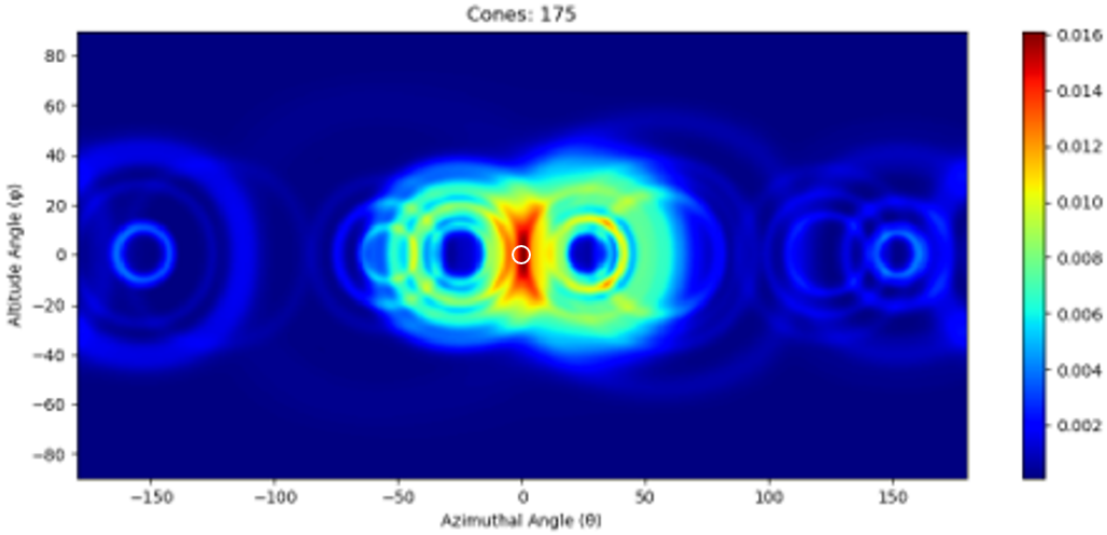

Figure 4.7: Reconstructed SBP image of a ^{137}Cs source 40.64 cm from the center of the miniature H2DPI composed of stilbene cubes and LYSO(Ce) cubes.

source location. These artifacts are due to the number of lever arms in the system and the dominance of the forward-scattering events. The forward scattering events have much lower relative uncertainty compared to the backscatter events, and each inorganic scintillator only has two primary lever arm interactions, which are due

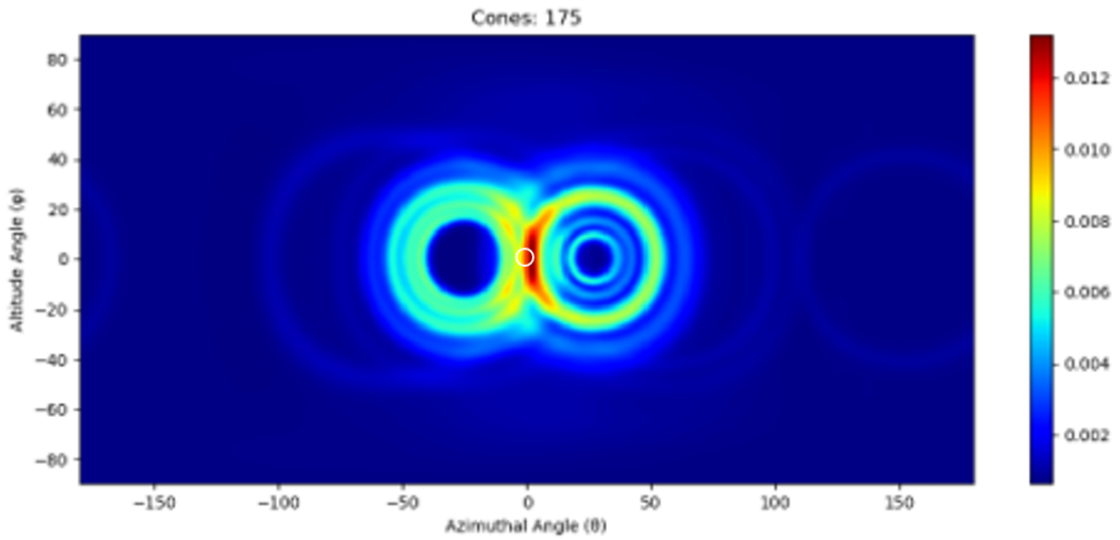

Figure 4.8: Reconstructed SBP image of a ^{137}Cs source 40.64 cm from the center of the miniature H2DPI composed of stilbene cubes and $CeBr_3$ cylinders.

to the two closest stilbene cubes in front of the inorganic scintillators. This result directly shows the importance of having adequate lever arm distributions to obtain a uniform image with minimal artifacts. Figures 4.7 and 4.8 also show the importance of experimental testing. Comparing the two images, Figure 4.7 has substantially more cone projections that do not align with the correct source location compared to Figure 4.8. Background measurements were taken to further investigate the origin of the cone projections that did not align with the correct source location.

Figure 4.9 compares the measured coincident gamma-ray energy spectra for the ^{137}Cs source and the same measured energy spectra due to background radiation. The coincident background energy spectrum is far more substantial in the LYSO(Ce) system than the $CeBr_3$ system. The internal activity of ^{176}Lu in the LYSO(Ce) crystals is yielding a chance coincident spectrum with the stilbene cubes that produces an irreducible background in the reconstructed image. To quantify the impact of this internal radioactivity on the summed photopeak, a signal to background ratio was determined for both spectra shown in Figure 4.9. The signal to background ratio for

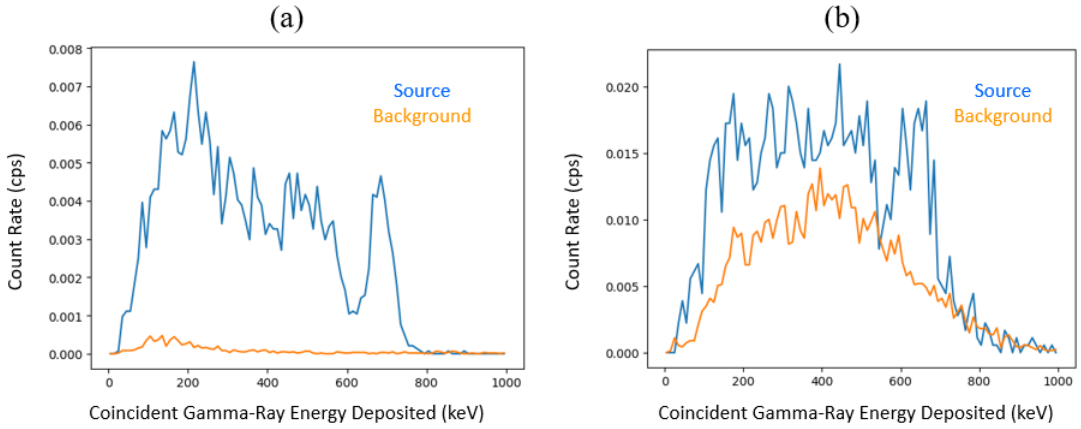

Figure 4.9: Measured coincident gamma-ray energy spectra for a ^{137}Cs source, shown in blue, 40.64 cm from the center of the miniature H2DPI (a) composed of $CeBr_3$ cylinders and (b) LYSO(Ce) cubes. The coincident background gamma-ray energy spectra are shown in orange for both systems.

the $CeBr_3$ system was found to be 131±40 while the signal to background ratio for the LYSO(Ce) system was found to be 1.80±0.22. While the net summed photopeak count rate for the LYSO(Ce) was found to be higher than the $CeBr_3$, 0.0704±0.0080 cps compared to 0.0236±0.0013 cps, the coincident background produces a level of noise that would be unacceptable for a deploy-able system. In a deployed scenario where either weak, shielded or sources far away are present, a user would have to guess if an image artifact due to the internal radioactivity was indeed a source or an actual artifact. To reduce this possibility, the following iteration of the H2DPI was designed using $CeBr_3$ cylinders.

4.3 Optimizing the Placement of $CeBr_3$ in the H2DPI

4.3.1 Constraints on the Placement of the $CeBr_3$

The pixel pattern to be coupled to an ArrayJ-60035-64P-PCB SensL SiPM array was constrained to sixteen of the possible sixty-four pixels with the goal of finding the optimum placement of the $CeBr_3$ scintillators within the layout shown in Figure 4.10. The first constraint placed on the pixel locations was a minimum neutron

flight-path of 1.3 cm in any direction. This constraint was chosen to improve neutron spectroscopy. Rows of pixels were chosen to be offset by one pixel based on previous design analysis [32]. The second constraint was on the number of $CeBr_3$ scintillators. Four pixel locations were chosen for the $CeBr_3$ scintillators to have adequate lever arm distributions to produce more uniform gamma-ray images. Simulations with less than four pixel locations exhibited artifacts because of the relative difference in double-scatter efficiency across the system and minimal lever-arm distributions. More locations for the $CeBr_3$ cylinders were not chosen to maintain neutron imaging efficiency. The placement of $CeBr_3$ was further constrained to the exterior to maintain neutron-imaging efficiency of the system, and $CeBr_3$ cylinders were not placed in adjacent pixels due to physical size constraints. Finally, some degree of symmetry was maintained in the system by not placing all of the $CeBr_3$ cylinders on one side of the detector system. Applying these constraints yields the nine potential layouts shown in Figure 4.11.

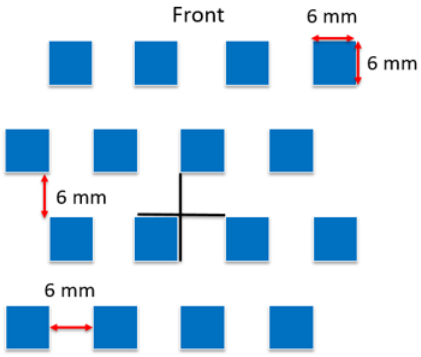

Figure 4.10: Preliminary pixel layout for the placement of scintillators within the 16-pillar H2DPI.

4.3.2 Image Comparison Methodology

Changing the placement of the $CeBr_3$ scintillators within the H2DPI will vary the distribution of scattering angles and lever arms produced by the system. As an example of the impact of this variation, Figure 4.12 shows a simulated azimuthal slice

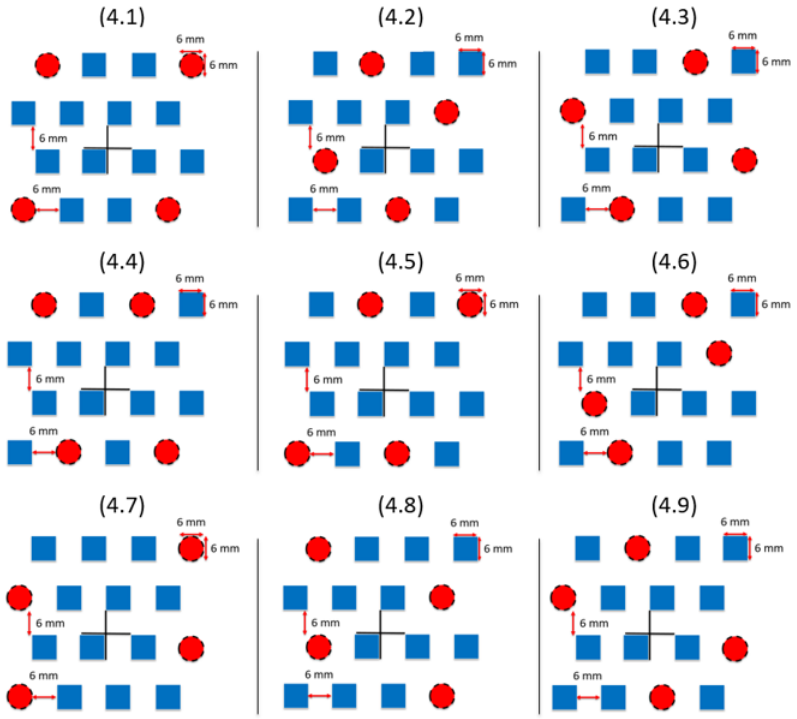

Figure 4.11: H2DPI layouts used in the MCNPX-PoliMi simulations where the blue squares denote placement of stilbene pillars ($6 \times 6 \times 50.5\ mm^3$) and the red cylinders denote placement of $CeBr_3$ scintillators ($6 \times 6\phi\ mm^3$). $CeBr_3$ cylinders were simulated on both the top and bottom SiPM array so that each simulation contained eight $CeBr_3$ cylinders. Each geometry is designated as design 4.1, 4.2, 4.3, ect.

using MCNPX-PoliMi for a reconstructed ^{137}Cs source for both designs 4.1 and 4.2. The light output and interaction location of a given pulse was broadened based off experimentally measured values for the scintillators. Broadening parameters for the stilbene pillars were determined in a similar method to the ones detailed in Steinberger et al. [49]. A back-scatter measurement using a ^{137}Cs source was used to determine the energy resolution of the stilbene pillars at 478 keV. This measurement and results are detailed in Section 5.6.1. The average energy resolution was found to be 11.2±0.5 %. The b parameter of

$$\text{FWHM}(E) = a + b\sqrt{E + cE^2}, \tag{4.2}$$

was fit for the Gaussian Energy Broadening (GEB) term to broaden the light output values in the stilbene pillars. In Equation 4.2, a, b and c are fit parameters, E [MeV] is the total light output or total energy deposited and FWHM is the full width at half maximum. All three GEB factors were fit for the $CeBr_3$ cylinders as measured with the system shown in Figure 4.2. A ^{137}Cs and a ^{22}Na source were used to fit the GEB factors for the top and bottom cylinders. The measured a, b and c parameters were found to be -6.56×10^{-05}, 0.0507 and -0.2395 respectively for the bottom cylinder and -5.02×10^{-05}, 0.0468, -0.1557 respectively for the top cylinder. Applying these uncertainties to the simulation produced the broadened reconstructions shown in Figure 4.12.

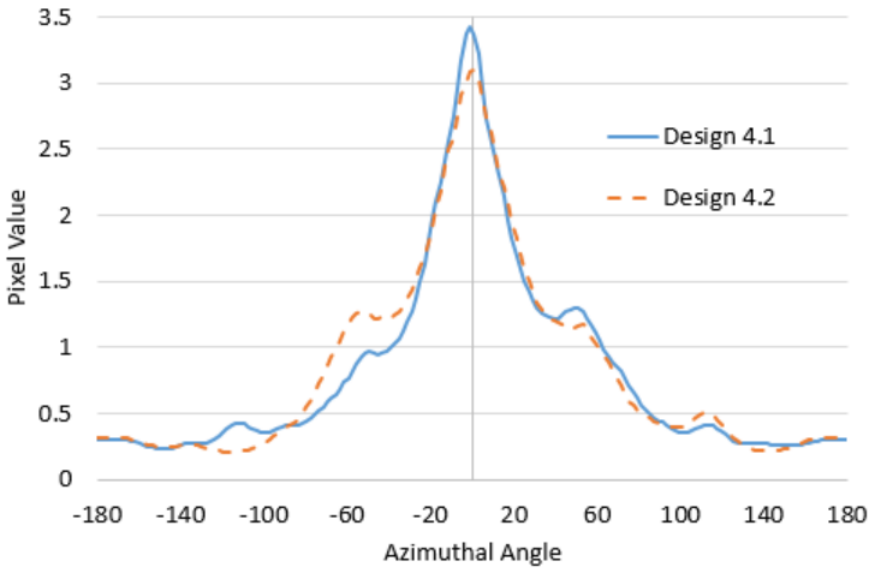

Figure 4.12: Azimuthal slices from SBP images generated from designs 4.1 and 4.2. The ^{137}Cs source was simulated at (0^o, 0^o).

Design 4.1 yields a higher intensity image, smaller FWHM and less artifacting across the image relative to design 4.2. To quantitatively assess the image performance between these simulated images, the structural similarity (SSIM) of each image was measured using a step function as the reference image [69, 70]. The SSIM index compares the luminance, contrast, and structure for a reference image x and mea-

sured image y. A step function was chosen as the reference image as a step function represents a pseudo-idealized system response. The step function was set to equal the maximum value of the simulated image for a 3 pixel radius in the simulated source location and equal to the minimum value of the simulated image for all other pixel locations. This index has been used in medical imaging applications [71], streaming services [72, 73] and to design coded aperture imaging systems [74, 75]. The SSIM index is computed using

$$\mathrm{SSIM}(x, y) = \frac{(2\mu_x\mu_y + C_1)(2\sigma_{xy} + C_2)}{(\mu_x^2 + \mu_y^2 + C_1)(\sigma_x^2 + \sigma_y^2 + C_2)}, \tag{4.3}$$

where μ is the mean of the pixel values, σ_{xy} is the correlation coefficient between the two images, σ is the standard deviation of the pixel values, and C_1 and C_2 are constants to help avoid instabilities. As an example, Figure 4.13 shows this methodology applied to a Gaussian distribution where the SSIM index is solved between the "measured image", y, and a "reference image", x. Local SSIM values are computed to assess differences over the entire image. The local SSIM values plotted as red squares in Figure 4.13 were computed for a 3-pixel radius where each pixel was weighted by an integral normalized Gaussian distribution. For the simulated image analysis, local SSIM values were computed for a 10-pixel radius for each pixel where each pixel was weighted by a normalized and converged point spread function developed in Section 3.2. The average of all the local SSIM values, MSSIM, is analyzed to determine which system design produces the best performance. The MSSIM value closer to 1.0 means that it is a better match.

Analyzing Figure 4.13 shows how the SSIM value changes across the image. Below an angle of -30^o and above an angle of 30^o, the SSIM returns a value close to 1.0. This value drops as the Gaussian distribution begins to deviate from the step function and then returns to a value close to 1.0 when the step function matches the peak of the Gaussian distribution. Averaging these SSIM values yields a quantitative metric for

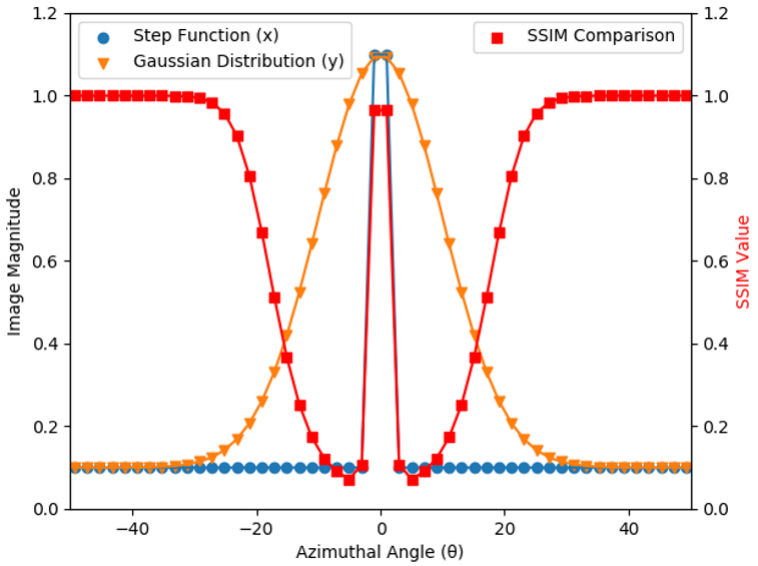

Figure 4.13: Azimuthal slice showing the SSIM result for a "measured image", y, and a "reference image", x. The "measured image" is a Gaussian distribution meant to represent a point spread function generated in simulation.

how well these images match.

SBP images, such as the ones used to generate the slices shown in Figures 4.12, were generated for each layout shown in Figure 4.11 for three sources at angular locations (azimuthal angle, altitude angle): $(0^o, 0^o)$, $(-45^o, 0^o)$ and $(-90^o, 0^o)$ at a distance of 45 cm from the center of the system. Each one of these simulated images was compared to a step function to determine which system geometry best matched a step function response.

4.3.3 Image Comparison Results

The MSSIM values for the three source locations and nine system designs shown in Figure 4.11 are shown in Figure 4.14.

Design 4.7 yielded the best performance for the ^{137}Cs at $(0^o, 0^o)$. Design 4.1 is within two standard deviations of design 4.7 for the ^{137}Cs at $(0^o, 0^o)$. Designs 4.1 and 4.5 are within a single standard deviation of each other for the best performance for the ^{137}Cs at $(-45^o, 0^o)$. Finally, designs 4.1, 4.4, 4.5 and 4.8 yielded results within a

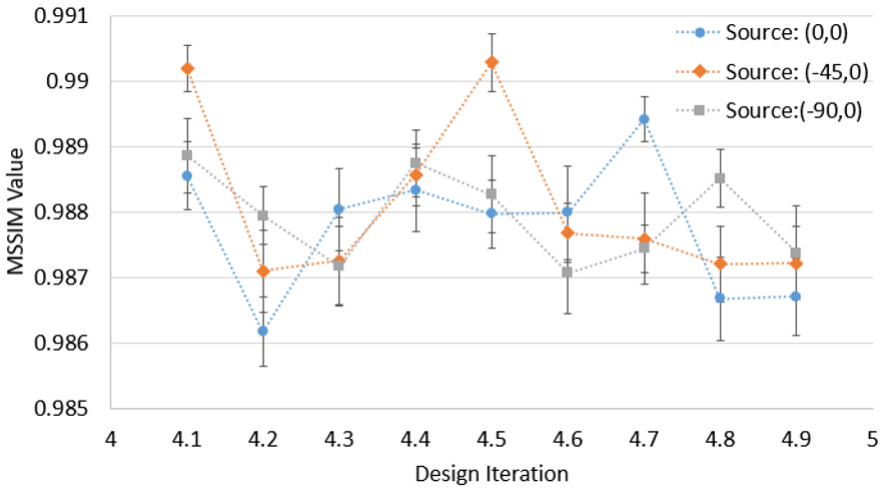

Figure 4.14: MSSIM values for each design iteration at the three source locations. Uncertainty bars denote a single standard deviation generated from bootstrapping 100 images composed of 5000 simulated cone projections.

single standard deviation of each other for the ^{137}Cs at (-90^o, 0^o). The error bars of the MSSIM values shown in Figure 4.14 are solved by taking the standard deviation of 100 bootstrapped images each composed of 5,000 cone projections.

4.3.4 Efficiency Analysis

Intrinsic efficiency of imageable neutron and gamma-ray interactions for each design was also assessed. Surface current tallies were placed on a surface directly around the simulated design to determine the intensity of incident neutrons or gamma rays. The number of imageable events was then divided by the number of incident particles to determine the intrinsic efficiency of the system. This analysis was performed for neutrons from a ^{252}Cf source and gamma rays from a ^{137}Cs with the sources at the following locations: (0^o, 0^o), (-45^o, 0^o) and (-90^o, 0^o) at a distance of 45 cm from the center of the system. Results are shown in Figures 4.15 and 4.16.

There is a direct trade off between the imaging efficiencies of the potential layouts and the imaging performance. Design 4.7, for instance, has poor gamma-ray imaging efficiency but good neutron imaging efficiency relative to the other designs, and

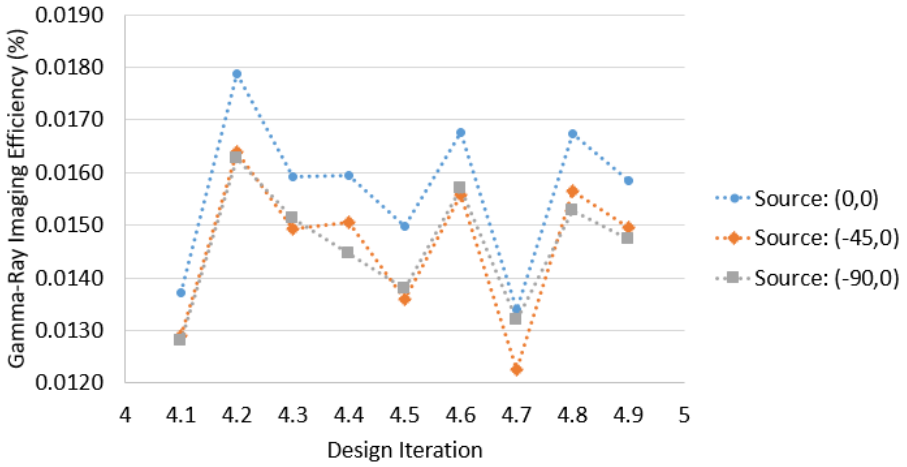

Figure 4.15: Simulated gamma-ray imaging efficiency for a ^{137}Cs source 45 cm from the 16-pillar iteration of the H2DPI.

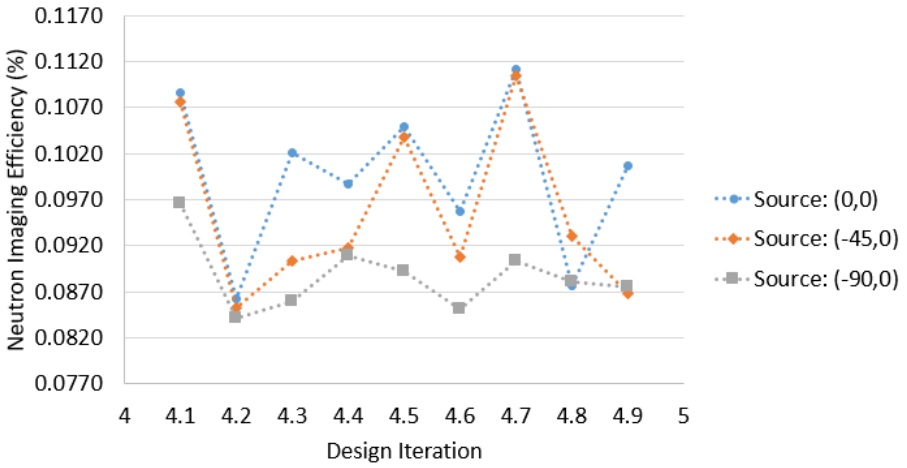

Figure 4.16: Simulated neutron imaging efficiency for a ^{252}Cf source 45 cm from the 16-pillar iteration of the H2DPI.

yielded the best MSSIM value for the ^{137}Cs source at (0^o, 0^o). This trade off effect holds for design 4.1 as well, which performed in the top two responses for each source location but has a trade off between the gamma-ray and neutron imaging efficiency.

4.4 Conclusions

The results presented show the impact of system geometry on imaging performance for a ^{137}Cs source imaged using a combination of inorganic and organic scintillators.

The SSIM index was used to assess relative image quality and produced an optimum geometry for imaging gamma-ray sources. The analysis showed that design 4.1 overall yielded the best gamma-ray imaging performance relative to the other designs. In addition, this design yielded one of the lower intrinsic gamma-ray imaging efficiencies and one of the higher intrinsic neutron imaging efficiencies. Design 4.1 was pursued in the 16-pillar prototype H2DPI. Characterization results of this design are detailed in Chapter V.

CHAPTER V

Characterizing the 16-Pillar H2DPI

The optimized design detailed in Chapter IV composed of twelve stilbene pillars and eight $CeBr_3$ cylinders was built. The system was then thoroughly characterized to accurately propagate uncertainties for source reconstruction. This chapter details the experiments and methodology used in the characterization of the system response.

5.1 Overview of the 16-Pillar H2DPI

Twelve pillars of Inrad Optics stilbene with dimensions of ($6 \times 6 \times 50.5$ mm^3) and eight cylinders of Advatech-UK $CeBr_3$ with dimensions of (6×6 Ø mm^3) were coupled to two arrays of ArrayJ-60035-64P-PCB SensL SiPMs [68] using ($6 \times 6 \times 0.5$ mm^3) EJ-560 optical interfaces [55]. The stilbene pillars were coupled to the SiPMs on both ends to allow for a duel-readout and position reconstruction across the length of the pillar [52, 45, 49, 51]. The $CeBr_3$ cylinders were independently coupled to single SiPM pixels. Figure 5.1 shows a photograph of the assembled prototype. The $CeBr_3$ cylinders were coupled to the top and bottom pixels for each respective position and are held in place by an aluminum structure containing springs that apply constant pressure to the cylinders so that they are coupled to the pixels.

Custom electronics were developed to apply voltage bias and to read the signals from the SiPM arrays. The electronics have been previously detailed and discussed

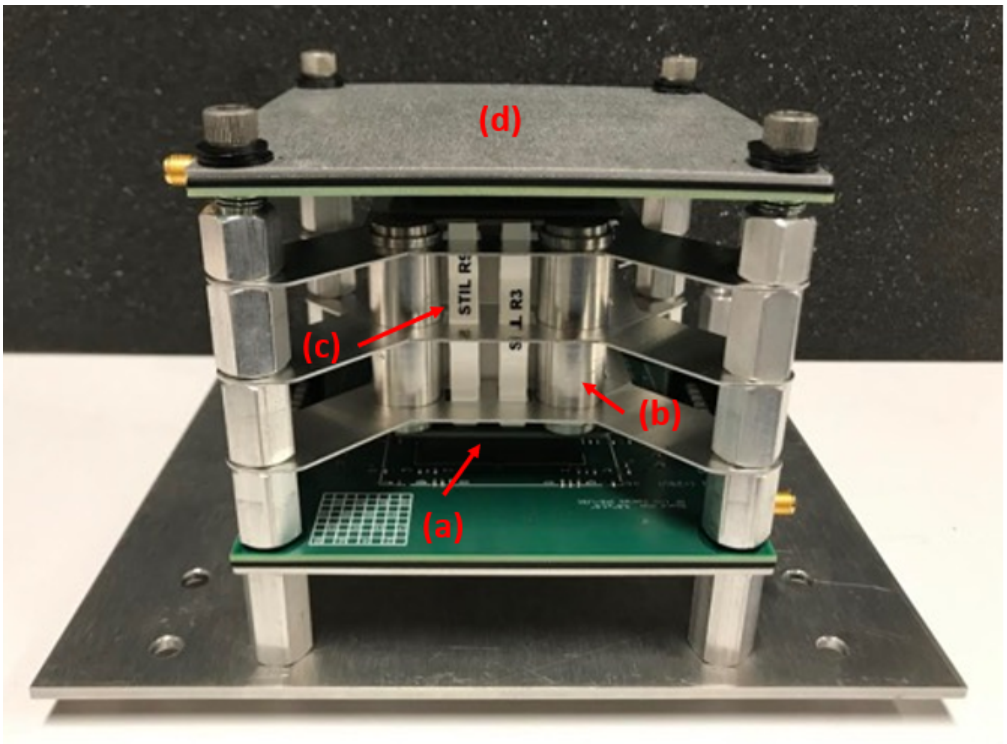

Figure 5.1: Photograph of the prototype 16-pillar H2DPI composed of (a) two ArrayJ-60035-64P-PCB SensL SiPMs, (b) eight $CeBr_3$ cylinders, (c) twelve stilbene pillars wrapped in PTFE and (d) two custom printed circuit boards with added teflon and aluminum support structure [1].

by Steinberger et al. and Giha et al. [51, 1]. The signals from each SiPM is read out to one of two v1730 CAEN digitizers with a 14-bit resolution, 2.0-V dynamic range, and 500-MHz digitization rate that were used for measuring sources with the H2DPI. An applied voltage value of 29.6 V was set to the relevant pixels by a KEYSIGHT E3649A Dual Output DC Power Supply.

5.2 Gamma-Ray Light-Output Calibration

5.2.1 Calibration of the Stilbene Pillars

Initial pulse integral (V-ns) to light output (keVee) calibration for the stilbene pillars was performed with a 100 μCi ^{137}Cs source [76]. SiPM output pulse integration was performed using a rectangular integration approximation from the beginning

of the rising edge to the end of the falling edge. The beginning of the rising edge is the digitized point before the rising edge that is equal to 5 % of the pulse height and the end of the falling edge is the point after the falling edge is equal to 1 % of the pulse height value. The pulse height value is defined as the maximum digitized point after the waveform has been baseline subtracted. These points were chosen as the integration bounds for the pulse integral so that noise from the baseline was not integrated in the pulse integral value. The integrals of the SiPM outputs from both sides of each scintillator pillar were summed to give the total integral of an interaction in a given pillar for a given event. The calibration point along the Compton edge was found using a similar method detailed by Norsworthy et al. [77]. An unbroadened pulse height distribution from a ^{137}Cs source was simulated using MCNP6 for one of the pillars of stilbene. The unbroadened spectrum was broadened to match a measured ^{137}Cs spectrum and the intersection of the unbroadened Compton edge with the broadened spectrum yielded the calibration point of 63 % as shown in Figure 5.2. The simulated spectrum used to generate this calibration point did not account for electron leakage from the scintillator and assumed constant resolution, which is why there is disagreement between the experimental and simulated Compton continuums. Accounting for the electron leakage and resolution provides a more accurate simulation model but does not significantly alter the calibration point.

5.2.2 Calibration of the $CeBr_3$ Cylinders

Unlike stilbene, $CeBr_3$ has the density and effective atomic number for gamma rays to undergo photoelectric absorption. Calibration can then be performed by fitting a Gaussian distribution to a measured photopeak from a given source. Assuming that a system has a linear response allows the calibration solely using photopeaks to determine the conversion from pulse integral (V-ns) to energy deposited (keV). The pixels of the J-series SiPMs used in the H2DPI are composed of 22,292 microcells [68],

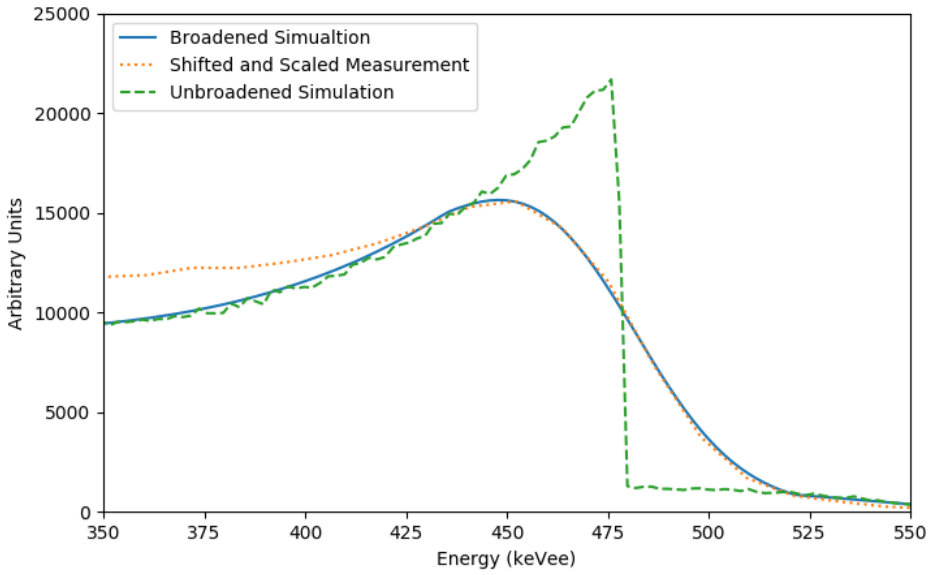

Figure 5.2: The calibration point for the $6 \times 6 \times 50$ mm^3 stilbene pillars used for the following analysis. The green dashed line shows the unbroadened simulated pulse height distribution from ^{137}Cs gamma rays incident on the detector. The solid blue line and dotted orange line show the broadened simulation and calibrated measured pulse integral distributions.

but the light output for $CeBr_3$ is 60,000 $\frac{photons}{MeV}$. At the photopeak for ^{137}Cs, $CeBr_3$ will on average produce nearly 40,000 photons. This high light output produces the good energy resolution that has been previously measured, but also introduces a non-linearity response of the scintillator. The microcells within the J-series pixel have a recharge time constant of 50 ns. Having a higher number of photons produced than the number of microscells means that some photons have a higher probability of being absorbed or escaping because the microcells require a time to recharge; creating this nonlinear effect. Calibrating a measured ^{137}Cs spectrum using the backscatter peak, the Compton edge and the photopeak as calibration points shows the nonlinear response of the system (Figure 5.3). The Compton edge calibration point was determined using the same method discussed in Section 5.2.1 and determined to be 62% of the Comtpon edge. Figure 5.3 compares the individual calibration points with a line that was made by only calibrating on the photopeak of the distribution. Not accounting for the nonlinear response of the system would significantly over es-

timate the Compton edge and backscatter peak values. Accurately calibrating these parameters, however, yields Figure 5.4.

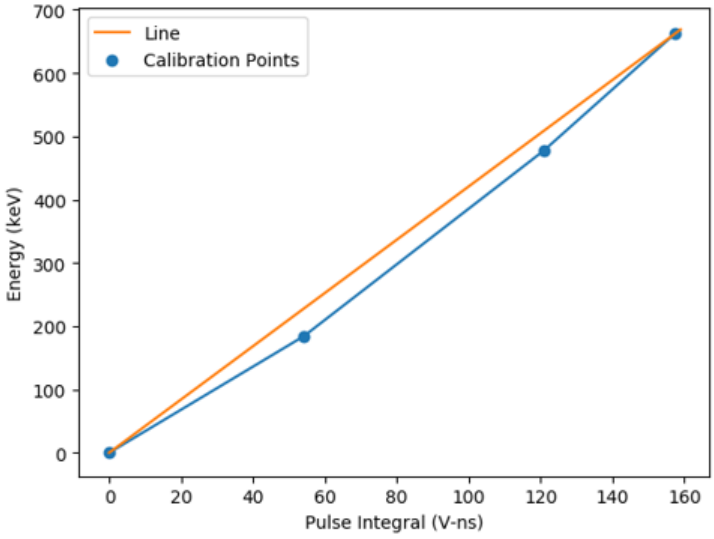

Figure 5.3: Calibration points from a ^{137}Cs source using the backscatter peak, Compton edge and photopeak as calibration points. The data are compared with a linear fit for just the photopeak.

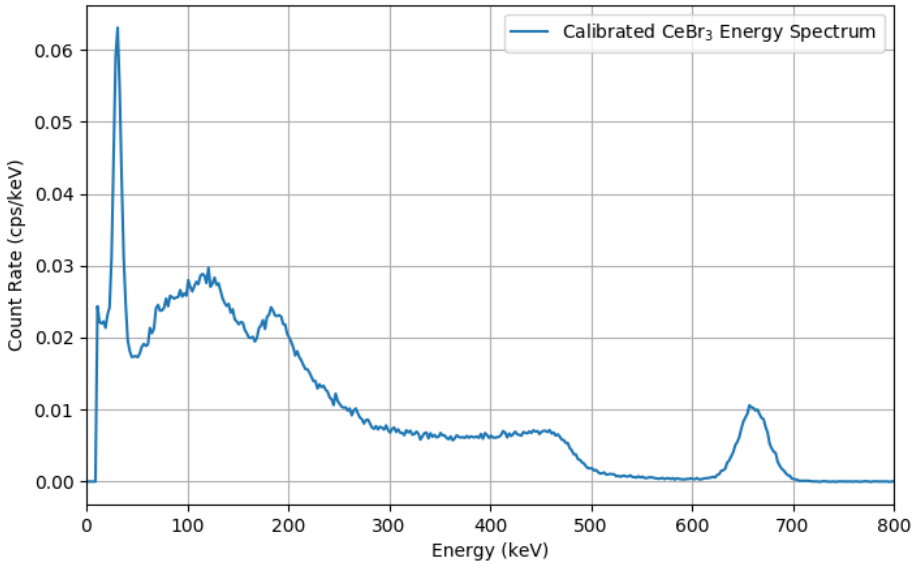

Figure 5.4: Calibrated experimental gamma-ray response from a ^{137}Cs source 58.34 cm from the center of the H2DPI for a single $CeBr_3$ cylinder within the H2DPI.

Gamma-ray imaging is dependent on the coincident interactions between the stil-

bene pillars and the $CeBr_3$ cylinders. The majority of the interactions within the $CeBr_3$ cylinders for these coincident events will be depositing less than the Compton edge value for the energy of the incident gamma ray. Because the reconstruction is dependent on the summation of the energies in both interactions, it is necessary that the energy deposited is accurately determined. Not accounting for this linearity would over estimate the incident gamma-ray energy and not accurately reconstruct the sources.

5.3 Time Resolution Calibration of the Stilbene Pillars

A 100 μCi ^{22}Na source was centered between two pillars of stilbene and a coincident measurement was taken for 30 minutes to determine the time resolution of the system. Digital constant fraction discrimination (DCFD) was used to determine the start time of the pulses. DCFD determines the start time of a pulse by finding where some fractional value of the amplitude occurs along the rising edge of the pulse [78, 43, 79]. The DCFD value was optimized to 20 % using the optimization method described in Steinberger, et al. [79]. In addition, all pulses above an approximate 30 keVee threshold were analyzed. Multiple methods for selecting the start time of the event were tested to see which yielded the best time resolution. The methods tested included using the start time of the larger pulse, using the earlier start time of the two pulses and using the average start time of the two pulses. It was found that taking the average start time yielded the best time resolution (standard deviation of the distribution from the full width at half maximum (FWHM)) of 217$\pm$2 ps. The time difference distribution of the measurement using the average start time is shown in Figure 5.5. The next best method, choosing start time from the larger pulse, yielded a time resolution of 342$\pm$3 ps. We assumed for the following analysis that the measured time resolution is constant as a function of interaction location, energy and pairs of bars.

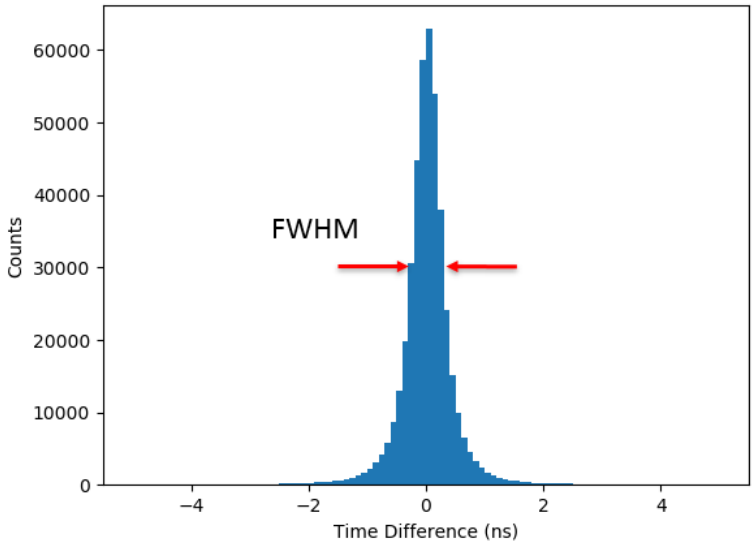

Figure 5.5: Time difference histogram with a DCFD fraction of 0.2 from a Na-22 source between two 6×6×50 mm^3 stilbene pillar with J-Series SensL SiPMs coupled to both ends.

5.4 Pulse-Shape Discrimination Calibration of the Stilbene Pillars

PSD was characterized using a digital charge comparison method where the ratio of the integral of the tail of the pulse over the integral of the total pulse is used to determine if an interaction was from a neutron or gamma ray [80, 81, 82, 42]. This method requires the optimization of three parameters: the time where the total integral begins, the time where the tail integral begins, and the time where both integrals end. These parameters were varied until an optimum value set was found between a light output range of 100-150 keVee. The optimized set of parameters was determined by choosing the set that yielded the highest figure-of-merit (FOM). The FOM,

$$\text{FOM} = \frac{u_n - u_\gamma}{\text{FWHM}_n + \text{FWHM}_\gamma}, \tag{5.1}$$

is a measure of how well neutrons and gammas can be separated. In Equation 5.1, u_n and u_γ denote the center of the Gaussian fits to the neutron and gamma distributions while FWHM_n and FWHM_γ denote the FWHM for the neutron and gamma distributions. Figure 5.6 shows Gaussian fits to the neutron and gamma portions for a histogram of the tail to total ratios for pulses with light output between 50-100 keVee. The distributions in Figures 5.6 was measured using a ^{252}Cf source. Since two pulses are acquired for each interaction, the tail regions (tail integral start time to integral end time) and total regions (total integral start time to integral end time) are summed in quadrature before taking a ratio as described by:

$$\text{Ratio} = \frac{\sqrt{\text{Tail}_1^2 + \text{Tail}_2^2}}{\sqrt{\text{Total}_1^2 + \text{Total}_2^2}}. \tag{5.2}$$

Summing the tails and totals in quadrature yielded the best PSD performance. Figure 5.7 shows examples of the integration regions on measured output pulses for a stilbene pillar. The parameters were varied to determine an optimum FOM. The parameters that yielded the greatest separation for the neutron and gamma distributions were a total integral start time of 0 ns relative the maximum value of the pulse, a tail integral start time of 60 ns relative to the maximum value of the pulse and an integral end time of 370 ns relative to the maximum value of the pulse. These parameters yielded average FOMs between all eight pillars of 1.25±0.05 for a light output range of 50-100 keVee and 1.74±0.06 for a light output range of 100-150 keVee.

Gamma-ray misclassification in neutron imaging can potentially reconstruct gamma-neutron coincident events that may add noise or artifacts to a measured image. Setting a classification threshold as a function of misclassification rate can mitigate this potential problem and yield necessary data to be able to model the response of the system. Figure 5.7 shows a ratio versus light output distribution with several classification lines denoted as some number of σ or standard deviations. The standard deviations, as shown in Figure 5.6, are based on the Gaussian fits to the gamma-ray

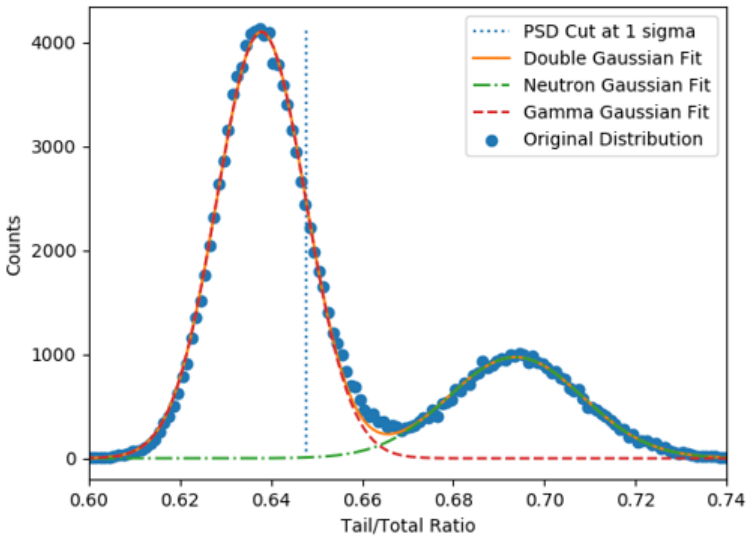

Figure 5.6: Tail/total ratio histogram for a 6×6×50.5 mm^3 stilbene pillar with J-Series SensL SiPMs coupled to both ends for a light output range of 50-100 keVee.

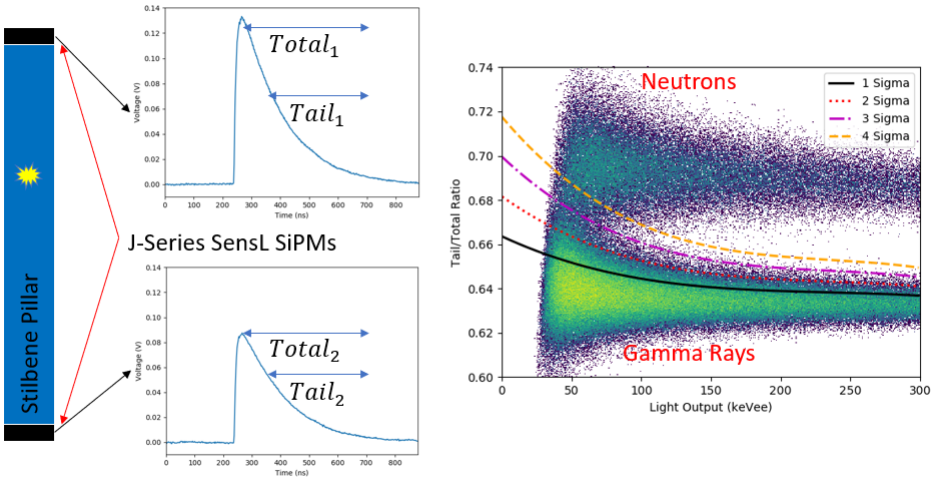

Figure 5.7: Tail/total ratio versus light output for a 6×6×50.5 mm^3 stilbene pillar with J-Series SensL SiPMs coupled to both ends with overlaid PSD cuts.

and neutron distributions. Generally these misclassification rates are set until separation between the gamma-ray and neutron bands is achieved. For the stilbene pillars within the H2DPI, separation occurs at about 75 keVee. For gamma-ray imaging, the same process is performed to classify gamma-ray pulses, but the misclassification is set for the neutrons instead of the gamma rays.

5.5 Neutron Light-Output Calibration

The conversion from light output to energy deposition is nonlinear for neutron interactions [83, 59]. Non-linearity results from the higher charge density from the ionizing track. Protons have a higher stopping power relative to electrons that causes more singlet state quenching and triplet state annihilation [58, 84], therefore producing different pulse shapes between neutron interactions compared to gamma-ray interactions. In addition, the anisotropic response of crystalline organic scintillators to heavy charged particles has been well documented [85, 86] and there has been a significant effort to characterize the response of stilbene due to its viability as a fast-neutron detector [87, 88, 2]. The anisotropic response of stilbene is significant enough that it can be exploited to localize a neutron source by rotating stilbene crystals and analyzing the relative change in count rate [89, 90, 91]. This change in response as a function of crystal direction, however, has not been analyzed for NSCs that may require a directionally-dependent correction. The following analysis was performed to measure the light-output distributions along the three crystal planes of stilbene.

Three TOF measurements were performed to characterize the light output for each crystal plane of stilbene. The experimental setups for each measurement are shown in Figure 5.8. A 25-mm diameter Hamamatsu H10580 PMT biased at -1000 V coupled to a ($25.4\phi\times$ 25.4 mm^3) stilbene cylinder was used as the start detector to tag fission events to create a source of quasi-mono-energetic neutrons by cutting on the TOF between the start detector and the stilbene pillars [92, 59, 93]. Care was taken in the design of the experimental setups to ensure that the center of the ^{252}Cf source was aligned along the axes of the center of the H2DPI. The activity of the ^{252}Cf source was 2.00 mCi at the time of the measurements, which yielded a neutron emission intensity of approximately 8.6×10^6 $\frac{n}{s}$. Each experimental setup had the ^{252}Cf source aligned along one of the axes by using an optical breadboard. The flight paths from the source to this center position were 50.8 cm for the source

at the angular position of (0^o,-0.8^o), 50.8 cm for the source at the angular position of (-90^o,-0.8^o), and 56.48 cm for the source at the angular position of (0^o,90^o). For the calculations of the flight paths, the center positions of the scintillators were used. The interaction location was reconstructed for the above-system measurement using a similar method to Ruch et al [52] and is explicitly detailed in Section 5.7. Each source position was measured for approximately 96 hours. ^{137}Cs measurements were performed approximately every 24 hours to account for gain change in the system over the course of the measurements.

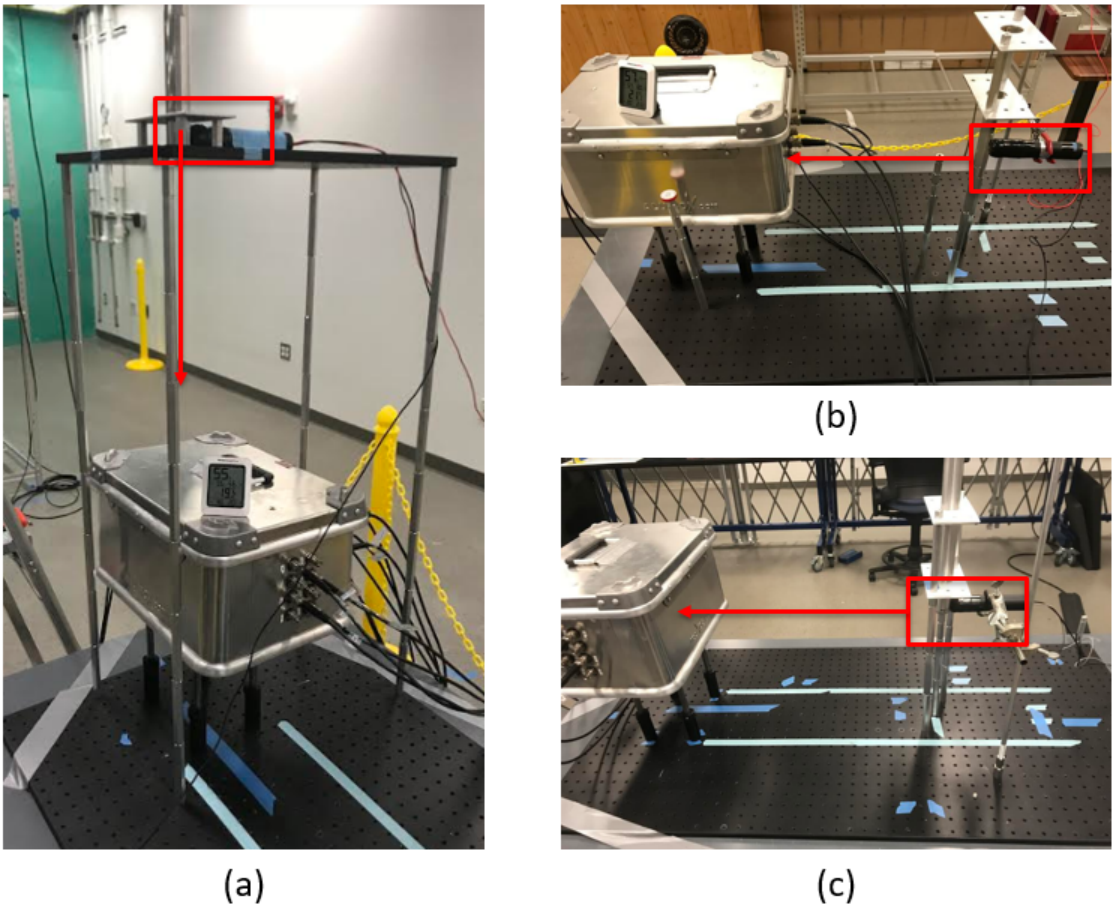

Figure 5.8: Experimental TOF setups for measuring the light output along the three crystal axes of stilbene, where the ^{252}Cf source is (a) above the system measuring L_b, (b) to the left of the system measuring majority $L_{c'}$, and (c) in front of the system measuring majority L_a. The start detector is outlined in a red box and the neutron flight path is shown as a red arrow.

Processing of coincident events between the start detector and a given pillar in the H2DPI was performed in the following manner. The pulse shape of the interaction in the start detector was checked to ensure a gamma-ray interaction by a charge integration method [81]. The pulse shape in the stilbene pillar was then analyzed to ensure a neutron event, where the discrimination line was chosen based on the gamma-ray misclassification rate. A misclassification rate of 0.13% was chosen for events below 150 keVee. The TOF of the gamma-neutron events were then grouped based on the time resolution of the system to generate quasi-mono-energetic neutrons. The average time resolution between the start detector and the stilbene pillars was found to be 783±15 ps (FWHM). These values were experimentally determined by a coincident measurement using a ^{22}Na source. Once the TOF groups were made, the mean TOF value was converted to energy and a pulse integral distribution from the TOF group was produced. Figures 5.9 and 5.10 show the calibrated light-output spectra for two of these TOF groups for the front pillar of stilbene in the prototype system. Figure 5.9 shows the light-output spectrum for neutrons with energies from 1.14±0.02 to 1.20±0.02 MeV and Figure 5.10 shows the light-output spectrum for neutrons with energies from 4.56±0.18 to 5.00±0.20 MeV. The uncertainty for the limits of the reported energy ranges include time resolution and position resolution between the start and stop detectors.

A Gaussian distribution was fit to the smoothed derivative of the end point of the light-output distribution. By analyzing the maximum light output for a given TOF bin, only protons recoiling along the crystal plane are analyzed. The mean of the Gaussian was taken as the light output for a full-energy deposition from an elastic-scattering interaction of that energy neutron [93, 94]. It should be noted that neutron multiple-scattering events where the neutron deposits its full energy will produce a lower light-output event than a single-scattering event where the neutron deposits its full energy [95, 88]. To assess the impact of multiple scattering, MCNPX-PoliMi sim-

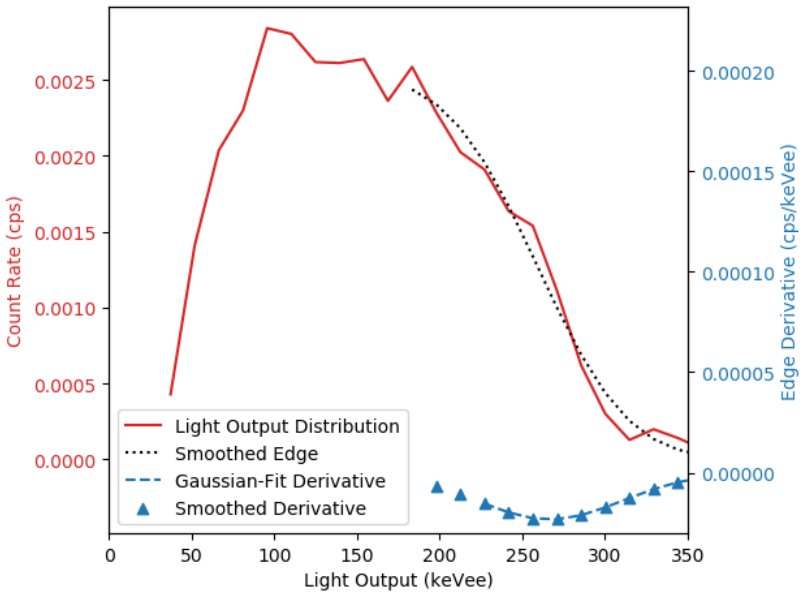

Figure 5.9: Light output distribution for neutrons with energies from 1.14±0.02 to 1.20±0.02 MeV. The measured light output for this distributions was found to be 260±41 keVee where the reported uncertainty is the standard deviation of the fit Gaussian distribution.

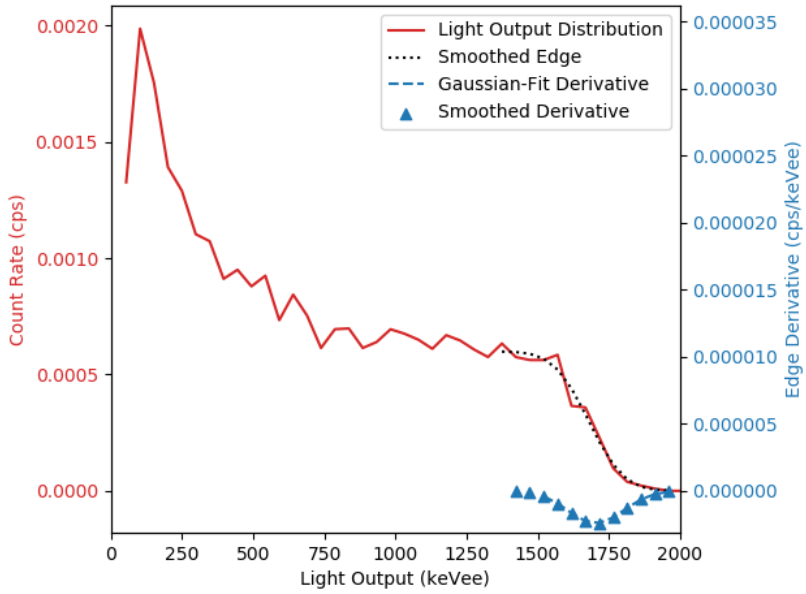

Figure 5.10: Light output distribution (shown as a red line) for neutrons with energies from 4.56±0.18 to 5.00±0.20 MeV. The measured light output for this distributions was found to be 1682±104 keVee where the reported uncertainty is the standard deviation of the fit Gaussian distribution.

ulations were performed with a ^{252}Cf centered 50.8 cm from the center of the H2DPI. Single and multiple scattering events were recorded and analyzed. It was found that approximately 17% of events above a threshold of 50 keVee consisted of two-neutron scattering interactions within the same pillar. Of those 17%, approximately 58% of those events consisted of the neutron scattering off two hydrogen atoms while 41% consisted of the neutron scattering off a hydrogen and carbon atom. The remaining percentage consisted of events where a neutron and gamma ray interacted with the same pillar. For the hydrogen double-scattering events, we found that there was a 15% change in light output relative to the higher-energy interaction. For the hydrogen and carbon double-scatter events, we found that there was a 1.8% change in light output. Results from these simulations did not show that there was a considerable impact of multiple scattering on the light-output endpoint for the TOF groups.

Once the electron equivalent energy of the full-energy deposition for each TOF bin was determined for all neutron energies, the data were fit with a semi-empirical function based on Birks' formula [58, 77, 93]:

$$L(E) = \int_0^E \frac{a}{1 + b(\frac{dE'}{dx})} dE'. \tag{5.3}$$

In Equation 5.3, $L(E)$ is the light output in MeVee, $\frac{dE'}{dx}$ is the particle stopping power in the interaction medium and a and b are fit parameters. The uncertainties in the fit parameters were ultimately calculated by splitting the measured data into 12 sequential sub-measurements for the L_b and L'_c crystal axes and 14 sequential sub-measurements for the L_a crystal axis, fitting each sub-measurement (obtaining a set of 12 or 14 a and b values for each crystal axis), and finally taking the sample standard deviation of the fit parameters for each set. The reported values of a and b are the means of the respective sub-measurements, shown in Table 5.1 with associated uncertainties. Figure 5.11 shows an overlay of the fit with all measured data points

for the $L_{c'}$ crystal axis of stilbene. Figure 5.12 shows the three fitted curves for the three crystal planes.

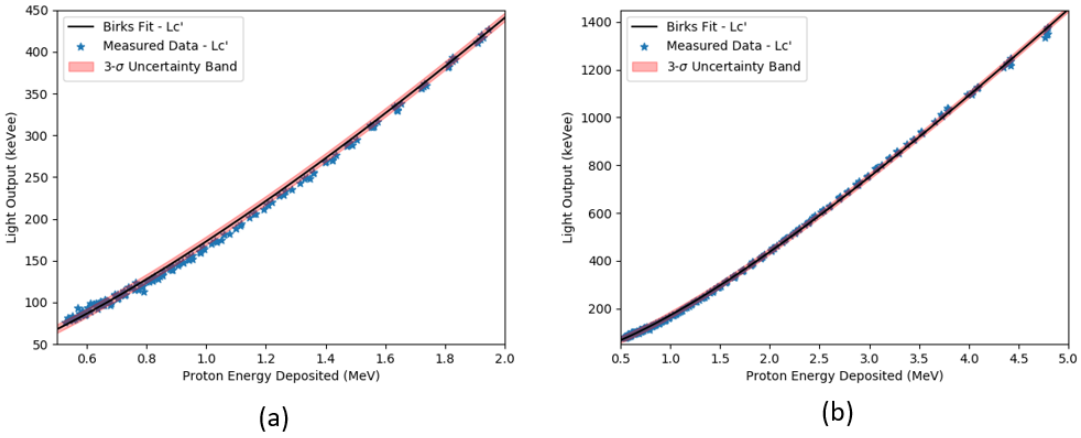

Figure 5.11: Measured $L_{c'}$ light output data fit with the Birks' function shown for proton energy depositions from 0.5-2.0 MeV (a) and 0.5-5.0 MeV (b).

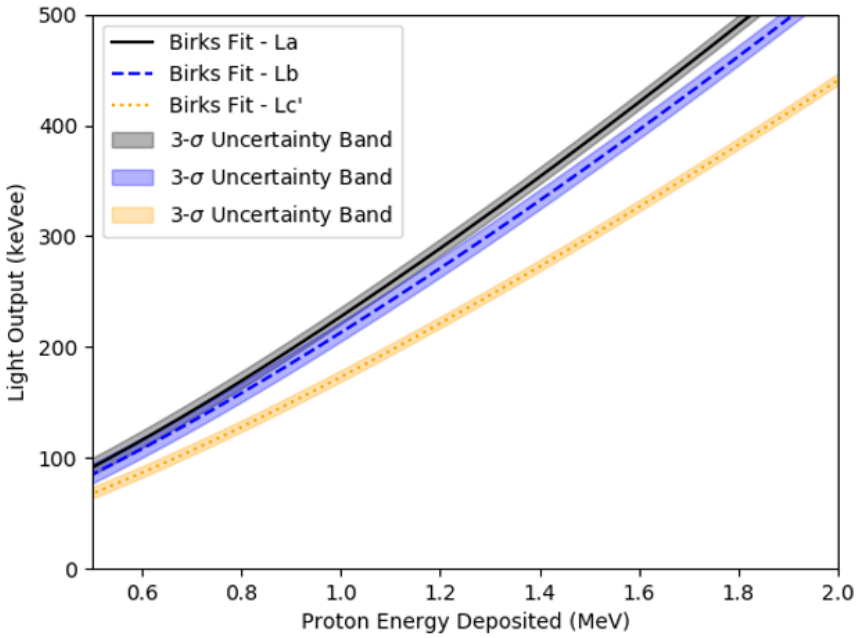

Figure 5.12: Overlaid fits to the measured light output curves for the three crystal planes of stilbene.

As previously detailed, there has been a substantial effort to characterize the response of stilbene to assess its feasibility in nuclear security applications [87, 88, 2]. The ratio of the measured light-output curves are compared to the most recent

Table 5.1: Birks' fit parameters for the three light output curves.

Light Output Curve	a $[\frac{MeVee}{MeV}]$	b $[\frac{cm}{MeV}]$
L_a	0.542 ± 0.016	3.05 ± 0.19
L_b	0.527 ± 0.019	3.26 ± 0.23
$L_{c'}$	0.487 ± 0.011	4.05 ± 0.18

published data on the anisotropic response by Weldon et al in Figure 5.13. Light-output linearity and the impact of quasi-monoenergetic neutrons on the absolute value of the light output distribution were not assessed in this manuscript, which may impact the magnitude of the measured light output. Taking the ratio between the light output curves normalizes out these affects and allows the curves to be directly compared. The comparison shown in Figure 5.13 agrees well for the L_a/L_b ratio, while it appears the results from the measurements detailed above yield an $L_{c'}$ curve with a higher magnitude than that found by Weldon [2]. The $L_a/L_{c'}$ and $L_b/L_{c'}$ ratios between the two data sets are within two to three standard deviations of each other. The general shapes of the ratios, however, agree well.

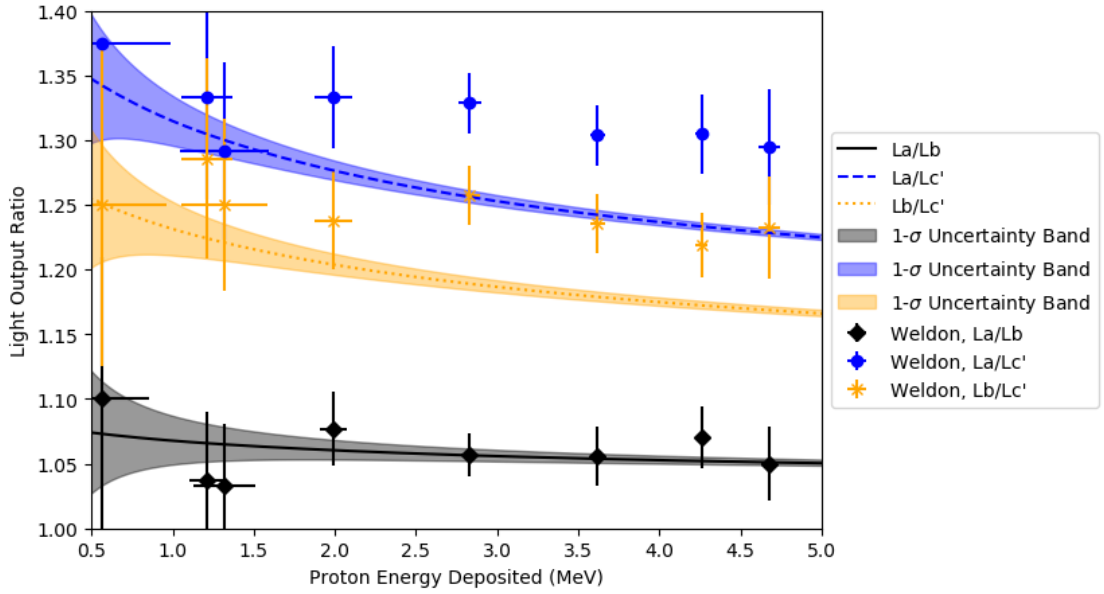

Figure 5.13: Light output ratios for the three measured crystal planes compared with previously measured results by Weldon et al. [2].

5.6 Energy Resolution

5.6.1 Energy Resolution of the Stilbene Pillars

Energy resolution is typically defined as

$$\text{Res.}(\%) = \frac{\text{FWHM}}{E_0} * 100, \tag{5.4}$$

where FWHM is the full-width at half maximum of a photopeak at energy E_0. It is unlikely, however, for photons of several hundred keV to undergo photoelectric absorption in stilbene. One method used to determine the energy resolution of organic scintillators is a Compton back-scatter experiment or Compton-coincidence technique [96]. The technique involves placing a mono-energetic gamma-ray source, such as ^{137}Cs in between an organic and inorganic scintillator. A gamma ray that scatters 180^o in the organic scintillator can be photoelectrically absorbed in the inorganic scintillator. These two events can be correlated both in time and energy since the energy of the gamma ray emitted by the source is known. Figure 5.14 shows the experimental setup used to measure the energy resolution of the stilbene pillars within the H2DPI.

Gating on coincident events between the H2DPI and the inorganic scintillator where a 186 keV event was recorded in the inorganic scintillator produced the distribution shown in Figure 5.15.

The Compton edge peak acquired from each stilbene pillar was calibrated and fit with a Gaussian distribution. It was found that the average energy resolution for the stilbene pillars at 477 keV was 11.24 $\pm$ 0.47 %.

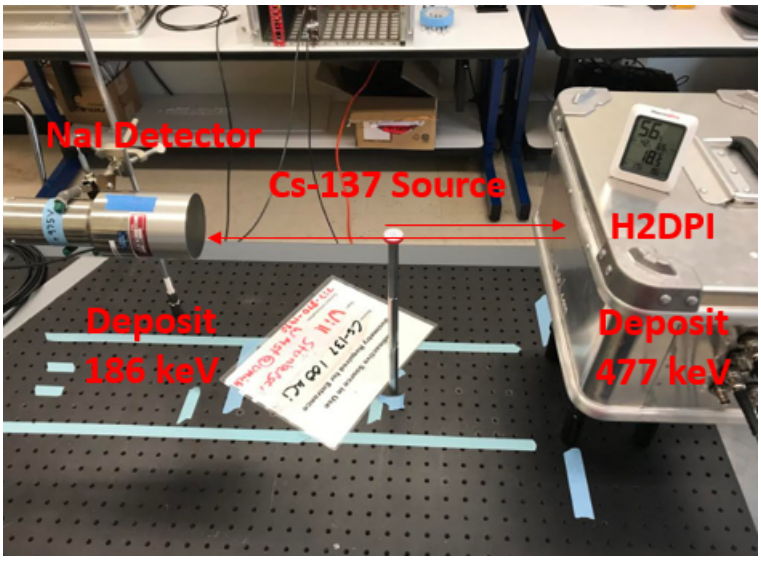

Figure 5.14: Photograph of the experimental setup for the Compton back-scatter experiment with the H2DPI.

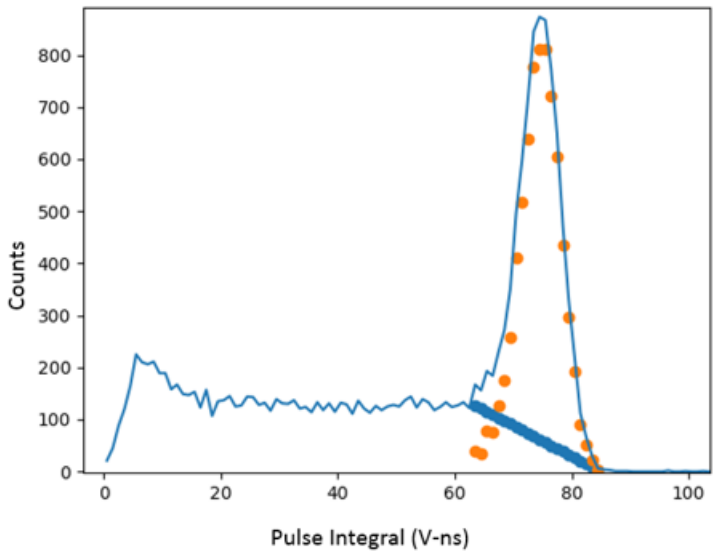

Figure 5.15: Coincident pulse integral spectrum for the first pillar of stilbene in the prototype H2DPI shown as a blue line. The blue scatter distribution shows the linear interpolation used to extract the Compton edge peak shown as an orange scatter distribution.

5.6.2 Energy Resolution of the $CeBr_3$ Cylinders

Energy resolution for the $CeBr_3$ Cylinders was much simpler to obtain than for the stilbene pillars. Equation 5.4 was used to determine the energy resolution of the

$CeBr_3$ Cylinders for the photopeaks produced by ^{137}Cs and ^{22}Na. It was found that the average energy resolution for the $CeBr_3$ Cylinders in the system was 4.35 ± 0.31 %.

5.7 Z-Position Calibration of the Stilbene Pillars

Using a dual-readout system allows for the reconstruction of the interaction location by comparing the relative light output between the top and bottom SiPMs:

$$\text{Ratio} = \frac{\text{Pulse Integral}_1}{\text{Pulse Integral}_1 + \text{Pulse Integral}_2}. \tag{5.5}$$

In Equation 5.5, Pulse Integral_1 is the pulse integral from the bottom SiPM and Pulse Integral_2 is the pulse integral from the top SiPM. To accurately reconstruct the interaction positions, a calibration measurement was performed where a ^{137}Cs and ^{22}Na were collimated to make a 1-mm fan beam using lead bricks. A diagram of the experimental set up is shown in Figure 5.16. This fan beam was placed at discrete points in 5 mm increments across the pillars to calibrate the position resolution. Figure 5.17 shows the average ratio for the twelve stilbene pillars as a function of calibration position along the stilbene pillars.

Figure 5.17 shows that the response is uniform between the stilbene pillars. It was also found that the average ratio was not dependant on the light output. The uncertainty in the reconstructed position, however, is strongly dependant on both the positions of reconstruction and the light output. Figure 5.18 shows the average uncertainty in the reconstruction position between the stilbene pillars for light output values between 25 and 50 keVee. Events toward the center of the pillar have lower position uncertainty while events towards the ends of the pillars have significantly higher position uncertainty. Position uncertainty is also light output dependent. Figure 5.19 shows how the uncertainty in position reconstruction decreases as the light

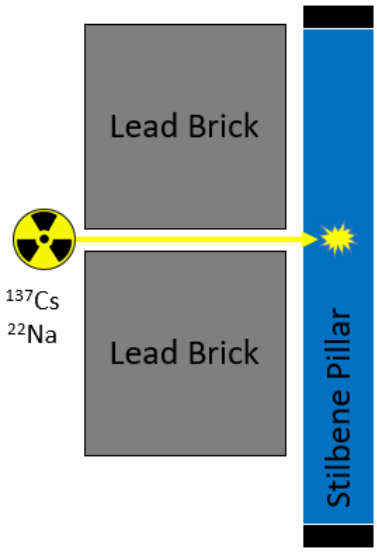

Figure 5.16: Diagram showing how the position calibration was performed along the stilbene pillars in the H2DPI.

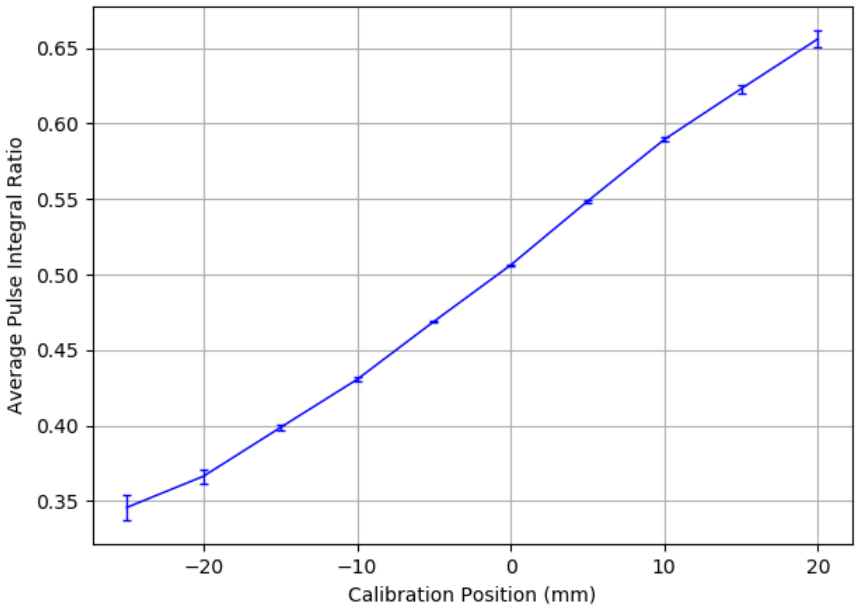

Figure 5.17: Average pulse integral ratio between the twelve stilbene pillars as a function of calibration position. Error bars are a single standard deviation of the average values.

output increases.

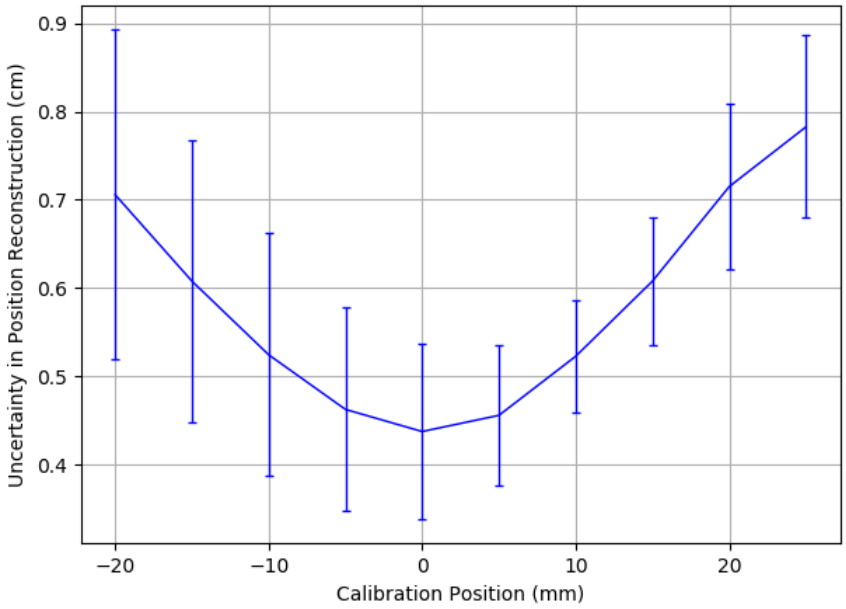

Figure 5.18: Average uncertainty in the reconstructed position for events between 25 to 50 keVee for the twelve stilbene pillars as a function of interaction location across the stilbene pillar. Error bars are a single standard deviation of the average values.

5.8 Conclusion

The above chapter demonstrates the complexity of calibrating the H2DPI. This level of detail in characterizing and understanding the system response is necessary for accurate source reconstruction and modeling the system. While time consuming and tedious, the results shown in Chapter VI will demonstrate how powerful a tool an imaging system can be.

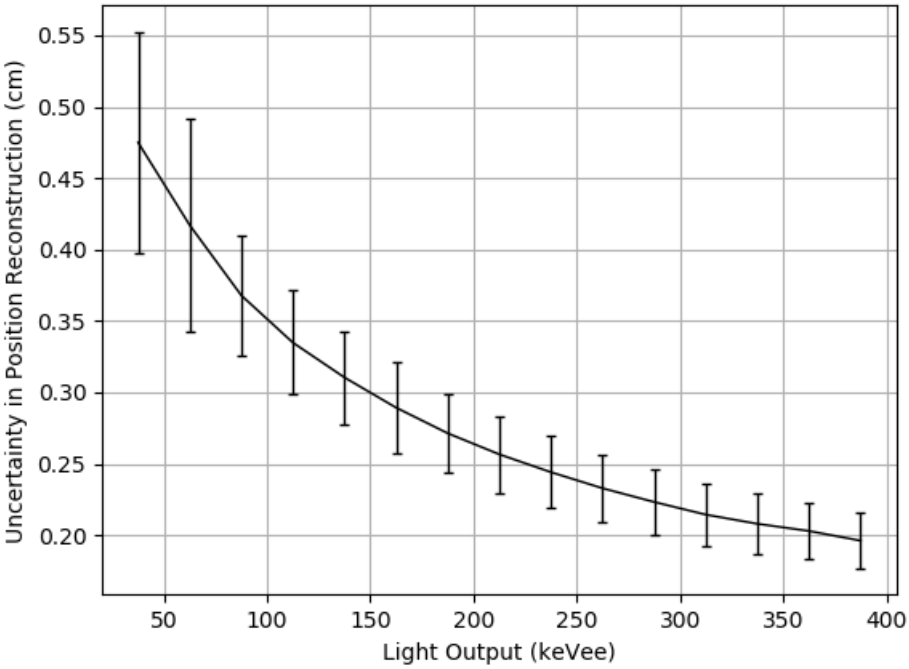

Figure 5.19: Average uncertainty in the reconstructed position for events at the center of the pillars as a function of light output. Error bars are a single standard deviation of the average values for all twelve stilbene pillars.

CHAPTER VI

Imaging and Characterizing Radioactive Sources

The characterization detailed in Chapter V was used to reconstruct both neutron and gamma-ray emitting sources. This chapter demonstrates the imaging capabilities of the H2DPI. Specifically, Section 6.1 addresses the impact of the anisotropic response of stilbene on the H2DPI. Section 6.2 validates the neutron image resolution of the system, demonstrates isolation of multiple neutron sources in the same field of view and demonstrates identification of neutron source by neutron spectroscopy. Section 6.3 then shows the gamma-ray imaging capability of the H2DPI by comparing the image quality of the 16-pillar prototype with the 8-pillar prototype, localizing a gamma-ray source in the presence of neutron sources, and localizing and identifying two SNM objects in the same field of view.

6.1 Impact of the Anisotropic Response of Stilbene on Neutron Imaging

The following analysis seeks to quantify the impact of the directionally-dependent stilbene response for imaging neutron sources in 4π, and determine if direction compensation is required to accurately image sources. This analysis is especially relevant because there has been a significant effort to develop organic scintillator-based compact NSCs for nuclear security applications [44, 45, 46, 47, 49].

6.1.1 Testing Methodology

To characterize the potential impact of the various light-output functions on the H2DPI detailed in Section 5.5, measurements were performed with a ^{252}Cf source at the following three locations: 50.8 cm at the angular position of (0^o,-0.8^o) for 23.0 hours, 50.8 cm at the angular position of (-90^o,-0.8^o) for 23.5 hours, and 56.48 cm at the angular position of (0^o,90^o) for 22.1 hours. ^{137}Cs calibration measurements were performed before and after the measurements to account for gain change. An average gain change of $3.97 \pm 1.08\%$ occurred over the course of each measurement. The gain of SiPMs decreases as temperature increases and temperature of the system increases during operation. Not accounting for gain change over the course of the measurements would cause events above a defined threshold to not be counted, incorrectly decreasing the efficiency of the detector. While gain change will not significantly impact the imaging results, it is necessary to take it into account so that it cannot be a potential explanation for a measured result. 54097, 33457, and 22893 cone projections were recorded for each measurement, respectively. Cone projections for this analysis are defined as neutron double-scatter events that meet the following threshold requirements: a time-difference value between 217-8825 ps, a light-output value between 50-1500 keVee, and each interaction has a pulse shape that is classified as a neutron interaction. Cone projections for each data set were generated using the appropriate light-output curves and the incorrect light-output curves to determine if there is significant variance in image characteristics as a function of light-output curve. The idea being that a neutron source could be in any given location relative to the prototype H2DPI, and the directionality of a given neutron event is not immediately knowable. For ease of application to the system, a single light-output curve would be applied to reconstruct the neutron energy deposition. This analysis seeks to determine if the incorrect light-output curve is applied, does that significantly impact the accuracy of imaging neutron sources in 4π.

The prototype used for this analysis is shown in Figure 6.1 where the axes of the stilbene pillars are labeled. By appropriate light-output curves, we are referring to the curves corresponding to the orientation of the crystals for a given direction in the H2DPI. As an example, for the measurement with the ^{252}Cf source at (0^o,-0.8^o), the $L_{c'}$ light-output curve would be applied to the top left pillar while the L_a light-output curve would be applied to the top right pillar. Each generated data set was analyzed using a bootstrapping technique: a random cone was sampled from the data set 1000 times and the following 2000 cones after that randomly sampled cone were analyzed to generate an image. The data were also analyzed by randomly sampling 2000 cone projections from the entirety of each data set. Randomly sampling from the data set did not have a significant impact on the presented parameters. Choosing 2000 consecutive cone projections was done to emulate the result from a single continuous measurement. 15 iterations of LM-MLEM, as described in Section 2.2, were then applied to generate the image for the measurements at (0^o,-0.8^o) and (-90^o,-0.8^o), while 10 iterations were applied to the images from the measurement at (0^o,90^o). Convergence criteria were not assessed in this analysis and iteration values were chosen based on visual inspection. The most likely pixel location and the FWHM in both the altitude and azimuthal directions were recorded for each image. The FWHM in the azimuthal direction was not analyzed for the measurement with the source at (0^o,90^o).

6.1.2 Results

Tables 6.1-6.3 contain the results of the analysis detailed in Section 6.1.1. Table 6.3 does not contain an appropriate light-output curve value because all the stilbene crystals were aligned along the L_b plane for the measurement. In addition, the average highest azimuthal pixel value in Table 6.3 is not reported because it ranged across the entire azimuthal space. The azimuthal FWHM is also not reported in Table 6.3

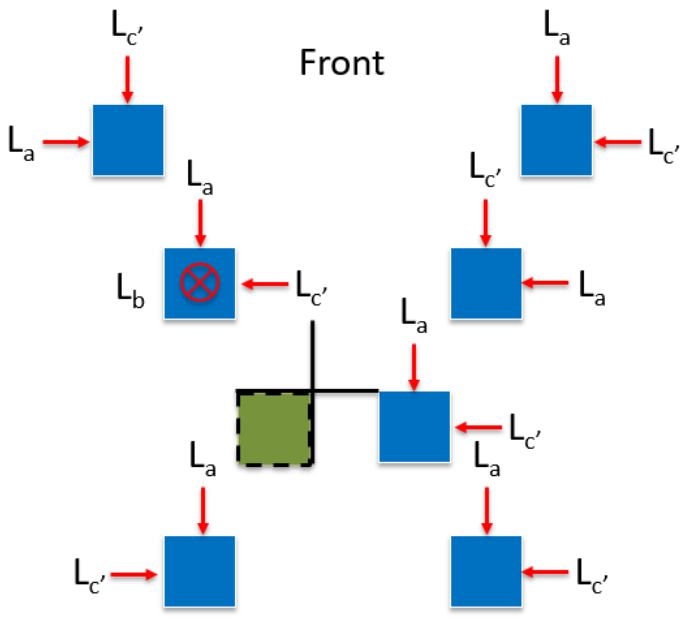

Figure 6.1: Layout of an 8-pillar iteration of the H2DPI depicting the crystal orientation of the stilbene pillars (blue squares). The L_b crystal plane is both going into and coming out of the page for all of the stilbene pillars. The green square with the dashed outline is a LYSO(Ce) pillar.

because analyzing the azimuthal slice along the highest pixel value did not always reach a half-maximum value, hence not returning a value for the FWHM. The altitude FWHM contained in Table 6.3 is also much larger and has greater variance than the values contained in Tables 6.1 and 6.2. The difference occurs because the altitude FWHM reported was measured across the image using the altitude distribution for the highest azimuthal pixel location and the altitude distribution 180^o apart. For example, if the highest pixel location was at -140^o in the azimuthal, the altitude values from -140^o and 40^o would be combined to produce one continuous altitude distribution. The half maximum point was determined for each one of these altitude sides. Due to how the projections are being reconstructed, the peak tends to be around 80^o. This offset from 90^o substantially increases the FWHM relative to the other two source locations since the two "peaks" will be separated by a minimum of around 20^o. This feature of the reconstruction explains why the FWHM for the 90^o

source location is much larger and has greater variance than the other two locations. All uncertainties listed in the tables are a single standard deviation for the image characteristics from the 1000 bootstrapped images.

Table 6.1: Imaging characteristics of a ^{252}Cf source 50.8 cm from the center of the H2DPI and at angular position (0^o,-0.8^o) for varying light-output curves.

Light Output Curve	Azimuthal Position (Degrees)	Altitude Position (Degrees)	Azimuthal FWHM (Degrees)	Altitude FWHM (Degrees)
Appropriate	-0.74 ± 0.90	-2.29 ± 2.86	11.45 ± 1.17	22.58 ± 4.39
L_a	-2.59 ± 1.06	-2.61 ± 3.15	11.53 ± 1.40	22.83 ± 4.69
L_b	-2.42 ± 1.01	-2.65 ± 2.76	11.44 ± 1.34	22.46 ± 4.86
$L_{c'}$	-1.47 ± 0.88	-2.80 ± 2.55	11.70 ± 1.30	23.10 ± 4.46

Table 6.2: Imaging characteristics of a ^{252}Cf source 50.8 cm from the center of the H2DPI and at angular position (-90^o,-0.8^o) for varying light-output curves.

Light Output Curve	Azimuthal Position (Degrees)	Altitude Position (Degrees)	Azimuthal FWHM (Degrees)	Altitude FWHM (Degrees)
Appropriate	-87.98 ± 1.20	-1.74 ± 3.45	13.27 ± 2.19	24.91 ± 4.33
L_a	-88.64 ± 1.30	-1.16 ± 2.95	13.10 ± 2.55	25.11 ± 5.20
L_b	-88.90 ± 1.22	-1.22 ± 2.96	12.95 ± 2.45	24.07 ± 4.86
$L_{c'}$	-90.01 ± 1.31	-2.00 ± 2.89	12.99 ± 1.94	23.03 ± 3.96

Table 6.3: Imaging characteristics of a ^{252}Cf source 56.48 cm from the center of the H2DPI and at angular position (0^o,90^o) for varying light-output curves.

Light Output Curve	Altitude Position (Degrees)	Altitude FWHM (Degrees)
L_a	82.94 ± 5.41	69.43 ± 35.40
L_b (Appropriate)	82.03 ± 8.37	68.62 ± 35.14
$L_{c'}$	82.55 ± 1.81	58.15 ± 32.55

Figures 6.2-6.4 are reconstructed images of the ^{252}Cf source in the three angular locations to visualize the images that are being analyzed. Each image is composed of 2000 cone projections where the cone projections were generated using the appropriate light-output curves. Each image accurately identifies the source location.

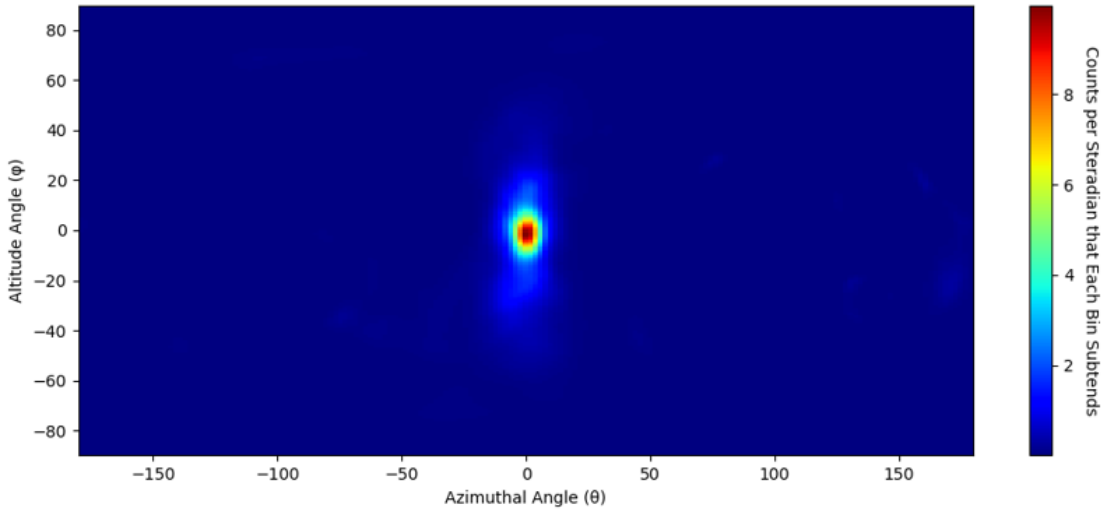

Figure 6.2: Neutron image of a ^{252}Cf source 50.8 cm from the center of the H2DPI at an angular position of (0^o,-0.8^o). (2000 cones with 15 iterations of LM-MLEM applied to the image).

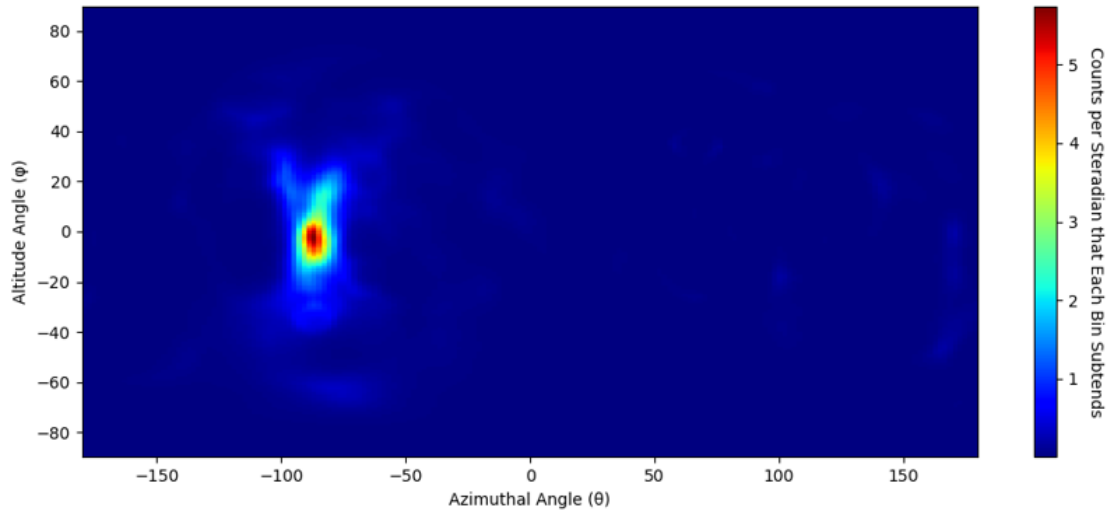

Figure 6.3: Neutron image of a ^{252}Cf source 50.8 cm from the center of the H2DPI at an angular position of (-90^o,-0.8^o). (2000 cones with 15 iterations of LM-MLEM applied to the image.)

6.1.3 Conclusions

The purpose of this analysis was to determine if direction-dependent compensation is necessary when imaging sources using a stilbene-based NSC, due to the anisotropic

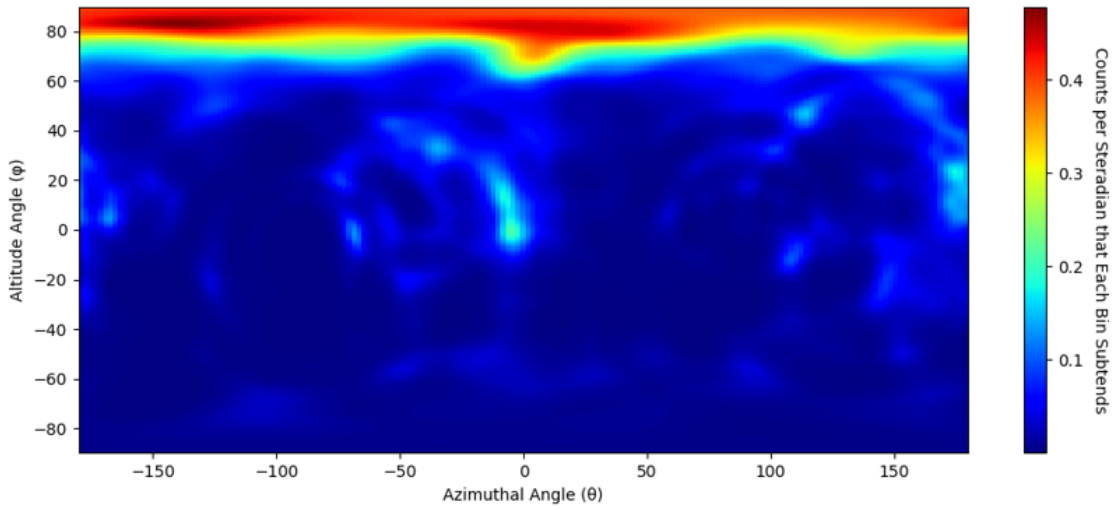

Figure 6.4: Neutron image of a ^{252}Cf source 56.48 cm from the center of the H2DPI at an angular position of (0^o,90^o). (2000 cones with 10 iterations of LM-MLEM applied to the image.)

response of stilbene crystals. Accordingly, the light-output curves for neutrons incident along the three crystal planes were measured and then applied appropriately and incorrectly to image sources in three angular locations: (0^o,-0.8^o), (-90^o,-0.8^o) and (0^o,90^o). Image characteristics of generated images were then recorded and analyzed to see if neutron sources can be accurately imaged when applying the incorrect light-output curve. Figure 6.5 compares the position information in Tables 6.1-6.3. The maximum difference in the average azimuthal pixel location for the source location at (0^o,-0.8^o) was found to be 1.85 ± 1.39^o and 2.03 ± 1.78^o for the source location at (-90^o,-0.8^o) when varying between the appropriate light-output curves and using incorrect light-output curves. The average azimuthal position for the appropriate light-output curves was also found to be 1.68 standard deviations from the actual source location for the source at (-90^o,-0.8^o) while all other reconstructions using incorrect light output curves had the average azimuthal pixel location within a single standard deviation for that location. Altitude locations were within a single standard deviation of the true source location for all reconstructions with the exception of the

source location at (0^o,90^o), where only the true light output curves reconstructed the source location within a single standard deviation.

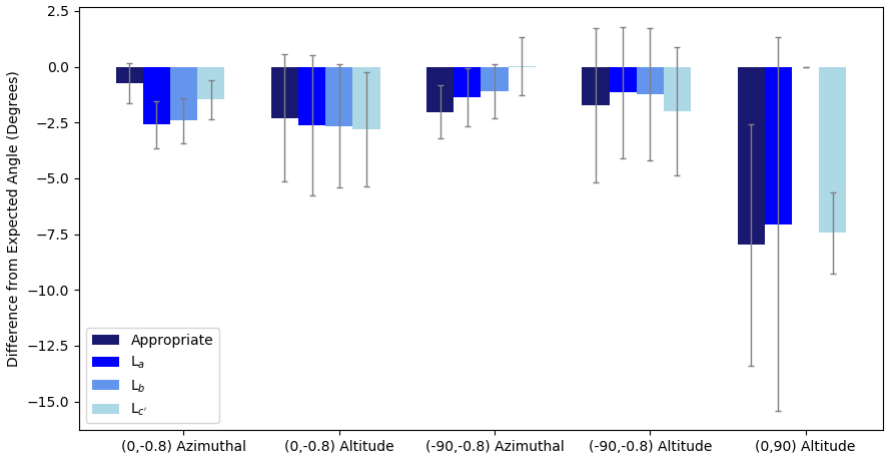

Figure 6.5: Comparison of the position information in Tables 6.1-6.3.

These results show a minimal impact on the ability of the H2DPI to image neutron sources in 4π when using the appropriate or incorrect light-output curves. The reason behind this result is most likely due to the broadening in cone projections. Figure 6.6 shows the relative uncertainty for the energy deposition of incident neutrons in the first interaction (E_0), relative uncertainty for the neutron after the first interaction (E_{TOF}), and relative uncertainty for the reconstructed neutron energy (E), which is the summation of E_0 and E_{TOF}. Relative uncertainty in this analysis is defined as the standard deviation, σ, of the value divided by the value itself. Mathematically, relative uncertainty can be expressed for a variable, x, by

$$\text{Relative Uncertainty } (\%) = \frac{\sigma_x}{x} \times 100. \tag{6.1}$$

The uncertainty in E_{TOF} is based on the position uncertainty and time resolution of the system, 217 ps standard deviation. The uncertainty in E_0 is based on the energy resolution of the stilbene pillars, which was found to be 11.2±0.5 % at 478 keVee. As shown in Figure 6.6, the relative uncertainty in E_{TOF} extends upwards of 200 %

due to the uncertainty in the path length and time resolution, while the uncertainty in the initial interaction tends to be less than 15 %. Cone projection uncertainty in the H2DPI is thus dominated by the TOF reconstruction energy because the H2DPI is such a compact system. Even if the incorrect light-output curves are used, this change is not significant enough to alter image characteristics due to domination of uncertainty in the TOF reconstruction energy. If the uncertainty in the TOF reconstruction was comparable to the uncertainty in the initial energy deposition in the first interaction or the anisotropic response of stilbene were much greater in magnitude, we would expect the anisotropic response to have an impact on the image reconstruction.

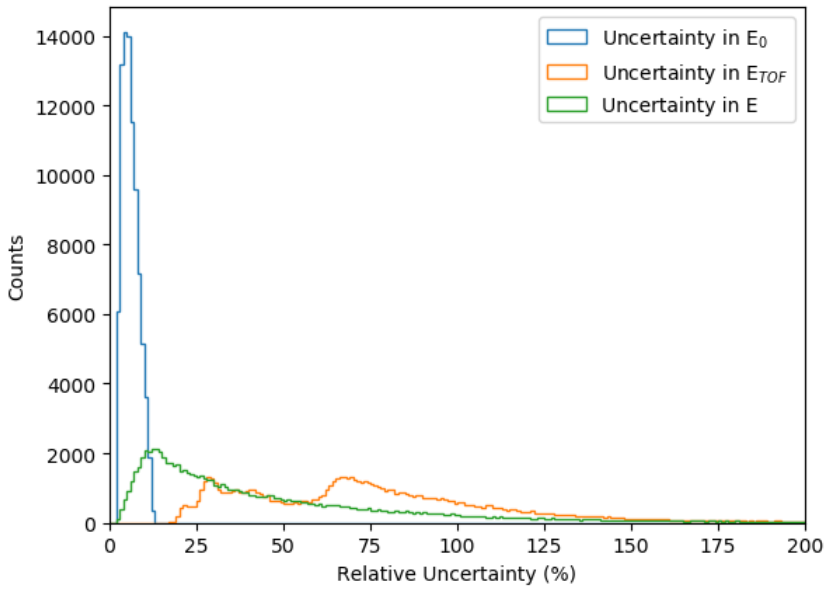

Figure 6.6: Histogram of relative uncertainties for the initial energy deposition (E_0), TOF energy (E_{TOF}), and the reconstructed incident energy (E).

6.2 Neutron Imaging

6.2.1 Neutron Image Resolution

Determining if a source is present and localizing said source is particularly useful for an emergency response or search scenario while accurate characterization of a source can be better applied to a safeguards or verification scenario. The following analysis characterizes the neutron image resolution of the 16-pillar prototype H2DPI to determine when multiple neutron point sources can be identified in the same field of view for application in a safeguards scenario.

6.2.1.1 Experimental Methodology

A measurement setup was built to measure a ^{252}Cf source in 2.5 degree increments along the azimuthal plane in front of the H2DPI at a constant radius of 58.42 cm. This system was made to perform precise measurements to determine the image resolution of the prototype 16-pillar H2DPI. Image resolution for this analysis is being defined as the degree separation required to identify two point sources. Figure 6.7 shows the measurement setup where the prototype H2DPI is in the aluminum box towards the front of the image. The ^{252}Cf source was measured in 5 degree increments from 0 degrees to 25 degrees. The ^{252}Cf source was measured for two hours in each source location. ^{137}Cs calibration measurements were taken before and after each measurement to account for gain change over the course of the measurement. The data sets were then summed together to determine when the H2DPI can resolve multiple ^{252}Cf sources in the same field of view. Figure 6.8 shows the primary result from this series of measurements. LM-MLEM was applied to each data set and iterated 20 times. Convergence criteria was not applied.

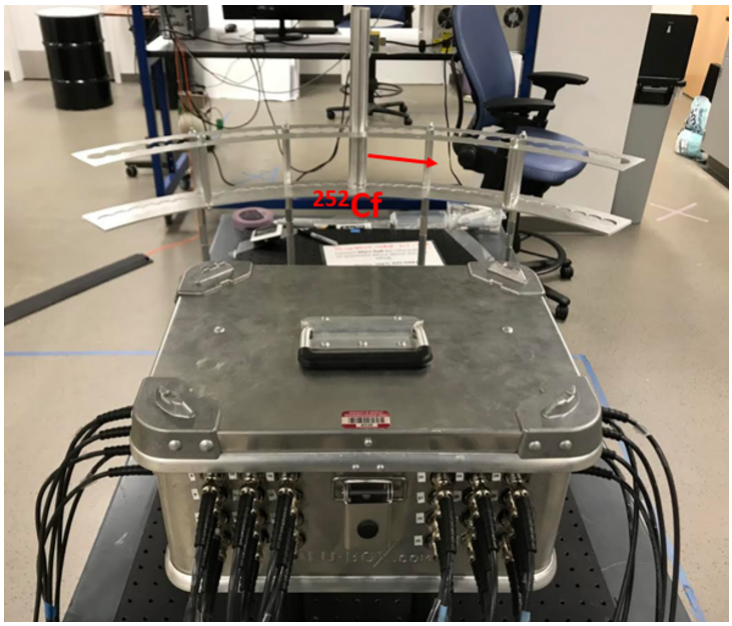

Figure 6.7: Photograph for the experimental setup used to measure the neutron-image resolution of the H2DPI.

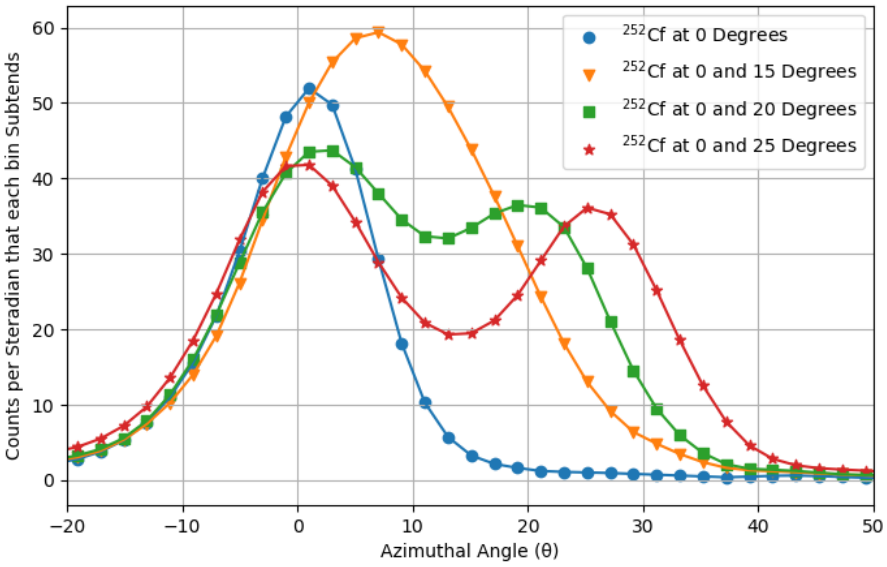

Figure 6.8: Azimuthal slice of the reconstructed neutron images with 20 iterations of LM-MLEM applied to the data sets.

6.2.1.2 Experimental Results and Conclusions

Figure 6.8 shows that the prototype H2DPI can begin to differentiate neutron sources with a Watt spectrum of approximately equal intensity at an azimuthal sep-

aration of 20 degrees. The 15 degree separation measurement shown in Figure 6.8 has a larger spread than would be expected from a single point source, but it cannot be differentiated from multiple sources or potentially an extended source. The single ^{252}Cf source measurement is shown in Figure 6.8 for reference.

Figure 6.9 further breaks down the 20 degree separation measurement shown in Figure 6.8. The result shown in Figure 6.8 was produced using cone projections with less than 50% relative uncertainty in the reconstructed neutron energy where relative uncertainty is defined as

$$\text{Relative Uncertainty } (\%) = \frac{\sigma_{(E_{\text{TOF}}+E_0)}}{E_{\text{TOF}} + E_0} \times 100. \tag{6.2}$$

Figure 6.9 compares the azimuthal slices if all events with up to 100% relative uncertainty are projected with the initial result. The defined two peaks begin to blur out with the higher uncertainty events being added into the analysis. This result shows that the image resolution of the H2DPI can be improved by omitting events with a higher relative uncertainty. The cost of this improved image resolution is then the efficiency of the system. Even with the higher uncertainty events in the projection, the distribution can still be differentiated from a point source.

The azimuthal efficiency of the prototype H2DPI is not constant. Moving the source from 0 degrees to 20 degrees decreases the intrinsic neutron double-scatter efficiency of the system from 0.0558% to 0.0495%. To assess if the image resolution is significantly impacted by this variable efficiency, the number of cone projections making up each source location were made equal for events with less than 100% relative uncertainty with the 20 degree separation measurement. The result from this analysis is shown as the green-square curve in Figure 6.9. Comparing this new result with the orange-triangle curve shows that there is only a decrease in likelihood for a neutron originating from the source location at 0 degrees. This result makes sense

since this is only decreasing the number of cone projections making up that location, making it less likely that a neutron would originate from that location. The shape for the source at 20 degrees is not changed by the reduction in the number of cone projections from the source at 0 degrees.

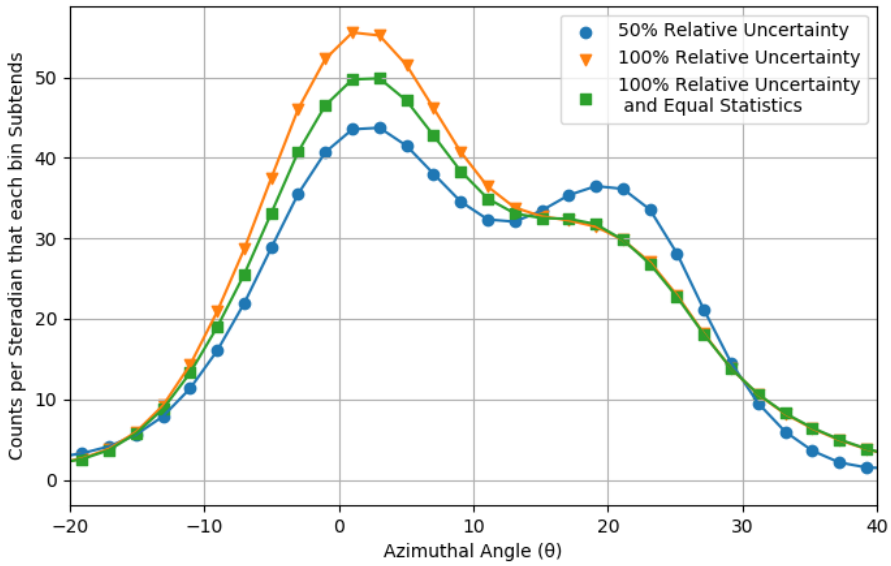

Figure 6.9: Comparison of the azimuthal slices for two relative uncertainty upper limits and equal number of cone projections for the combined data sets of the ^{252}Cf source at 0° and 20° .

6.2.2 Imaging Multiple Neutron Sources in the Same Field of View

Section 6.2.1 detailed results showing that the H2DPI is capable of resolving multiple neutron sources in the same field of view when the sources are separated by twenty degrees or more. To further test this result and the spectroscopy capabilities of the prototype H2DPI, a measurement was taken with two 100-μCi ^{137}Cs source, 6×10^6 n/s ^{252}Cf source and 1×10^6 n/s PuBe source in the same field of view.

6.2.2.1 Experimental Set Up

The ^{137}Cs sources were placed at 90 degrees and a radius of 20.32 cm. The ^{252}Cf source was placed at 15 degrees and a radius of 58.42 cm. The PuBe source was

placed at -35 degrees and a radius of 31.01 cm. All sources were centered in the altitude direction relative the to H2DPI. The sources were measured together for one hour with calibration measurements being taken before and after the measurement. In addition, each source was independently measured at each location for one hour. Figure 6.10 shows a photograph of the measurement setup. The reconstruction of the ^{137}Cs sources will be discussed in Section 6.3.

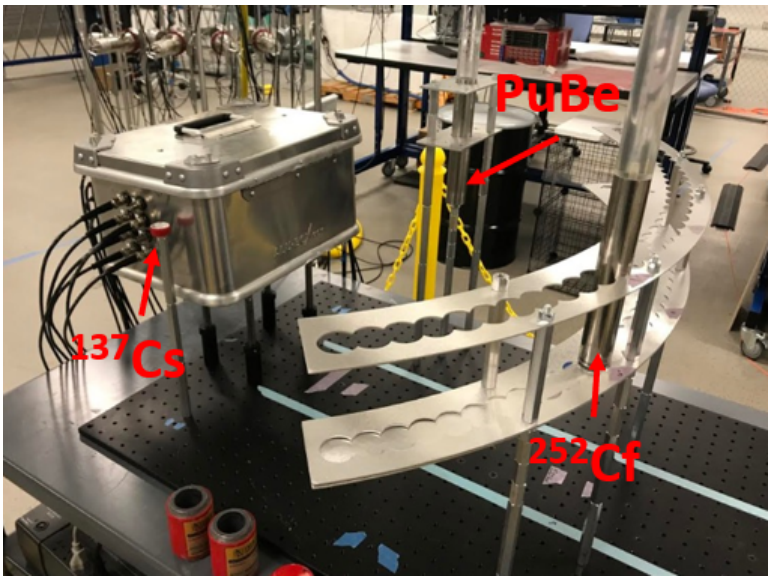

Figure 6.10: Photograph the experimental setup used to measure two 100 μCi ^{137}Cs sources, a 6×10^6 n/s ^{252}Cf source, and a 1×10^6 n/s PuBe source in the same field of view.

6.2.2.2 Neutron Imaging Results

Neutron interactions from the measurement shown in Figure 6.10 were reconstructed using the same methodology discussed in Section 2.2 and the following threshold requirements: a time-difference value between 217-8825 ps, a light-output value between 50-1500 keVee, and each interaction has a pulse shape that is classified as a neutron interaction. In addition, a physical event is required where the neutron TOF energy must be within a single standard deviation of the reconstructed energy deposition in the second interaction. Projecting the neutron double-scatter events

that meet these requirements from the measurement yields Figure 6.11.

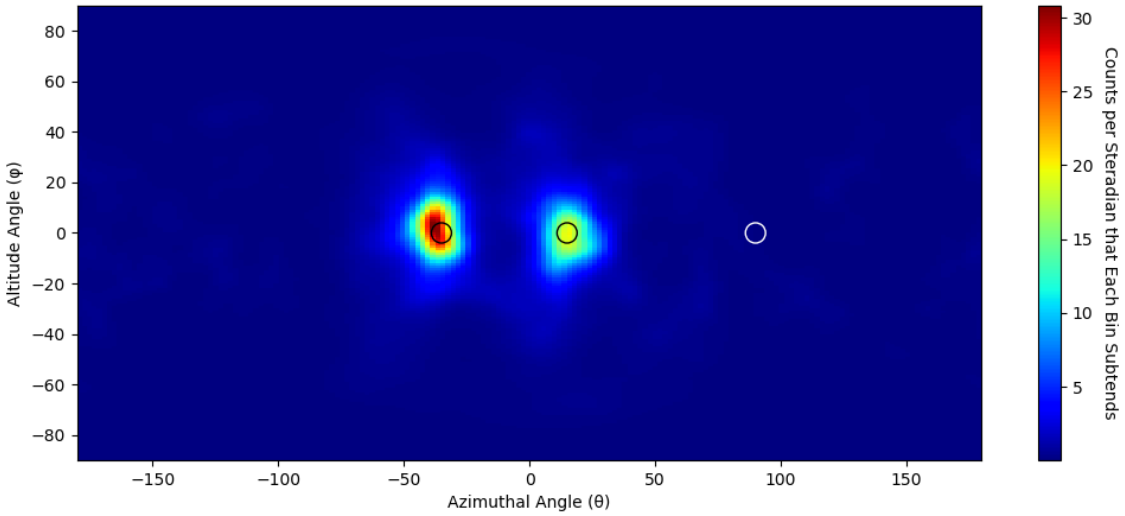

Figure 6.11: Neutron image of the ^{252}Cf and Pube sources (black circles) reconstructed from neutron events with less than 100% relative uncertainty with 20 iterations of LM-MLEM applied to the data set. The location of the ^{137}Cs source is shown as a white circles.

6.2.2.3 Neutron Spectroscopy

As discussed in Section 2.2, NSCs measure the incident energy of neutrons making them neutron spectrometers. Neutron spectra extraction can be performed on SBP images by analyzing the individual cone projections. Figure 6.12 shows the neutron SBP image from the measurement shown in Figure 6.11. The two regions shown in Figure 6.12 cover the two source locations. The centers of each location are (-35,0) and (15,0). Each region is ±20 degrees in the altitude direction and ±25 degrees in the azimuthal direction from the two defined points. Figure 6.13 shows the extracted neutron energy spectra from the two regions.

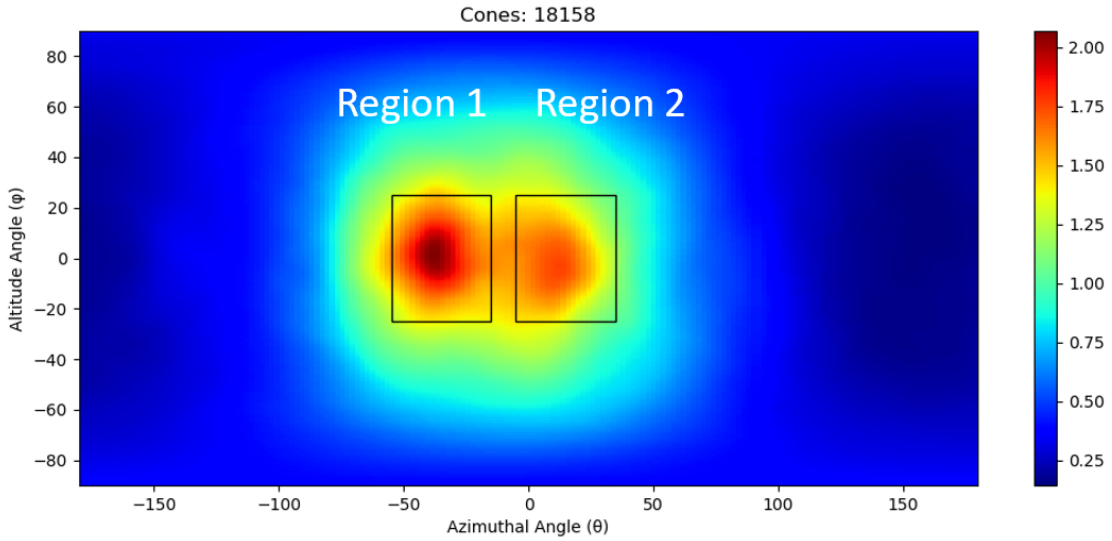

Figure 6.12: SBP image of the ^{252}Cf and Pube sources reconstructed from neutron events with less than 100% relative uncertainty. Two regions are defined around the sources to shown as black boxes used to extract the neutron energy spectra from each source.

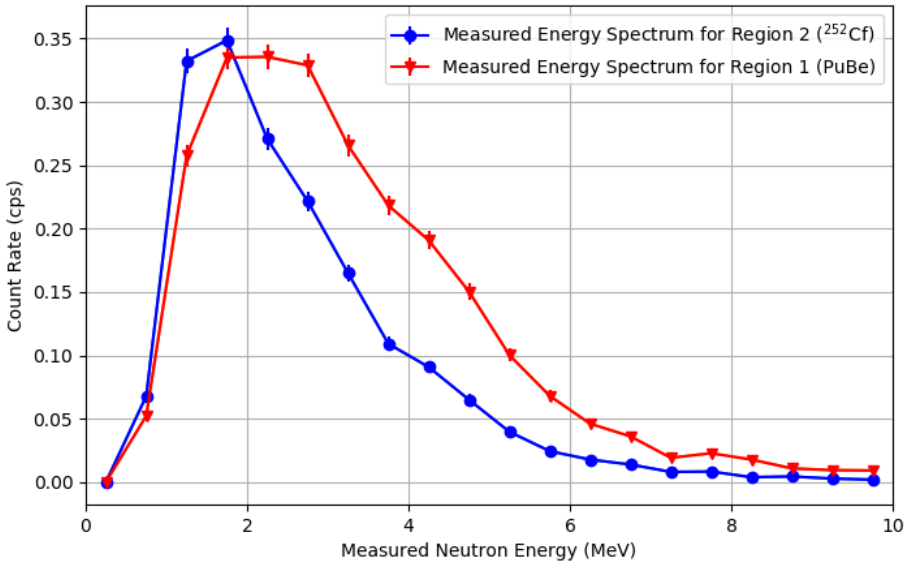

Figure 6.13: Measured neutron energy spectra from the SBP image shown in Figure 6.12.

6.2.2.4 Neutron Spectroscopy Analysis

Taking the average of each of the extracted neutron energy spectra shown in Figure 6.13 yields an average neutron energy of 2.63 MeV for the ^{252}Cf source and 3.22 MeV for the PuBe source. A higher average neutron energy value from the PuBe source is expected since the (α, n) spectrum from PuBe emits more higher energy neutrons relative to the Watt spectrum from ^{252}Cf [57]. The extracted energy spectra were further analyzed to better understand their shapes and assess repeatability of the measurement. As stated, the sources were independently measured for one hour. The same spectrum extraction technique was applied when only one source was present to determine the contribution from the expected source and the contribution or "contamination" from the adjacent source. Figures 6.14 and 6.15 show this breakdown. Analyzing Figure 6.14, the orange-square curve is the contamination from the PuBe source in the defined region where the ^{252}Cf source would be present. The green-diamond curve is the contribution from the lone ^{252}Cf source. The ^{252}Cf source yields the majority of interactions from that source location. The opposite

holds true for the PuBe spectrum result shown in Figure 6.15. Summing the two curves from the true source and the contamination from the other source produces the red-triangle curve shown in both figures. This summed curve is within one to two standard deviations of the extracted neutron energy spectra from Figure 6.13, showing that the spectra are being accurately extracted. The uncertainty bars are a single standard deviation in the uncertainty making up the count rate assuming Poisson statistics.

The sources for this measurement were separated by 40 degrees, approximately double the neutron image resolution of the system. We would expect if the sources were measured in a closer configuration that the contribution from the other source would begin to significantly impact the measured spectrum such that the two spectra would just average and not yield distinctly different distributions. Adding the (α, n) spectrum to the Watt spectrum, assuming a significant (α, n) source, would still increase the average measured neutron energy and allow the system to differentiate the source distribution from a pure Watt spectrum.

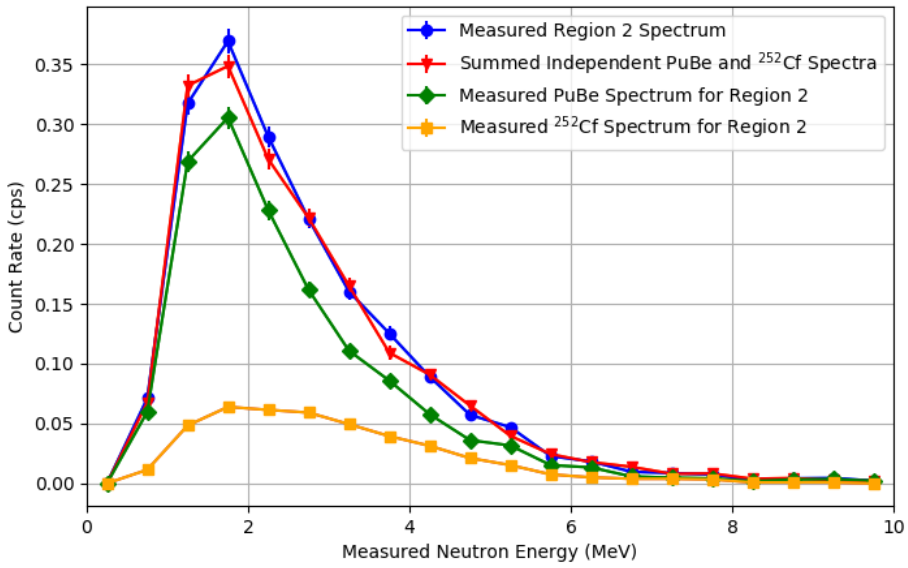

Figure 6.14: Breakdown of the measured neutron energy spectrum from the region containing the ^{252}Cf source.

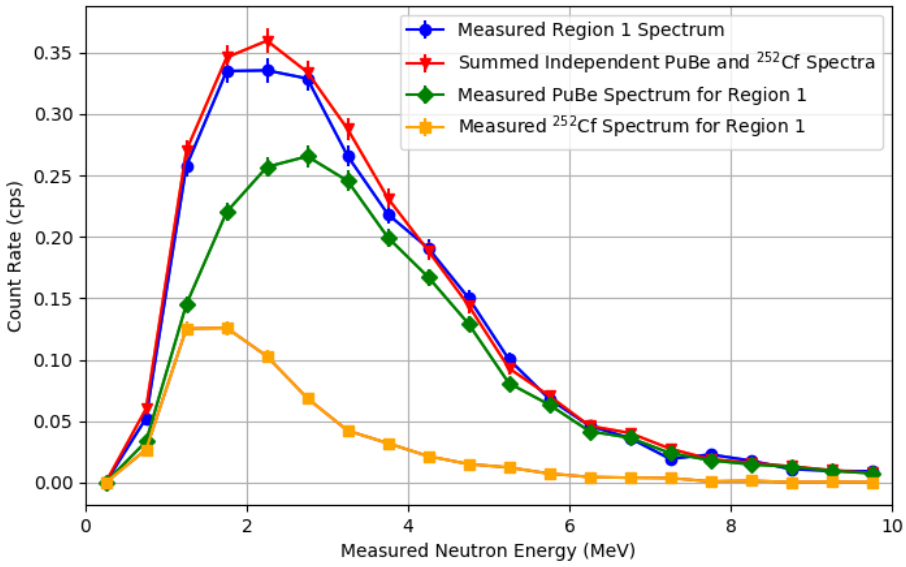

Figure 6.15: Breakdown of the measured neutron energy spectrum from the region containing the PuBe source.

6.2.3 Neutron Imaging Conclusions

Scatter-based neutron imaging enables source localization and spectroscopic identification of fast neutron emitting sources. Detection and localization of fast-neutron sources is of particular interest to search and verification scenarios since neutrons do not make up a substantial portion of background radiation and generally are due to the presence of a man-made source. The results presented demonstrate the localization and spectroscopic capabilities of a compact dual-particle imager. While uncertainties associated with the TOF of the neutrons dominate the response of the H2DPI due to the short flight paths, the H2DPI still has sufficient resolution to differentiate a Watt spectrum from an (α, n) source. The results presented are the first demonstrations of spectra extraction and multiple neutron source localization using a compact scatter-based imaging system.

6.3 Gamma-Ray Imaging using the 16-Pillar H2DPI

6.3.1 Comparing Compton Imaging Techniques

The 8-pillar prototype H2DPI was capable of imaging gamma-ray sources as demonstrated in Section 2.4 with the drawback of needing a significant number of cone projections to accurately localize a gamma-ray source. In addition to this drawback, the technique did not resolve multiple sources and generally produced significant artifacts in the images. Figures 6.16 - 6.18 demonstrate the improvement in localization capability between the two methods. The source location for each image is shown as a white circle.

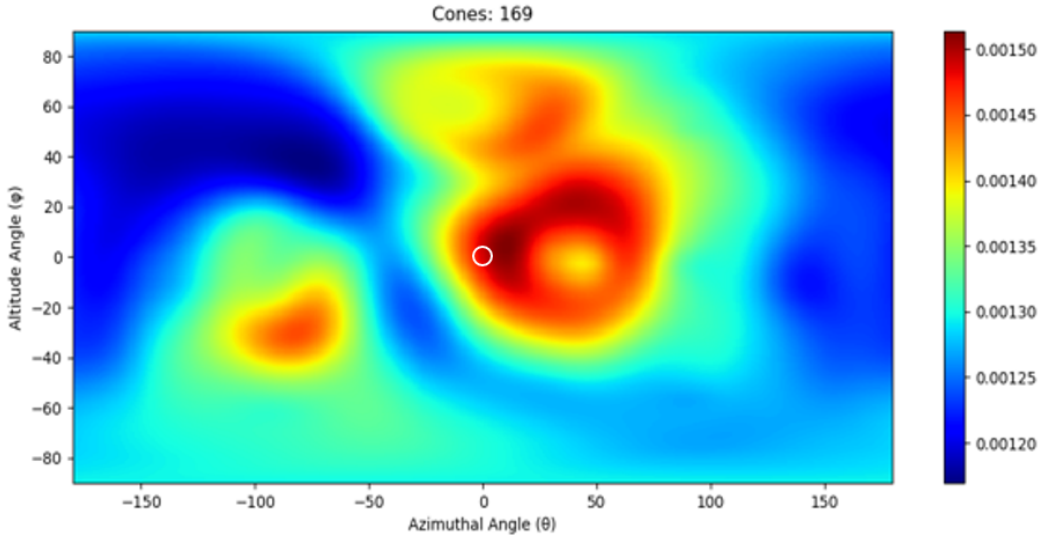

Figure 6.16: SBP image of a ^{137}Cs source using the Compton imaging method with the 8-pillar H2DPI.

Figures 6.16 and 6.17 show SBP images of a ^{137}Cs source where both images are composed of an equal number of cone projections, 169. These 169 cone projections were acquired in one minute for the 16-pillar H2DPI and 1.8 minutes for the 8-pillar H2DPI. While the 8-pillar H2DPI is not limited to where the second scattering interaction can occur, poor reconstruction and the cuts necessary to image gamma rays make the system less efficient than the 16-pillar iteration. The ^{137}Cs source is

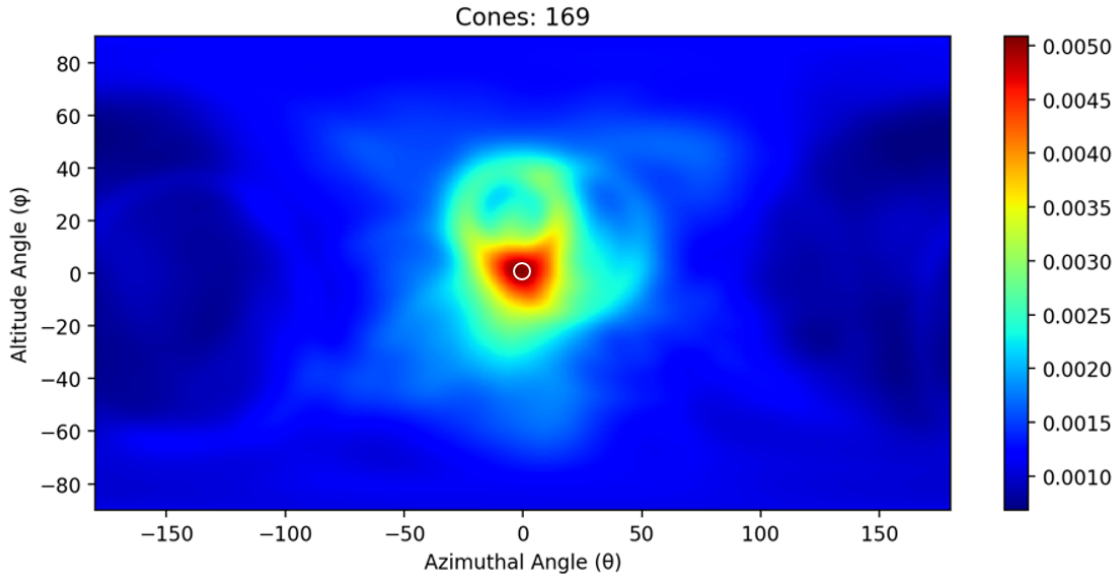

Figure 6.17: SBP image of a ^{137}Cs source using Compton imaging with the 16-pillar H2DPI. The data presented in this image was acquired in one minute.

centered in both images at (0^o, 0^o). The difference between the two figures is that Figure 6.16 was generated using the approximate Compton imaging method with the 8-pillar H2DPI and Figure 6.17 was generated using Compton imaging with the 16-pillar prototype. For the same number of cone projections, the 16-pillar prototype better converges on the source location. Increasing the number of cone projections with the 8-pillar H2DPI does, however, converge on the source location as shown in Figure 6.18.

Comparing Figures 6.17 and 6.18 shows the direct improvement in imaging capabilities between the two systems and imaging methodologies. Incorporation of the inorganic scintillators corrects for the associated uncertainties in sequencing and energy of the incident gamma ray, which greatly improves gamma-ray source localization.

6.3.2 Gamma-Ray Image Resolution for a ^{137}Cs Source

A series of measurements were performed with a 100 μCi ^{137}Cs source. The source was placed on a similar system to the one developed for the ^{252}Cf source; shown in

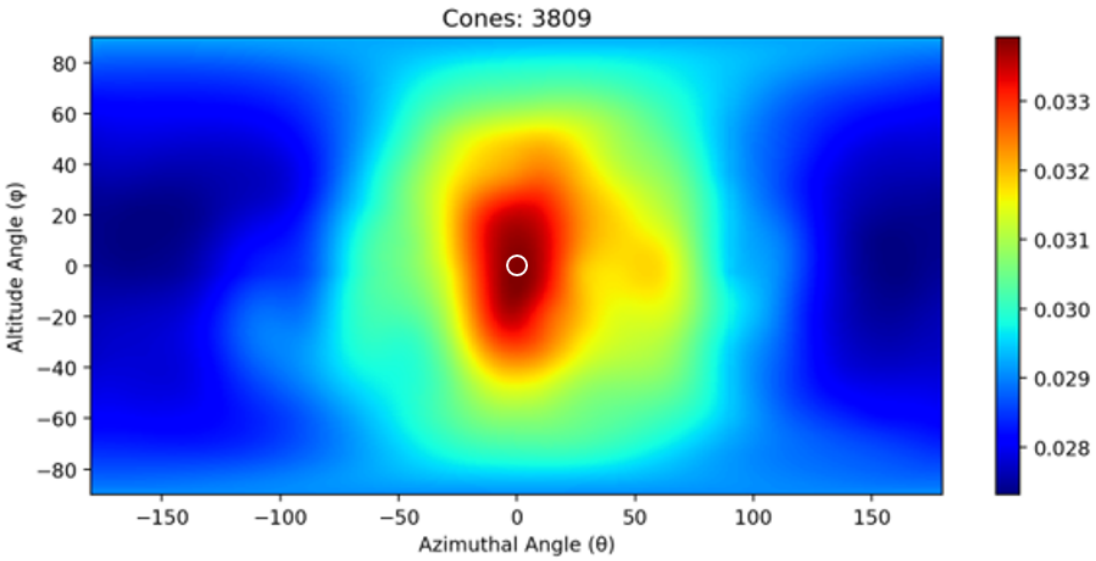

Figure 6.18: SBP image of a ^{137}Cs source using the Compton imaging method with the 8-pillar H2DPI. The data presented in this image was acquired in forty minutes.

Figure 6.8. The source was kept at a constant radius of 58.42 cm from the center of the H2DPI and the azimuthal angle was adjusted. The source was placed from -5 degrees to 25 degrees in 5 degree increments for 8.86 hours at each location. Calibration measurements were performed before and after the measurements to account for gain change. Coincident events between the stilbene pillars and $CeBr_3$ cylinders were summed to generate summed-coincident spectra. Events within the energy range of 661.7±37.56 keV were reconstructed to generate SBP images. LM-MLEM was then applied to generate images that converged on the most likely source distribution [49, 51]. The energy range used for this analysis is defined as plus or minus two standard deviations based on the summed-coincident spectrum resolution of 7% at 661.7 keV. The individual source reconstructions are shown in Figure 6.19. The azimuthal slices were taken from the LM-MLEM images where 20 iterations were applied, which is the same value applied to the neutron images. This value was chosen for both types of images based on visual inspection.

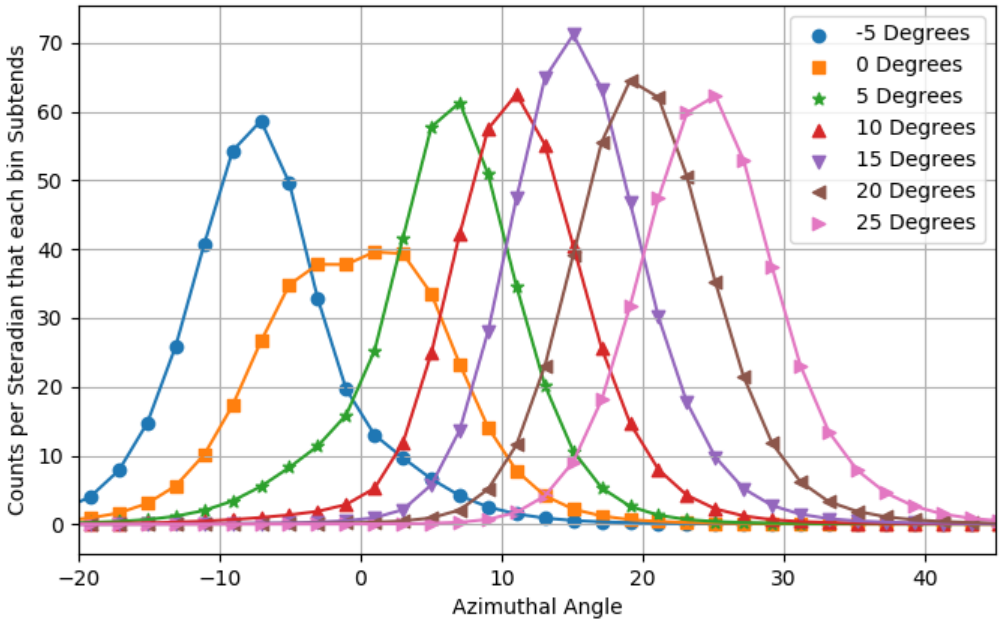

Figure 6.19: Azimuthal slices of the reconstructed gamma-ray images from the ^{137}Cs source generated using 20 iterations of LM-MLEM.

The source reconstruction at 0 degrees shown in Figure 6.19 has a distinctly different shape than the other source reconstructions. This shape difference is most likely due to a combination of the lever-arm distribution and the dominance of forward-scattering gamma-ray coincident events in the reconstruction. Combining the -5 degree data set with data sets at 5 degrees, 10 degrees and 15 degrees produces the azimuthal reconstructions shown in Figure 6.20.

Sources of equal intensity and energy that are symmetrically around 0 degrees can be resolved with an azimuthal separation angle of 10 degrees as shown in Figure 6.20. Further separating the second source location from 5 degrees to 15 degrees reconstructs both sources; with the source at the larger angle being more likely. This effect is because the source reconstruction at -5 degrees is broader than the source reconstruction at 15 degrees as shown in Figure 6.19. The full-width at tenth maximum (FWTM) for the source reconstruction at -5 degrees is 23.78 degrees and the FWTM for the reconstruction at 15 degrees is 20.93 degrees. Combining the data

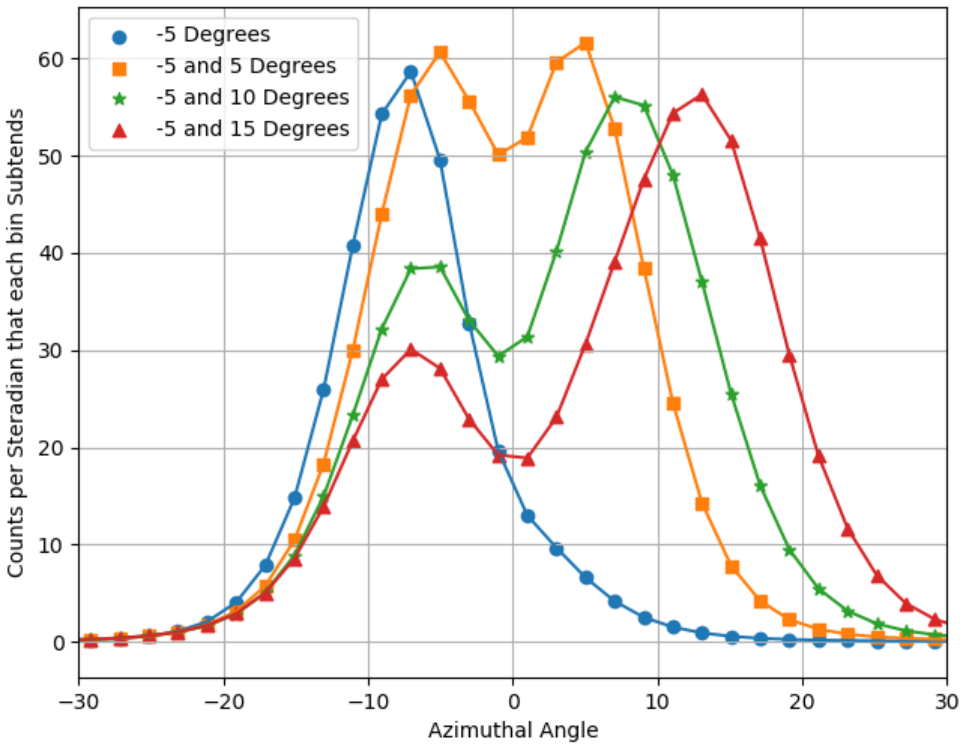

Figure 6.20: Azimuthal slices of the combined reconstructed gamma-ray images from the ^{137}Cs source generated using 20 iterations of LM-MLEM.

sets with the source at 0 degrees and the source at 25 degrees produces the azimuthal slices shown in Figure 6.21. Combining the two data sets produces a reconstruction that can be differentiated from either of the single sources, but does not distinctly reconstruct the two source locations like what is shown for the -5 and 5 degree case in Figure 6.21. Testing the reconstruction between positive azimuthal source positions produces Figure 6.22. This result demonstrates that the resolution is dependent on source location and specifically if the sources are symmetric about the center of the system.

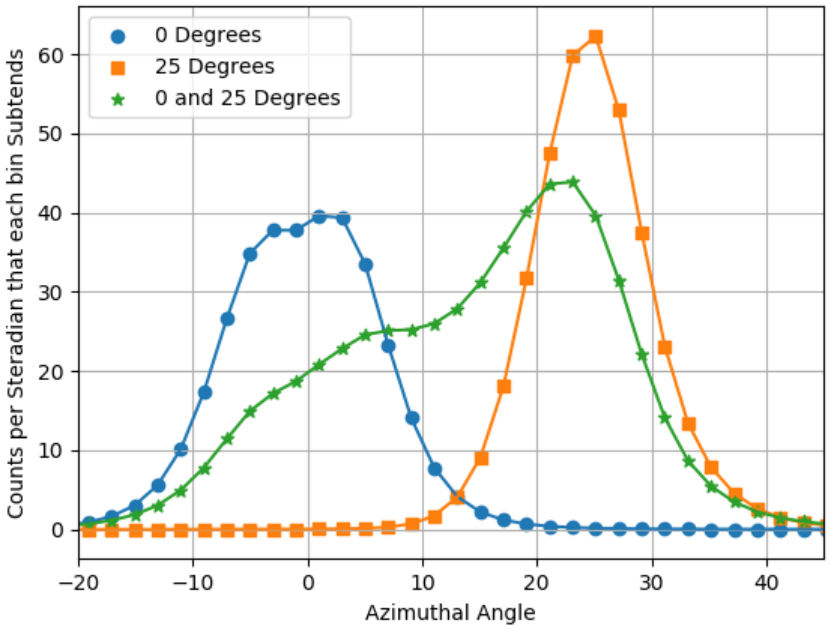

Figure 6.21: Azimuthal slices of the reconstructed gamma-ray images from the ^{137}Cs source generated using 20 iterations of LM-MLEM.

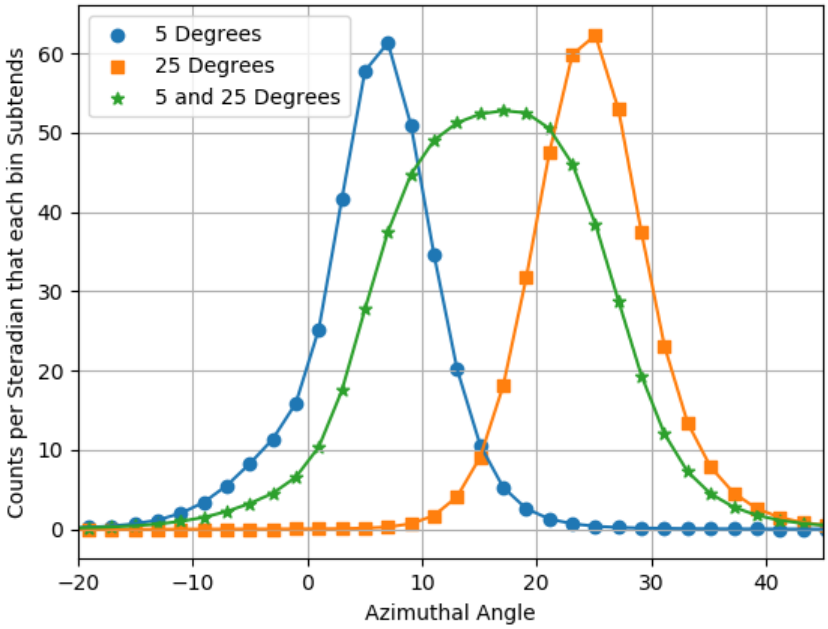

Figure 6.22: Azimuthal slice of the reconstructed gamma-ray images from the ^{137}Cs source generated using 20 iterations of LM-MLEM.

6.3.3 Reconstructing Gamma-Ray Sources with Neutron Sources in the Same Field of View

Figure 6.11 shows a photograph of a measurement setup where the 100-μCi ^{137}Cs source, a 6×10^6 n/s ^{252}Cf source, and a 10×10^6 n/s PuBe source were all measured

in the same field of view. Applying the charge integration method detailed in Section 5.4 allows for classification of gamma-ray interactions with minimal neutron misclassification. Gating on summed photopeaks then allows for specific source isolation. This technique was used to produce Figure 6.24, which demonstrates the capabilities of the H2DPI to localize a gamma-ray source in the presence of multiple neutron-emitting sources in a relatively quick time. The image shown in Figure 6.24 was generated with one minute of data and accurately localizes the ^{137}Cs sources.

Figure 6.23 shows the summed coincident energy spectrum from the measurement shown in Figure 6.10. The 661.7 keV gamma-ray from ^{137}Cs is shown in the measured spectrum. Projecting events within the energy range of 661.7±37.56 keV yields Figure 6.24.

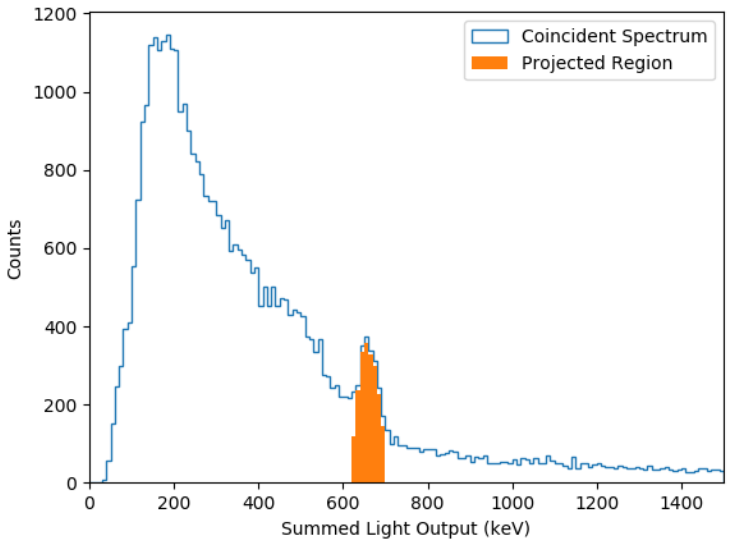

Figure 6.23: Measured coincident energy spectrum from the experimental setup shown in Figure 10. This spectrum was acquired in 15 minutes.

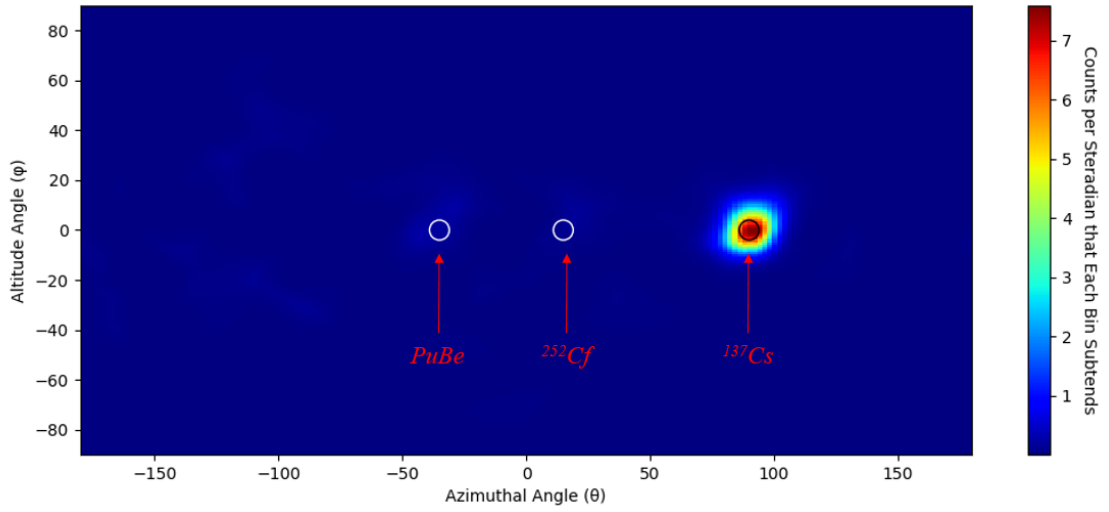

Figure 6.24: Gamma-Ray image of the ^{137}Cs sources (black circle) reconstructed from events in the energy range of 661.7±37.56 keVee with 20 iterations of LM-MLEM applied to the data set. The image is composed of 1559 cone projections acquired over a 15 minute measurement. The location of the ^{252}Cf and PuBe sources are shown as white circles.

6.3.4 Isolating ^{137}Cs and ^{22}Na Sources

To demonstrate the capability of the prototype H2DPI to image multiple gamma-ray sources, two gamma-ray sources, a 100 μCi ^{137}Cs source and a 100 μCi ^{22}Na source, were measured for 45 minutes at a radius of 58.42 cm. The two sources were separated by 20 degrees in the azimuthal direction and centered in the altitude direction with the H2DPI. Figure 6.25 shows a photograph of the measurement setup. Calibration measurements were performed before and after the measurement to account for gain change over the course of the measurement.

The energy deposition of coincident events between a given stilbene pillar and $CeBr_3$ cylinder are summed to produce a summed-coincident energy spectrum as shown in Figure 6.26. Figure 6.26 shows the 511 keV annihilation peak from ^{22}Na and the 661.7 keV gamma-ray peak emitted from ^{137}Cs. A continuum up to the summed peak of 1274 is also present with a broad peak at 1274 keV. Projecting events within the range 511±33.01 keV yields Figure 6.27 and projecting events within the range

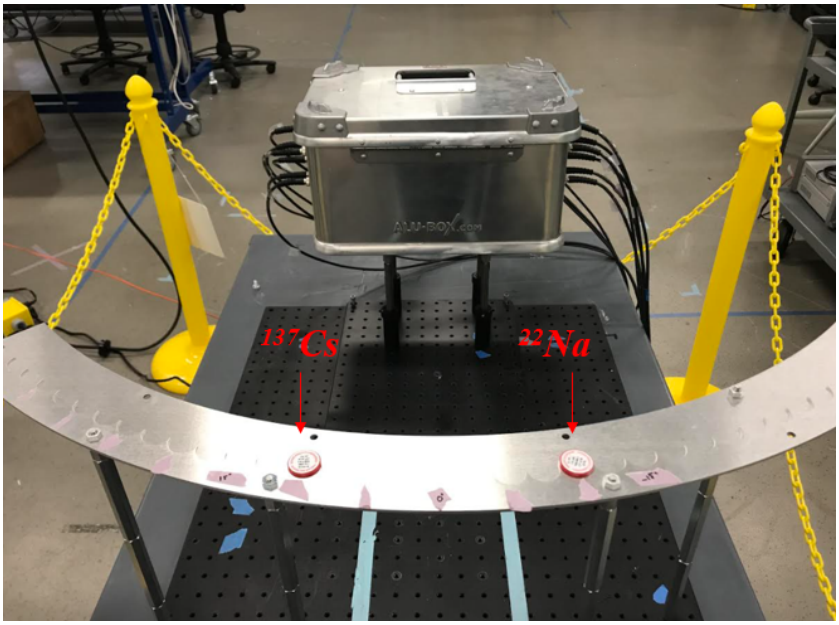

Figure 6.25: Photograph of the experimental setup to measure a 100 μCi ^{137}Cs source and a 100 μCi ^{22}Na source at a radius of 58.42 cm and separated by 20 degrees.

661.7±37.56 keV yields Figure 6.28. The regions for both energies are plus or minus two standard deviations based on the coincident energy resolution. A circle with a radius of four degrees is used in both of these images to show the source locations. The radius of the circles was chosen arbitrarily.

6.3.5 Passive Gamma-Ray Imaging of Special Nuclear Material

Imaging in-lab check sources allows for the simple demonstration of Compton imaging capabilities and techniques. Localizing sources such as ^{137}Cs is rather simplistic even in the presence of other sources due to the mono-energetic gamma-ray emission of the source. While localizing or monitoring these types of sources could be useful in certain scenarios, it is necessary that the system can specifically localize and identify SNM. Chapter II demonstrated that SNM can be localized well using neutron imaging, but had difficulty localizing the gamma rays emitted by the presented sources. The following sections demonstrate the improved Compton imaging

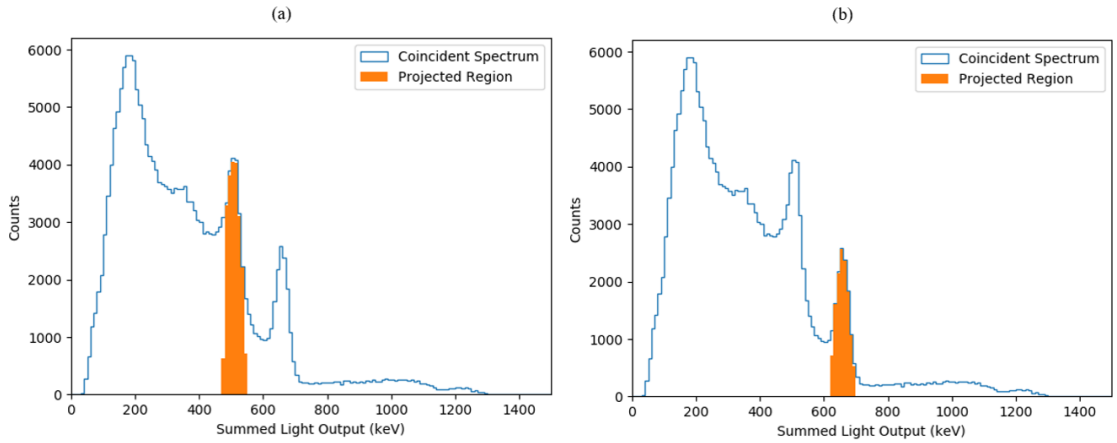

Figure 6.26: Measured coincident energy spectrum from the experimental setup shown in Figure 6.25. The highlighted region in (a) shows the projection region for the ^{22}Na and the highlighted region in (b) shows the projection region for ^{137}Cs.

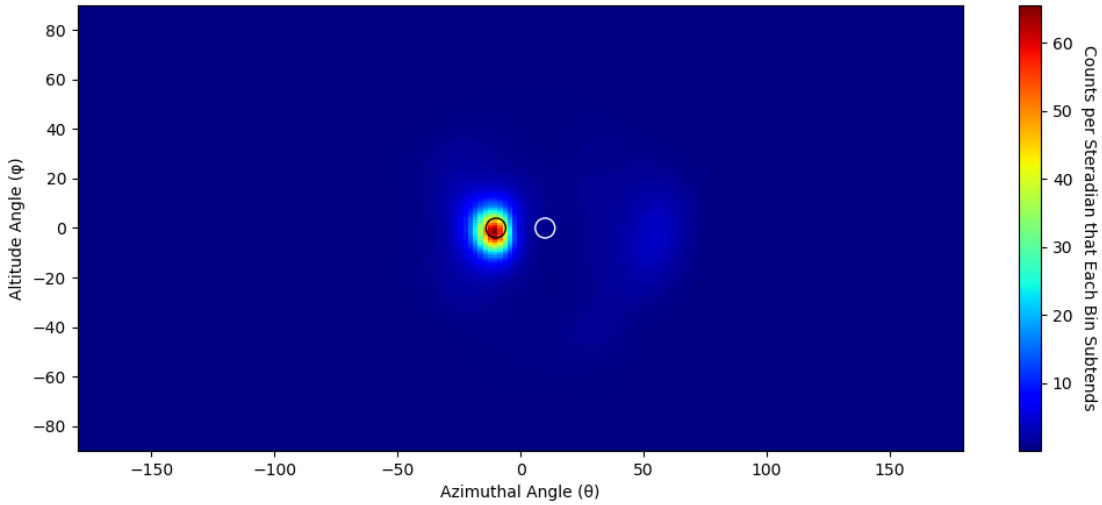

Figure 6.27: Image of the ^{22}Na source (black circle) reconstructed from events in the energy range of 511±33.01 keV with 20 iterations of LM-MLEM applied to the data set. The location of the ^{137}Cs source is shown as a white circle.

capability of the 16-pillar H2DPI by localizing a 10-kg mock sphere of HEU and a 100-g disk of plutonium (94% ^{239}Pu). Each object was localized independently and both sources were imaged in the same field of view.

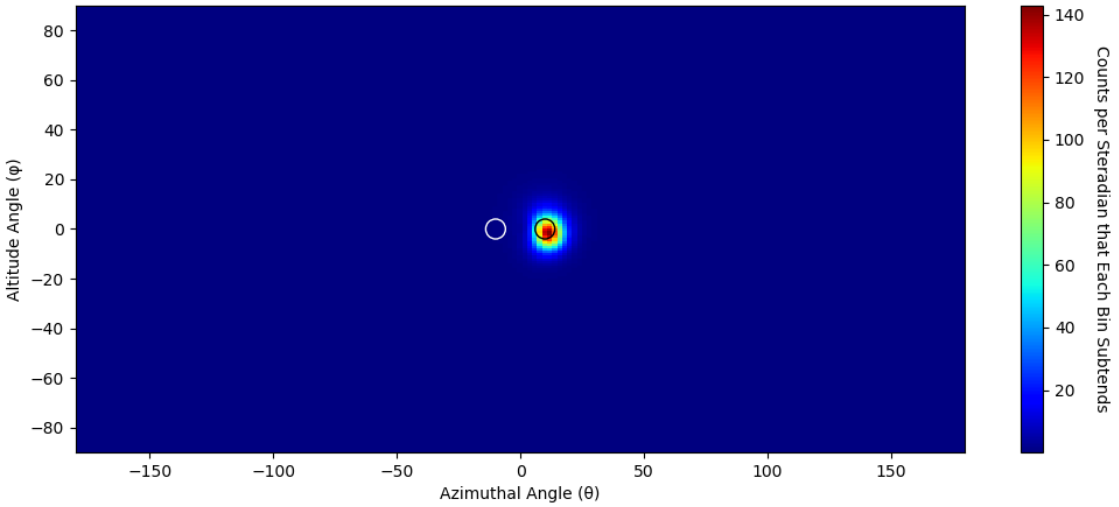

Figure 6.28: Image of the ^{137}Cs source (black circle) reconstructed from events in the energy range of 661.7±37.56 keV with 20 iterations of LM-MLEM applied to the data set. The location of the ^{22}Na source is shown as a white circle.

6.3.6 Passive Gamma-Ray Imaging of Highly Enriched Uranium

Figure 6.29 shows a diagram of the mock 10-kg sphere of HEU known as "Taz". Mock in this case means that the sphere gives off a gamma-ray signature consistent with what would be expected from an actual 10-kg sphere of HEU. The sphere is composed of a 799-g depleted uranium core with a radius of 2.184 cm, an aluminum spacer with an exterior radius of 4.97 cm, a 1133-g metal enriched uranium-aluminum alloy shell with an external radius of 6.0065 cm and an exterior titanium shell. The composition of the uranium-aluminum alloy shell is 11.8% uranium where the uranium has an average enrichment of 92.87% [3].

6.3.6.1 Measurement Setup

Figure 6.30 shows the measurement setup for Taz. Taz was placed at a radius of 46.7 cm from center of the system at an azimuthal and altitude location of (22.38^o,-0.4^o) relative to the center of the H2DPI. The object was measured overnight for 18.3

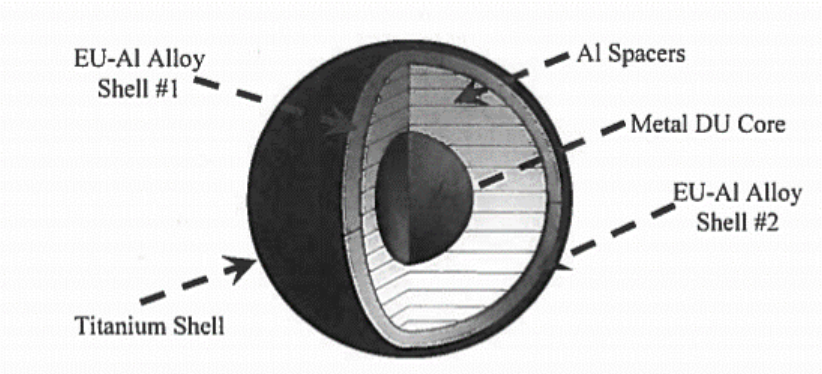

Figure 6.29: Diagram showing the makeup of a 10-kg mock HEU sphere [3]

hours. ^{137}Cs measurements were taken before and after the measurement to account for gain change.

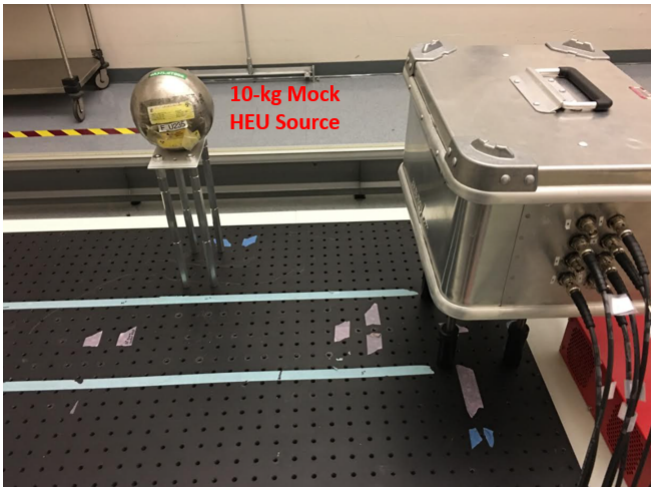

Figure 6.30: Photograph of the measurement setup used to measure Taz.

6.3.6.2 Measurement Results

Figures 6.31 and 6.32 show the gamma-ray spectroscopic response of the H2DPI to a mock HEU object. Analyzing the single spectrum shown in Figure 6.31 clearly shows the 185.7 keV peak that is a key signature of ^{235}U. A lower energy peak at 143.8 keV can also be identified as well as the x-rays from uranium around 93.4 keV. Analyzing the coincident spectrum clearly shows the 185.7 keV peak in coincidence along with some coincidence of the 143.8 keV peak. The coincidence spectrum does

not show significant information below the 143.8 keV peak due to the threshold that was applied to this measurement. The other isotope of uranium that is commonly analyzed as well is ^{238}U. Within the ^{238}U decay scheme, a 1001 keV gamma ray is emitted that is characteristic of the presence of the ^{238}U isotope. Figure 6.32 shows the same spectra as Figure 6.31 but on a log scale and up to 1250 keV. Due to the low emission rate of the 1001 keV gamma ray and the efficiency of the H2DPI, the 1001 keV gamma-ray is not observed in either spectra in Figure 6.32.

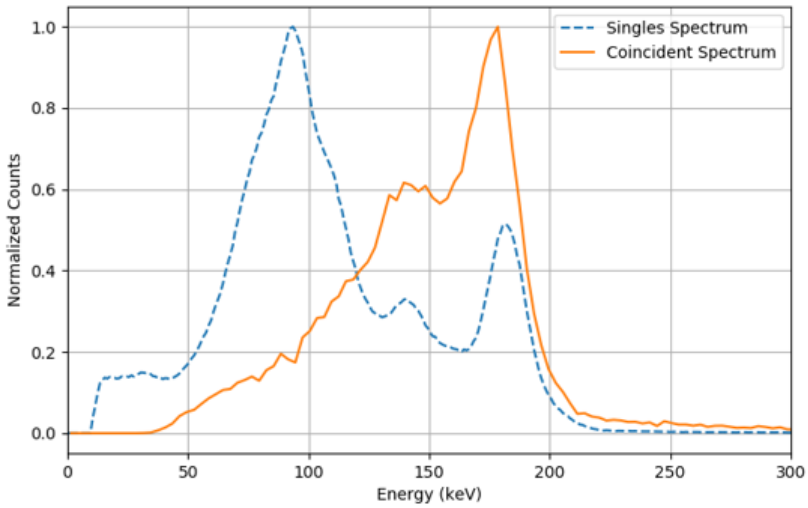

Figure 6.31: Comparison between the measured gamma-ray energy spectrum for a single $CeBr_3$ cylinder and the coincident spectrum between all stilbene pillars and $CeBr_3$ cylinders for Taz. The two spectra are normalized to easily compare them.

Gating on the 185.7 keV peak in the region of 185.7±18.6 keV for the coincident spectrum in Figure 6.31 yields the image shown in Figure 6.33. The count rate for the gated coincident region was found to be 15.67 cone projections per minute. The outline of the sphere is shown in black in the correct azimuthal and altitude coordinates. The reconstruction matches well with the correct source location, but is slightly off centered in the positive azimuthal direction. This effect is due to a combination of the lower energy of the reconstructed gamma ray and the asymmetry of the H2DPI design relative to the positive azimuthal direction.

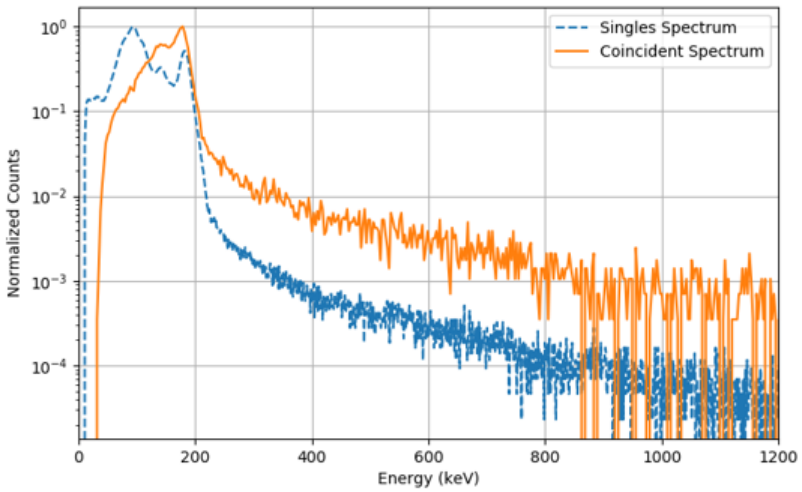

Figure 6.32: Comparison between the measured gamma-ray energy spectrum for a single $CeBr_3$ cylinder and the coincident spectrum between all stilbene pillars and $CeBr_3$ cylinders for Taz shown on a log scale to visualize higher-energy gamma-ray interactions.

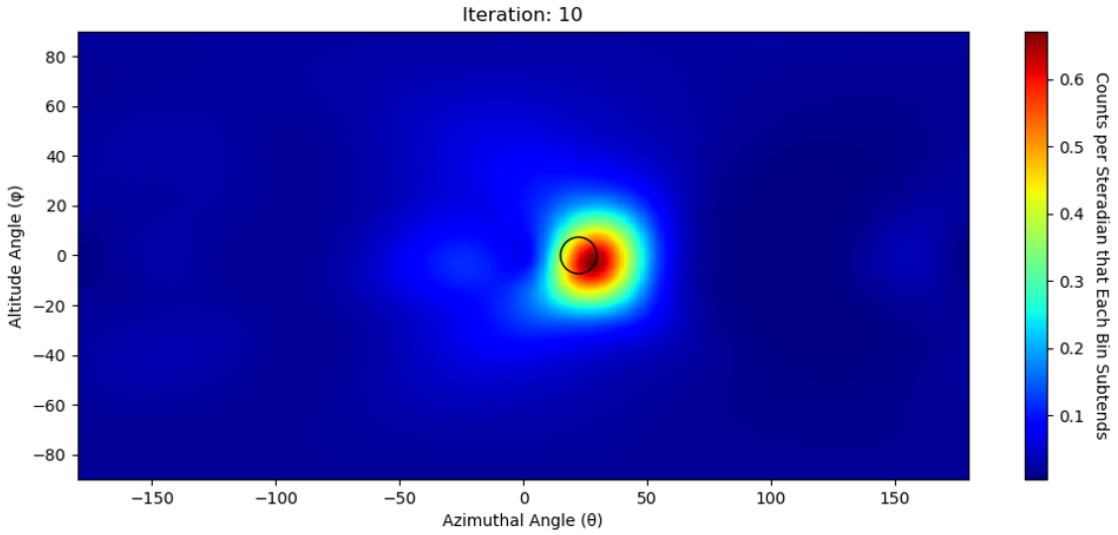

Figure 6.33: Reconstructed gamma-ray image of Taz composed of 5,000 cone projections measured in 5.3 hours with 10 iterations of LM-MLEM applied.

6.3.7 Passive Gamma-Ray Imaging of Plutonium

Figure 6.34 shows a diagram of the plutonium disk source known as PSS-006 that was measured using the H2DPI. The source is composed of a puck of plutonium with a thickness of 0.062 inches and a diameter of 2.896 inches. The mass of the puck is

104.1 g where 98.25 % of the mass is plutonium. Of that plutonium mass, 93.9351% is ^{239}Pu [4]. The exact dimensions of the housing and material composition of the housing are not known.

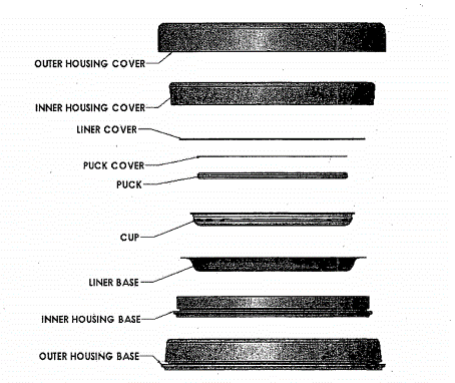

Figure 6.34: Diagram showing the components and housing making up the sealed plutonium disk source known as PSS-006 [4].

6.3.7.1 Measurement Setup

The plutonium disk was placed perpendicular to the system at a radius of 27.5 cm at angular coordinates of (-33.69^o, -2.55^o) as shown in Figure 6.40. The disk was measured for 17.5 hours where ^{137}Cs measurements were taken before and after the measurement to account for gain change.

6.3.7.2 Measurement Results

Figures 6.36 and 6.37 show the gamma-ray spectroscopic response of the H2DPI to the plutonium disk. Analyzing the single spectrum shown in Figure 6.36 shows a more complex spectrum than was recorded with Taz. Clear peaks can be identified in the singles spectrum at the following energies (keV): 146, 203, 333/345, 375 and 413. Looking at higher energies in Figure 6.37 shows a clear peak as well at 646 keV in both the singles and coincident spectrum. Table 6.4 lists the resulting cone projection rate for several of the peak regions in the coincident spectrum.

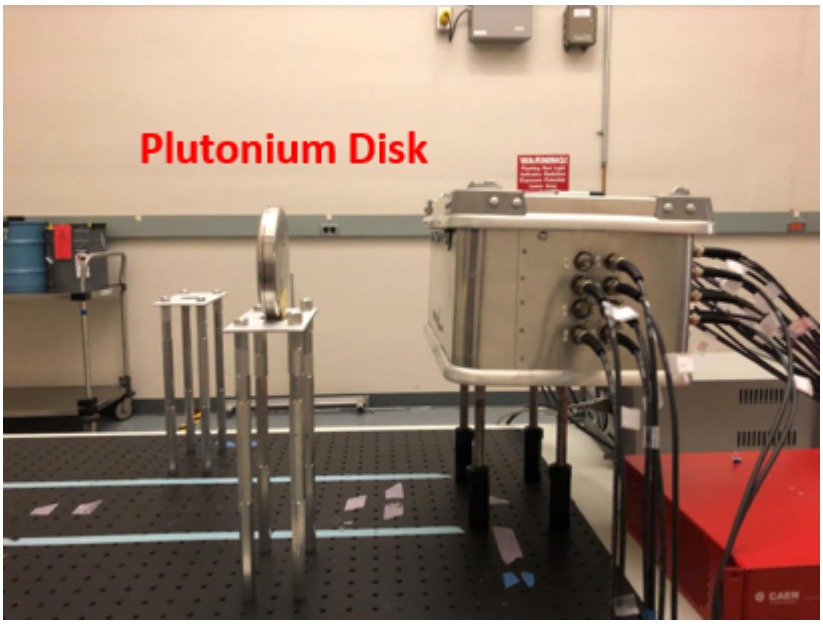

Figure 6.35: Photograph of the measurement setup used to measure PSS-006.

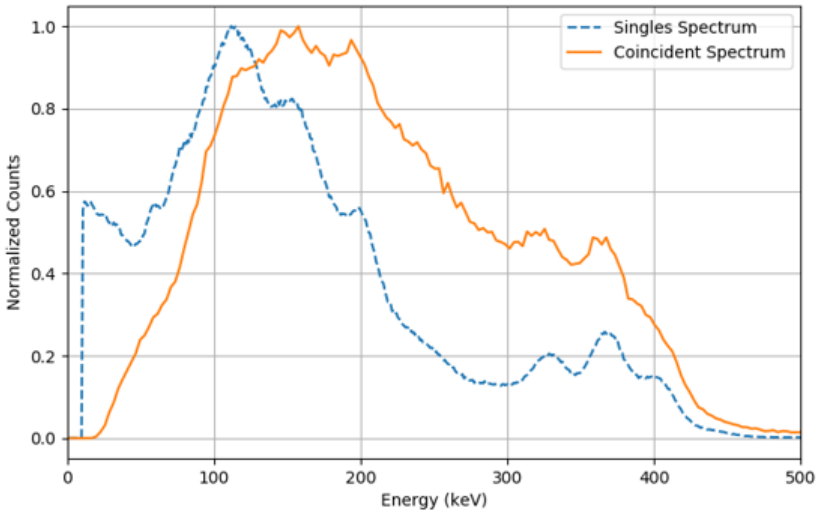

Figure 6.36: Comparison between the measured gamma-ray energy spectrum for a single $CeBr_3$ cylinder and the coincident spectrum between all stilbene pillars and $CeBr_3$ cylinders for Taz. The two spectra are normalized to easily compare them.

Reconstructed events with the 203±20.3 keV region of the coincident energy spectrum produces Figure 6.42. The outline of the plutonium disk in Figure 6.42 is slightly distorted due to the intersection of a perpendicular cylinder with a spherical projection. The reconstruction, however, does converge on the correct source location.

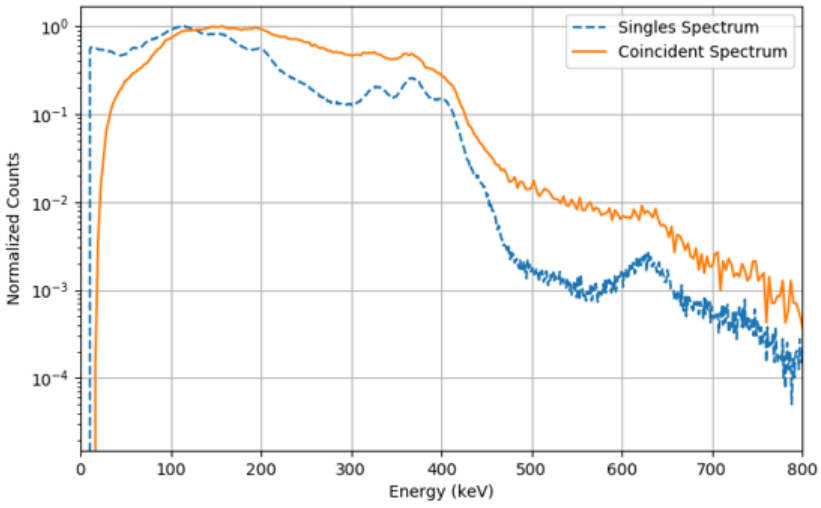

Figure 6.37: Comparison between the measured gamma-ray energy spectrum for a single $CeBr_3$ cylinder and the coincident spectrum between all stilbene pillars and $CeBr_3$ cylinders for Taz shown on a log scale to visualize higher-energy gamma-ray interactions.

Table 6.4: Imageable gamma-ray event rate in specified regions for PSS-006.

Plutonium Gamma Ray (keV)	Energy Region (keV)	Count Rate (projections per minute)
203	± 20.3	47.99
333/345	± 16.7	23.20
375/413	± 18.8	28.28
646	± 32.3	00.61

There is also a substantial amount of noise in the image. We believe this noise is due to two main aspects. The first being that there are a significant number of backscatter events making up the image. These backscatter events are overlaying to produce the structure around the altitude planes of $\pm 70^{o}$. In addition, there is added noise to the image because the 203 keV peak is on a significant continuum from higher energy gamma-ray coincident events. While most of these events will not reconstruct to a physical event, some will and cannot be differentiated from a true Compton imaging event from that energy gamma ray. As Figures 6.36 and 6.37, plutonium emits many more higher-energy gamma rays. Reconstructing with the 375±18.8 keV region of the coincident energy spectrum produces Figure 6.43. Figure 6.43 shows excellent

localization of the plutonium disk with minimal image artifacts.

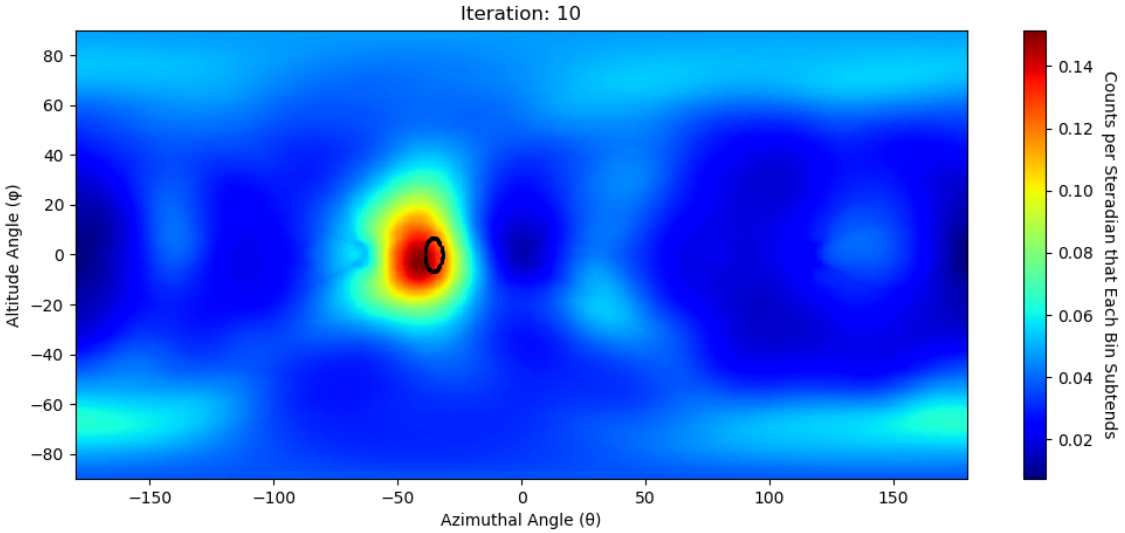

Figure 6.38: Reconstructed gamma-ray image of the plutonium disk composed of 5,000 cone projections measured in 1.7 hours with 10 iterations of LM-MLEM applied. The energy region used for generating the cone projections was 203±20.3 keV.

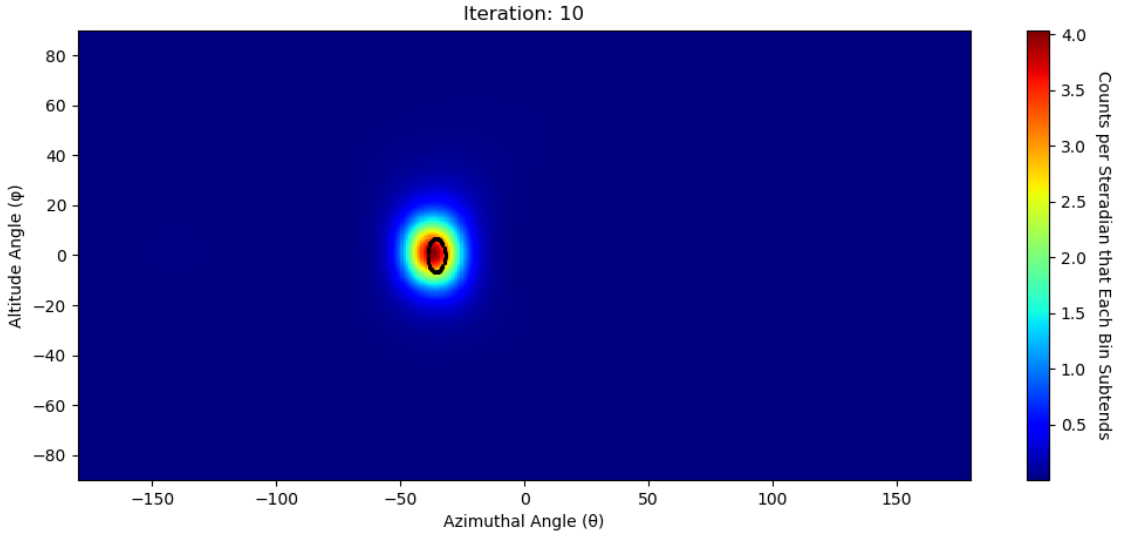

Figure 6.39: Reconstructed gamma-ray image of the plutonium disk composed of 5,000 cone projections measured in 2.9 hours with 10 iterations of LM-MLEM applied. The energy region used for generating the cone projections was 375±18.8 keV.

6.3.8 Passive Gamma-Ray Imaging of Plutonium and Highly Enriched Uranium in the Same Field of View

Demonstrating the localization of independent source of SNM can show capabilities of a system but does not necessarily show the limits of an imaging system. To further demonstrate the capabilities of the H2DPI to localize multiple SNM objects by passive gamma-ray imaging, both Taz and PSS-006 were measured in the same field of view.

6.3.8.1 Measurement Setup

Figure 6.40 shows the measurement setup for measuring Taz and PSS-006 in the same field of view. Taz was placed at a radius of 46.7 cm from center of the system at an azimuthal and altitude location of (22.38^o,-0.4^o) relative to the center of the H2DPI. PSS-006 was shifted slightly relative to the previous measurement. PSS-006 was placed at a radius of 31.0 cm and angular location of (-34.99^o, -2.55^o). PSS-006 was slightly shifted for this measurement due to concern that separation between the sources would not be achieved. As will be demonstrated in the following section, that concern was not warranted. Data were taken in the setup shown in Figure 6.40 for 23.67 hours. ^{137}Cs measurements were taken before and after the measurement to account for gain change.

6.3.8.2 Measurement Results

Figure 6.41 compares the measured singles spectra between these three measurements: independent measurement of Taz, independent measurement of PSS-006 and both objects in the same field of view. The 185.7 keV gamma-ray peak can be clearly identified on top of the plutonium spectrum with both sources present. Imaging this peak in for the coincident spectrum region of 186±18.6 keV produces Figure 6.42. Figure 6.42 converges on both sources well. The reason for the convergence on

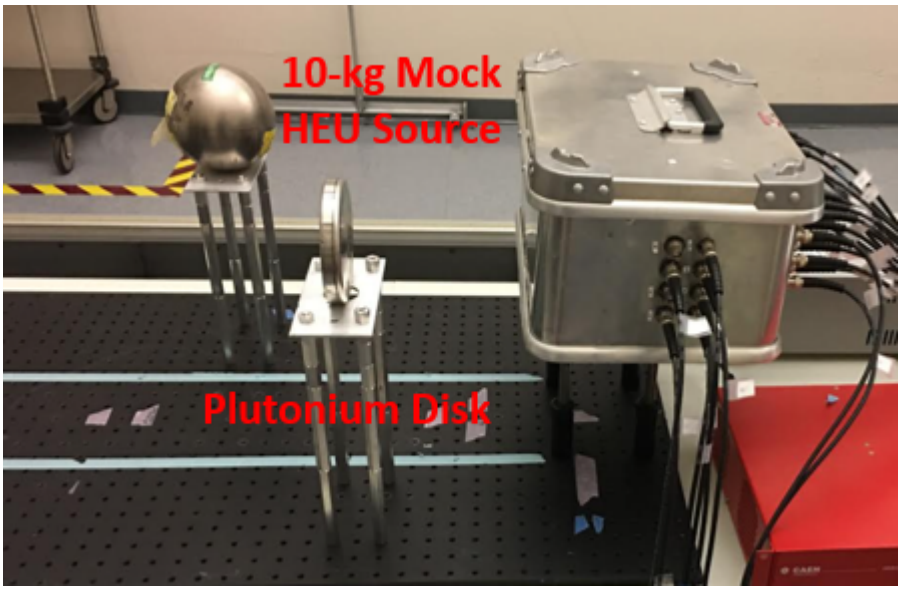

Figure 6.40: Photograph of the measurement setup used to measure PSS-006.

PSS-006 in this imaging region is because of the broadening around the 203 and 146 keV peaks from ^{239}Pu. True events from these gamma rays are being reconstructed correctly in the defined imaging region. PSS-006, because it is a plutonium source, can then be independently localized in this measurement by imaging a higher energy gamma ray. Figure 6.43 shows the reconstruction from the 375±18.8 keV region of the coincident spectrum. This result clearly demonstrates that the plutonium source can be localized relative to the HEU source.

6.3.9 Passive Gamma-Ray Imaging Conclusions

Incorporation of inorganic scintillators into the prototype H2DPI was done to improve spectroscopic capabilities and Compton imaging performance relative to the previous iteration of the H2DPI. The previous Compton imaging method with the 8-pillar H2DPI struggled to converge well on gamma-ray source locations and failed at being able to resolve multiple sources in the same field of view. Results from this chapter demonstrate that with the addition of $CeBr_3$ scintillators into the design of the H2DPI, localization and identification of SNM can be accurately performed via

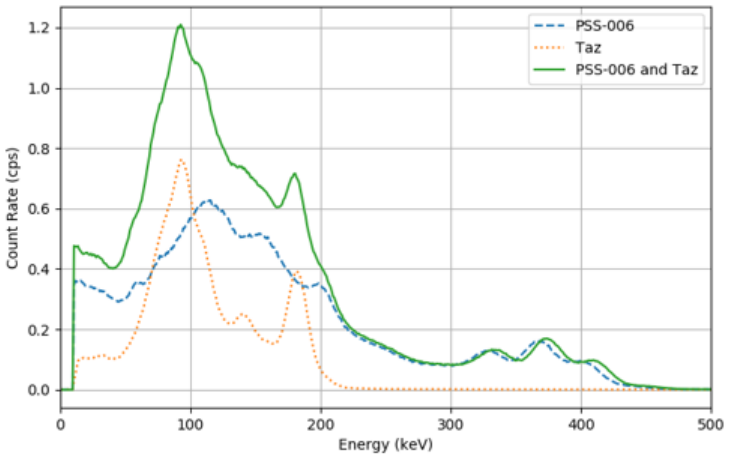

Figure 6.41: Comparison between the measured gamma-ray energy spectra for a single $CeBr_3$ cylinder for the independent measurements and with both objects in the same field of view.

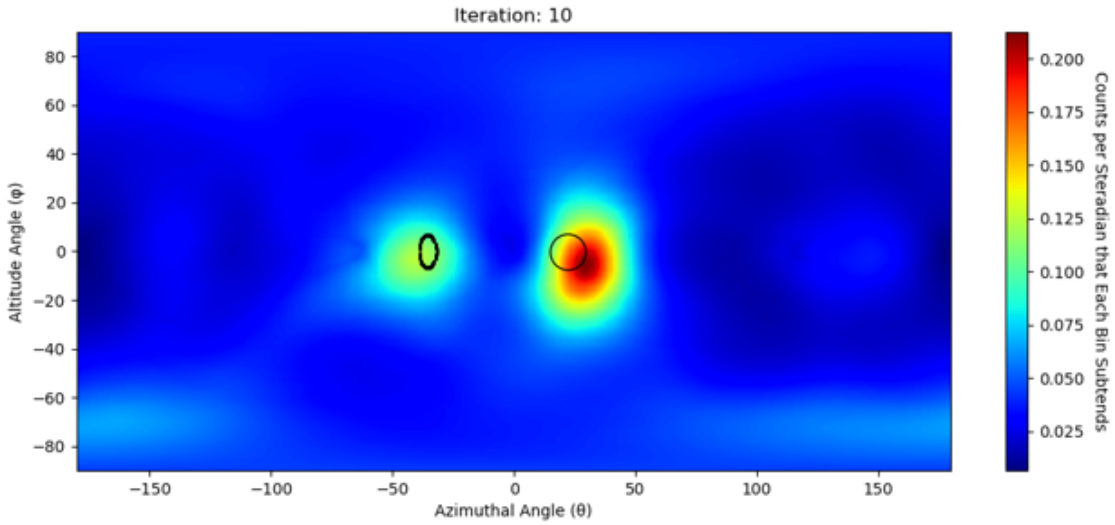

Figure 6.42: Reconstructed gamma-ray image of both objects composed of 5,000 cone projections measured in 1.2 hours with 10 iterations of LM-MLEM applied. The energy region used for generating the cone projections was 186±18.6 keV.

Compton imaging and spectroscopic identification.

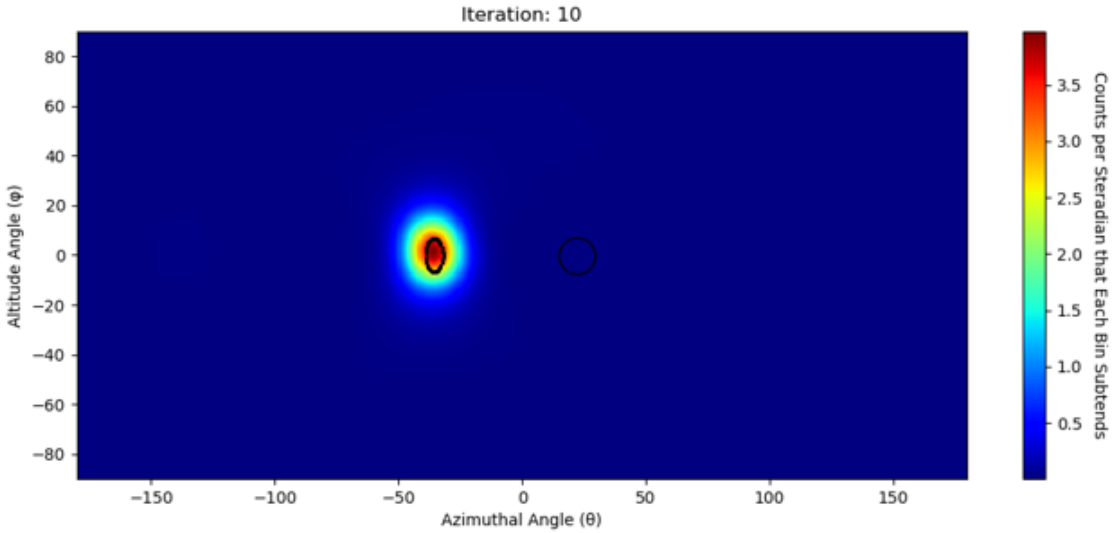

Figure 6.43: Reconstructed gamma-ray image of the plutonium disk composed of 5,000 cone projections measured in 2.9 hours with 10 iterations of LM-MLEM applied. The energy region used for generating the cone projections was 375±18.8 keV.

CHAPTER VII

Validating MCNP-PoliMi Models of the H2DPI

Chapter VI showed the imaging capabilities of the prototype H2DPI composed of 12 pillars of stilbene and 8 $CeBr_3$ cylinders. The SensL array used for this prototype, however, contains 64 pixels. A fully realized system could thus contain up to 64 stilbene pillars or some combination of stilbene and $CeBr_3$ totaling 64 pillars. To assess the capabilities of such a system, simulations were created and validated with the 16-pillar H2DPI using MCNPX-PoliMi. These validated models were then applied to a simulated 64-pillar system.

Figure 7.1 shows a 3D display of the active volumes in the 16-pillar simulation model. Support structures, optical interfaces, SiPM arrays, PCBs, table and concrete floor were all included within the simulation but are not shown in the 3D rendering. The following two sections will describe the model and validation of the response of the 16-pillar H2DPI to neutrons emitted by a ^{252}Cf source and gamma rays emitted by a ^{137}Cs source.

7.1 Validating the Simulated Neutron Response of the H2DPI

A well characterized measurement of a ^{252}Cf source was needed to compare with the simulated response of the H2DPI. Figure 7.2 shows the measurement setup used to compare with simulations. The spontaneous fission rate of the ^{252}Cf source on the

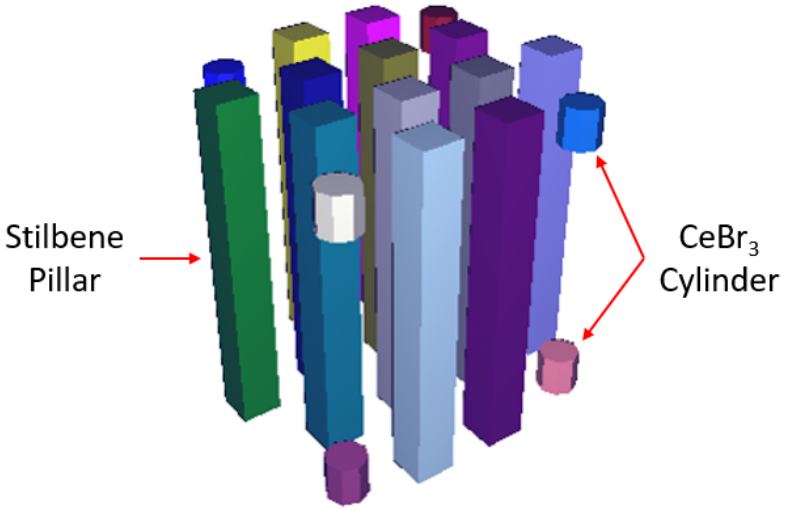

Figure 7.1: 3D rendering of the scintillators in the H2DPI using Vised. The pillars are stilbene ($6\times6\times50.5$ mm^3) and the cylinders are $CeBr_3$ ($6\times6\varnothing$ mm^3).

measurement date was estimated to be 1.61×10^6 $\frac{fis}{s}$. The source was placed 58.42 cm from the center of the H2DPI and measured for two hours. Calibration measurements were performed before and after the measurement to account for any gain change over the course of the measurement.

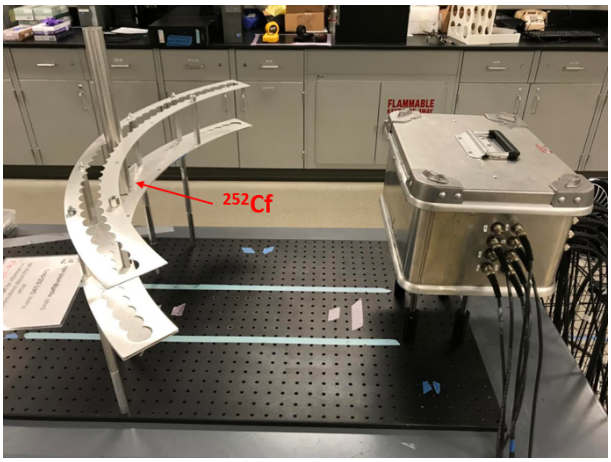

Figure 7.2: Photograph of the experimental setup used to measure a ^{252}Cf source 58.42 cm from the center of the H2DPI. The source was centered in both the azimuthal and altitude directions.

7.1.1 Simulating Neutron Pulses

MCNPX-PoliMi outputs a collision file containing the interaction information for any particle interaction within a defined volume [62]. Obtaining the individual interaction information is particularly useful since the light output from neutron elastic scattering off hydrogen is not linearly related to the energy deposited [19, 59, 93].

A program was made to convert the collision files into simulated pulses. Energy depositions within a stilbene pillar were converted from energy deposited to light output where appropriate light-output curves were applied to each pillar based on their orientation. Due to the magnitude of the anisotropic response of the system, applying the appropriate light-output curves is necessary to achieve the correct system response. If a series of collisions within a single volume contained at least one neutron elastically scattering off hydrogen, then that event was considered a neutron event. Events containing only gamma-ray interactions were not counted at this point. The light output for multiple interactions within a volume were summed together to determine the total light output of the simulated pulse. It was assumed that the light output from carbon recoils was equal to 1.5 % of the total energy deposition for neutrons elastically scattering off carbon [77]. Total light-output values were then broadened based on the measured energy resolution of the stilbene pillars. The total light-output value for the pulse was assumed to be the mean of a Gaussian distribution where the standard deviation was found using the measured GEB factors. This Gaussian distribution was randomly sampled to obtain the broadened light-output value. Pulses were then randomly sampled based on the measured percent removal rate for the neutrons removed due to the applied PSD threshold. Interaction location of the pulses was set to the center of the pillars in the x and y directions. If multiple interactions occurred, both the start time of the pulse and z position of the pulse were weighted by the relative light-output values for each interaction. Z positions were then broadened using the same random sampling method applied to the light output with

the difference being that the standard deviation of the Gaussian distribution to be sampled is both a function of the interaction location and the light output. Once a broadened Z position was determined, the uncertainty in Z position was determined for that new location. For an interaction to be counted, the reconstructed Z position must be within one standard deviation from the edge of the pillar. Broadening of the interaction time was only performed for the time difference between coincident events in independent volumes. The same random sampling methodology was applied to determine the broadened time difference between interactions. It should be noted that it was assumed for this analysis that the time resolution, 511 ps (FWHM), is constant as a function of light output and interaction location.

7.1.2 Simulating Neutron Spectra

Applying the methodology detailed in Section 7.1.1 with a 50 keVee light-output threshold to single interactions within one of the front stilbene pillars yields the red-dashed distribution in Figure 7.3. This distribution is compared with the experimental result shown as a solid blue line. Error bars for the simulation are a single standard deviation assuming a 5 % uncertainty in the source activity. Error bars for the experimental data are a single standard deviation assuming Poisson statistics. Both a (a) log and (b) linear scale are shown in Figure 7.3 to show that there is good agreement between the simulated and experimental results. The average count-rate difference between the experimental and simulated count rates for the twelve stilbene pillars is -0.30±3.89 %.

Further applying the methodology detailed in Section 7.1.1 to coincident neutron events with a time difference between 217 and 8825 ps yields the simulated and experimental neutron energy spectra shown in Figure 7.4. Error bars for the simulation are a single standard deviation assuming a 5 % uncertainty in the source activity. Error bars for the experimental data are a single standard deviation assuming Pois-

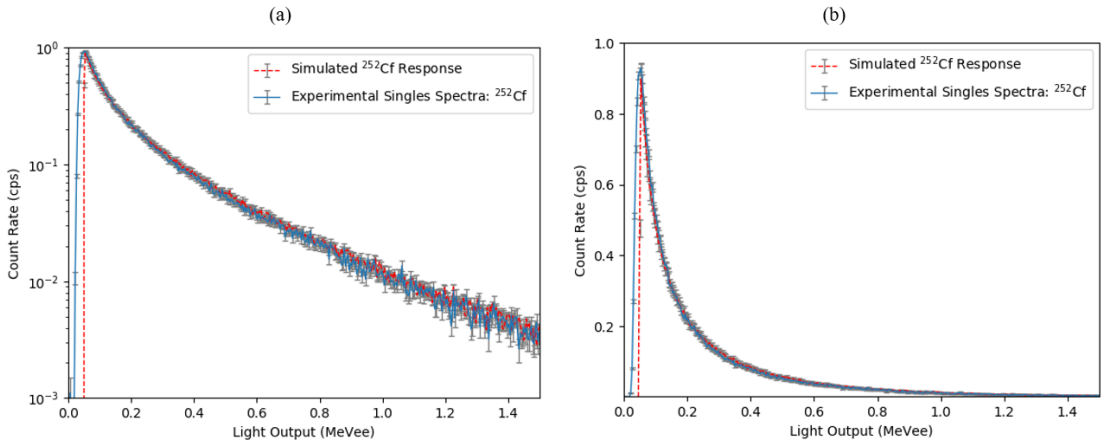

Figure 7.3: Comparison between the experimental and simulated single-neutron spectra for one of the front pillars of stilbene within the H2DPI shown on a (a) log scale and (b) linear scale.

son statistics. There is good agreement between the experimental and simulated energy spectra although the simulation is over predicting the number of interactions by 11.08±1.25 %. The primary reason for this overestimation is most likely due to the magnitude of the light-output curves. Section 5.5 compares the ratio of light-output curves that were measured using a TOF experiment with results published by Weldon et al, [2]. Ratios were compared to mitigate experimental differences that may impact the absolute magnitude of the light-output curves. Comparing the ratios, either the L_a and L_b curves are over predicting the light output or the magnitude of the $L_{c'}$ is being under predicting. Over prediction of the L_a light-output curve would explain the overestimation in the number of simulated events.

7.1.3 Simulating a Fully-Populated Stilbene-Based H2DPI

The validated methodology detailed in Section 7.1.2 was then applied to a simulation of a fully-populated 64-pillar stilbene-based H2DPI. A 3D rendering of this system is shown in Figure 7.5. A 1.61×10^6 $\frac{fis}{s}$ ^{252}Cf source was simulated at a distance of 1 m and 61 m to give an idea of how quickly a fully realized system could

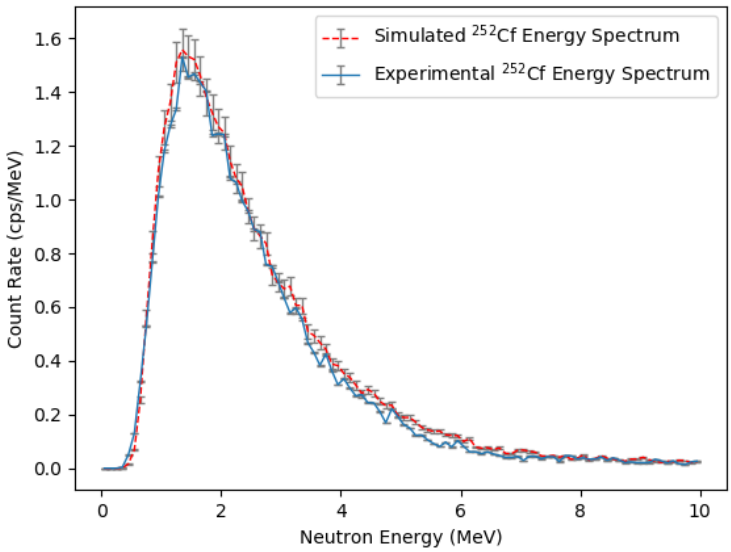

Figure 7.4: Comparison between the experimental and simulated neutron energy spectra for the H2DPI for a ^{252}Cf source centered 58.42 cm from the center of the H2DPI.

image a significant neutron source. The number of cone projections per second for the 1 m case was found to be 18.73 projections per second. The resulting SBP images for the source at both distances are shown in Figures 7.6-7.8. The source location is denoted as a white circle at the center of each of the figures in this chapter.

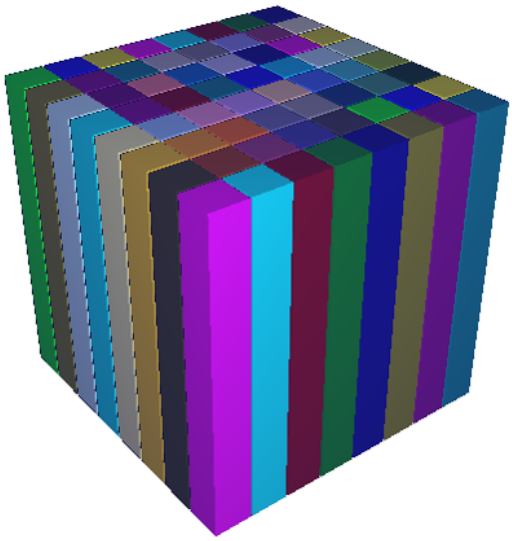

Figure 7.5: 3D rendering of the scintillators in the fully-populated H2DPI using Vised. The pillars are composed of stilbene ($6\times6\times50.5$ mm^3).

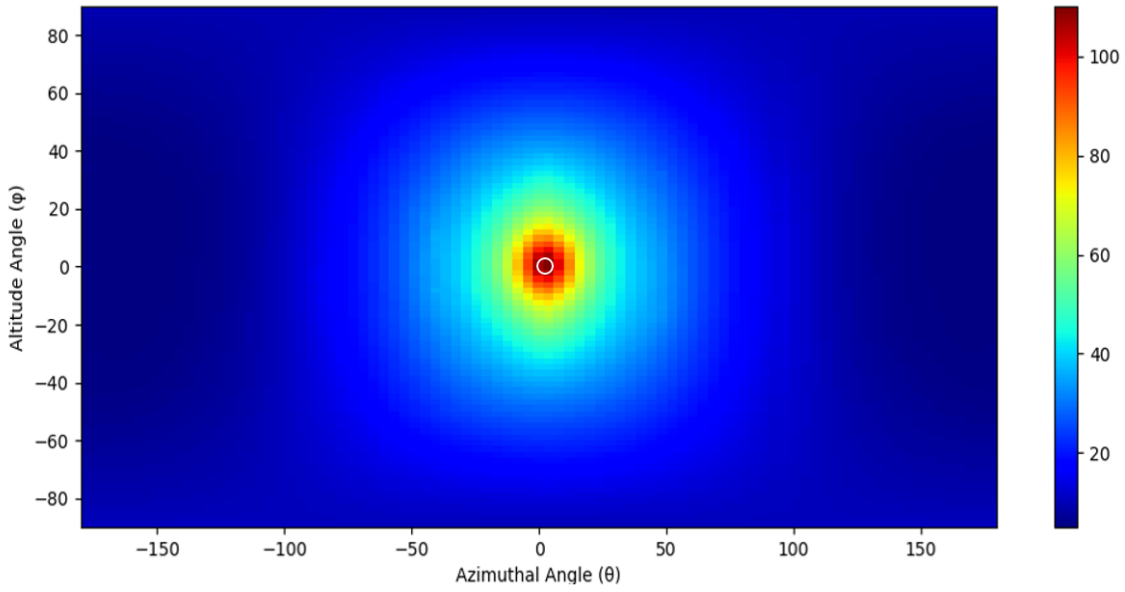

Figure 7.6: Simulated SBP image of a 1.61×10^6 $\frac{fis}{s}$ ^{252}Cf source measured at a distance of 1 m at an angular location of (0^o,0^o) for 115.1 minutes. The image is composed of 129,408 cone projections.

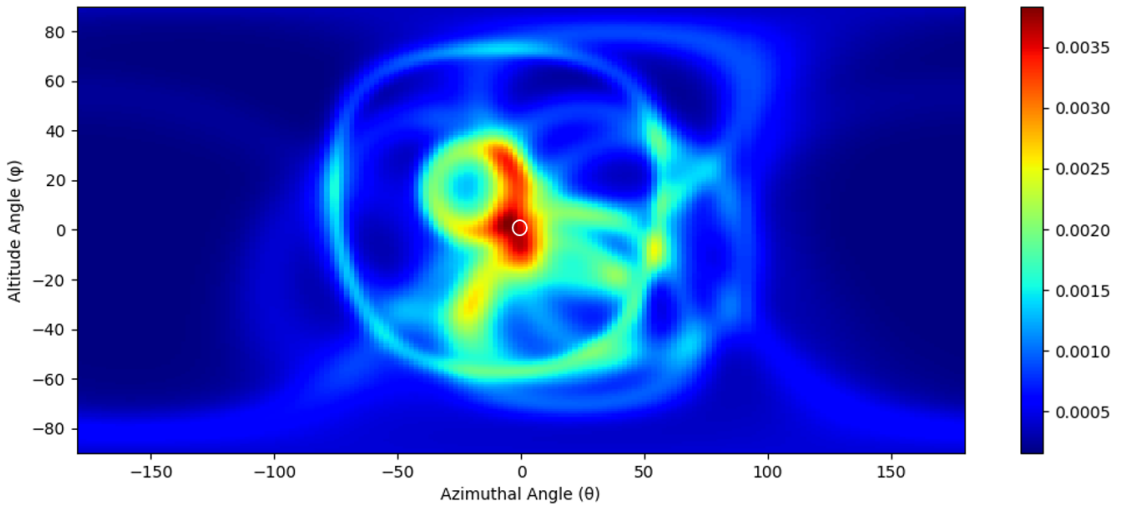

Figure 7.7: Simulated SBP image of a 1.61×10^6 $\frac{fis}{s}$ ^{252}Cf source measured at a distance of 1 m at an angular location of (0^o,0^o) for 1.07 seconds. The image is composed of 20 cone projections.

An F1 tally was set on a plane in front of the 64 pillars of stilbene that covered the face of the active area to determine the number of neutrons incident on the

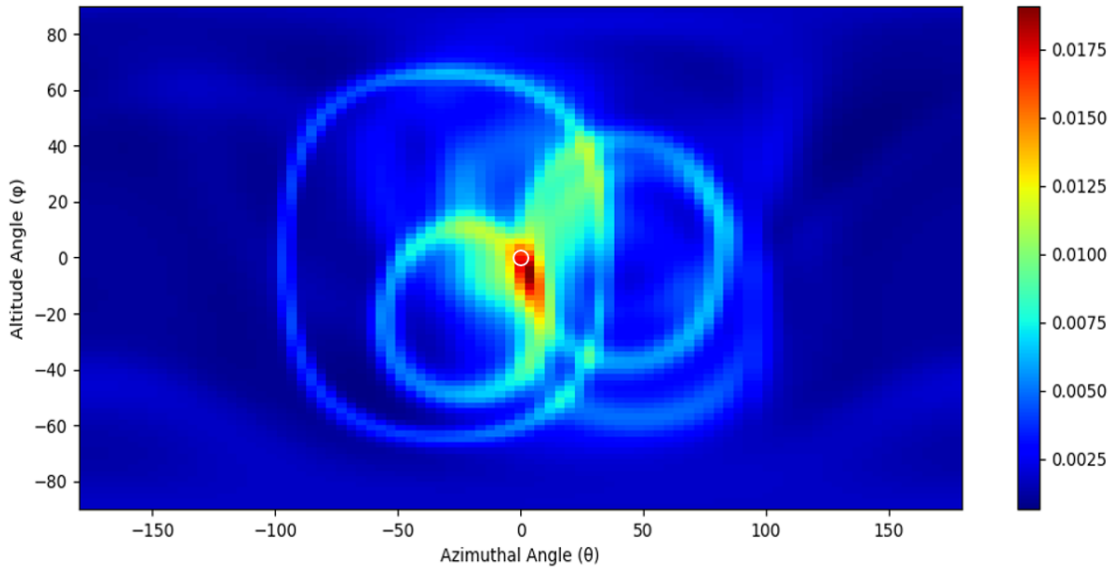

Figure 7.8: Simulated SBP image of a 1.61×10^{6} $\frac{fis}{s}$ ^{252}Cf source measured at a distance of 61 m at an angular location of (0^{o},0^{o}) for 103.8 minutes. The image is composed of 20 cone projections.

system. Using this tally along with the number of cone projections making up Figure 7.6, it was determined that a fully populated system would have a neutron intrinsic imaging efficiency for a Watt spectrum of 1.25%. This efficiency and the images shown in Figures 7.6 and 7.8 were generated assuming the crystal orientation along the source direction was in the L_a crystal plane. If the crystals were oriented in the $L_{c'}$ direction, the intrinsic efficiency of the system would be 0.94%. This analysis demonstrates the impact of the anisotropic response on the system and shows the directional dependence of a fully-realized system. This effect, however, could be mitigated by alternating crystal directions for every adjacent crystal, which would yield a more uniform directional response.

7.2 Validating the Gamma-Ray Response of the H2DPI

The gamma-ray response of the H2DPI was validated using the same geometries specified for the neutron validation but was matched to a simulated response from

an 88.6 μCi ^{137}Cs source measured at a distance of 58.42 cm from the center of the H2DPI. A photograph of the measurement setup that was used to match experimental results to simulated responses is shown in Figure 7.9.

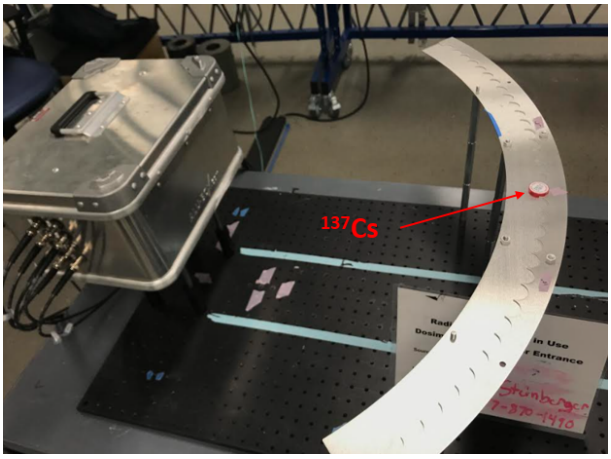

Figure 7.9: Photograph of the experimental setup used to measure an 88.6 μCi ^{137}Cs source 58.42 cm from the center of the H2DPI. The source was centered in both the azimuthal and altitude directions.

7.2.1 Simulating Gamma-Ray Pulses

Collision files were generated using MCNPX-PoliMi and converted to simulated pulses in a similar manner as described in Section 7.1.1. Three primary differences were considered for the simulated gamma-ray pulses. Energy deposition to light output was converted in a 1-1 ratio, only gamma-ray interactions were considered when generating the pulses and broadening was performed for both the stilbene pillars and $CeBr_3$ cylinders with their respective measured GEB factors. Events were projected from the centers of the $CeBr_3$ cylinders and the same light-output weighting as described in Section 7.1.1 was applied to determine the time of interaction and Z position within the stilbene pillars. The sequencing of events was also assumed that the first interaction occurred within a stilbene pillar and the second interaction occurred within a $CeBr_3$ cylinder. Unlike the neutron analysis, only an upper time difference threshold was applied to the data set of 100 ns.

7.2.2 Simulating Gamma-Ray Spectra

7.2.2.1 Simulating the Gamma-Ray Response of Stilbene Bars

Applying the methodology described in Section 7.2.1 to the collision file yielded the simulated response shown as an orange-dotted line in Figure 7.10. The experimental response shown as a solid-blue line does not agree with the simulated response and the simulated response significantly over predicts the magnitude of the Compton edge by 19.89±1.36 %.

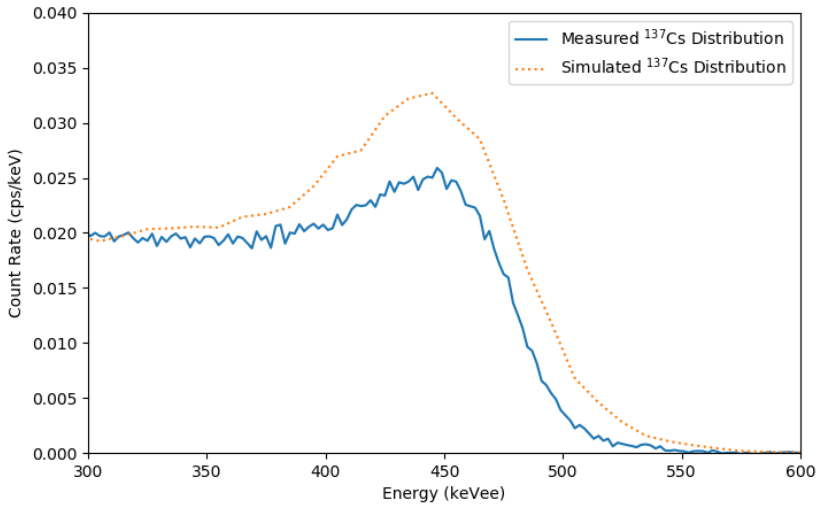

Figure 7.10: Comparison between the simulated response of a stilbene pillar to a ^{137}Cs source with the measured experimental response.

The range of electrons with energies in the hundreds of keV in organic materials is on the order of millimeters [57]. The cross sectional area of one of the stilbene pillars is 6×6 mm^2, which means a significant portion of the electrons have sufficient energy to escape or leak out of the stilbene pillars.

F1 tallies, a surface current tally tracking the number of electrons passing through a surface, were placed on all sides of a simulated stilbene pillar and a distributed electron source was set within the stilbene pillar. The electrons were given an energy of 477 keV to mimic backscatter gamma-ray interactions from a ^{137}Cs source. The direction of the electrons were set in the negative y direction to simulate the response

of the system to these backscatter interactions. Figure 7.11 shows the results of the F1 tallies placed on the pillar.

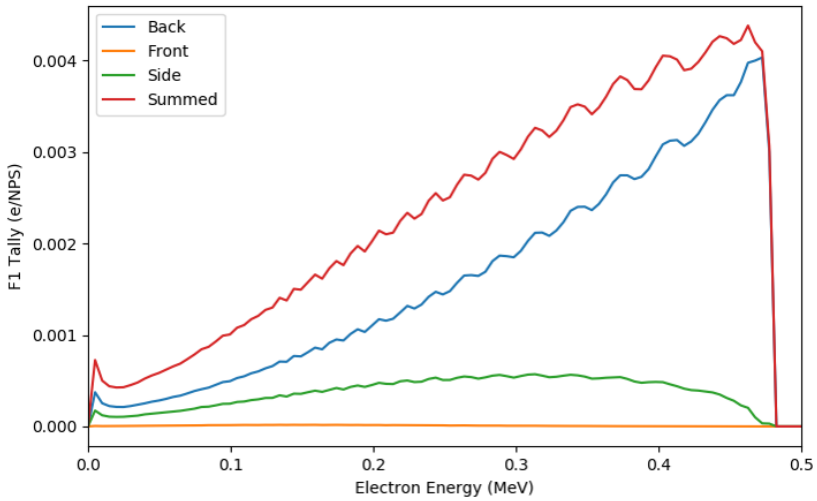

Figure 7.11: Results from an F1 tally demonstrating the electron leakage out of a stilbene pillar for a 477 keV electron.

The total probability that a 477 keV electron will escape the stilbene pillar is 23.12 %. This probability decreases as the energy of the electron decreases. Additional simulations were performed for various recoil electron energies down to a gamma-ray scattering angle of 10 degrees. The electrons were simulated in a cone at the various energies where the angle of the cone was determined based on the recoil scattering angle of the electron. The direction of the cone was set in the negative y direction to simulate the response of the ^{137}Cs source in front of the system.

Results from the various electron-escape simulations were used to further refine the simulated model. Each gamma-ray interaction was randomly sampled to determine if the recoiled electron would escape the stilbene pillar. If it was determined that the electron would escape, the escape energy of the electron was randomly sampled based on the integral-normalized summed F1 tally like the one shown in Figure 7.11. The energy deposition and light output of the interaction was then determined to be the energy deposited from the gamma-ray interaction minus the escape energy of

the electron. Applying this methodology to the simulation yields the green dot-dash line shown in Figure 7.12. This simulated spectrum better matches the measured experimental spectrum and demonstrates that the electron leakage from the stilbene pillars is non-negligible.

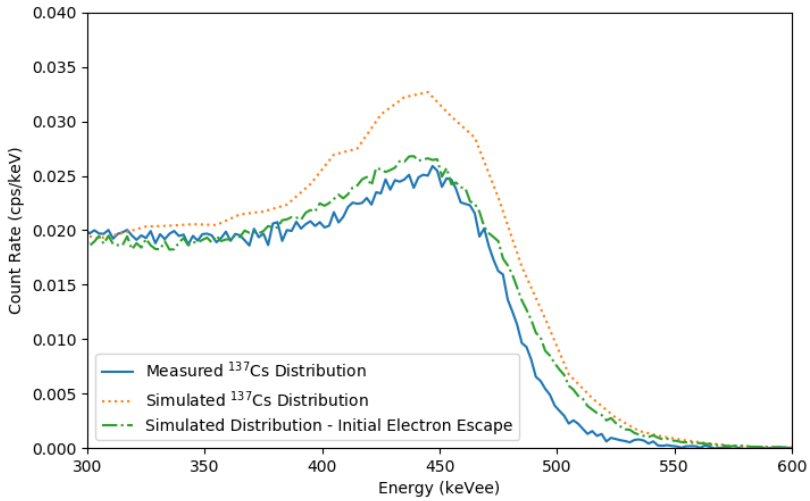

Figure 7.12: Comparison between the initial simulated response of a stilbene pillar to ^{137}Cs source with electron leakage applied to the simulation and the experimental response.

Comparing the green dot-dash line with the experimental result matches better than the initial simulation; however, there is still a 6.96±0.90 % disagreement where the simulation is over predicting the response of the stilbene pillar. This shape difference was initially thought to be caused by one of or some combination of the following three mechanisms: the escape probability of secondary scattering interactions is significantly higher than the escape probability for the initial scatter, the response of the stilbene pillar as a function of Z position is not uniform, and the average escape probability is not representative of the escape probability when broken down as a function of interaction location. Each one of these factors was assessed to determine the impact on the simulated response. It was found that the probability of secondary interactions was not significantly different than the escape probability of initial interactions. Breaking down the electron leakage to a function of position also had no

significant impact on the simulated response. It was also found that there was no significant variance in the response of the stilbene pillar as a function of Z position when comparing the measured light-output spectra from a ^{137}Cs source. Further analyzing the system response, it was determined that two additional factors were most likely responsible for the shape difference between the experimental and simulated response: the energy resolution of the experimental spectrum is much better than the simulated spectrum and a greater number of electrons were escaping the stilbene pillar than the simulated results suggest. It is well documented that there are limitations regarding the electron transport in MCNP. Specifically, limitations include boundary crossing approximations and stepsize artifacts both of which would impact the electron escape probability from the stilbene pillars [97]. Accounting for the energy resolution of the stilbene pillar and increasing the electron escape probabilities yields the spectra shown in Figure 7.13. These two adjustments show good agreement between the simulated and experimental responses; with the difference between the spectra of 1.63±0.09 %.

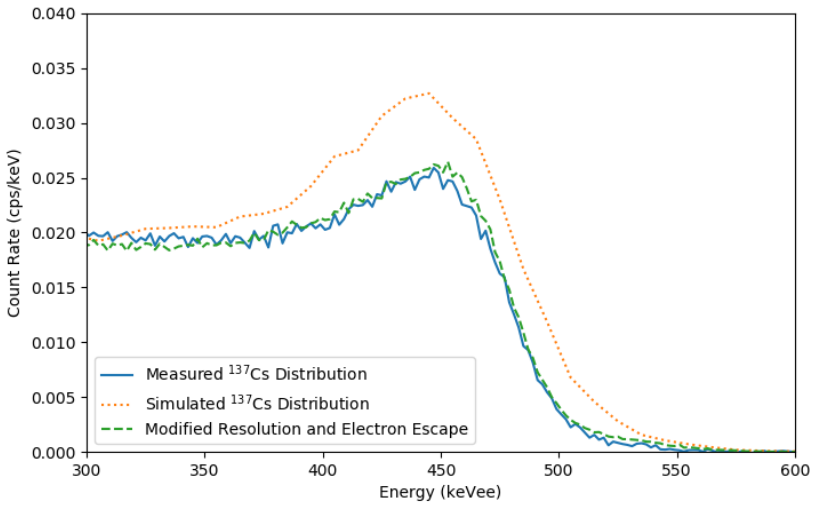

Figure 7.13: Comparison between the initial simulated response of a stilbene pillar to ^{137}Cs source with a modified energy resolution and electron leakage applied to the simulation and the experimental response.

7.2.2.2 Simulating the Gamma-Ray Response of $CeBr_3$ Cylinders

The $CeBr_3$ cylinders used in the prototype H2DPI have dimensions of (6×6Ø mm^3). Although the density and effective atomic number of $CeBr_3$ are both much higher than that of stilbene, due to the small size of the cylinders, there is still a significant probability that the electrons can escape out of the cylinders. The continuous-slowing-down approximation (CSDA) range for a 450 keV electron in $CeBr_3$ is 0.49 mm. Figure 7.14 compares the simulated spectra accounting for electron leakage and not accounting for electron leakage with the experimentally measured spectrum from a ^{137}Cs source 58.34 cm from the center of the H2DPI. Like the result with the stilbene pillars, the electron leakage is non-negligible for accurately modeling the response of the $CeBr_3$ cylinders. The measured energy resolution of the $CeBr_3$ cylinder at 661.7 keV is 4.5%.

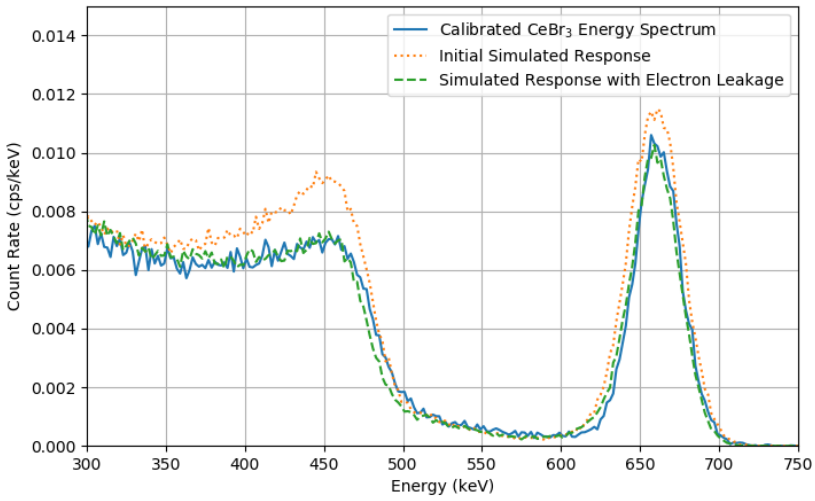

Figure 7.14: Comparison between the initial simulated response of a $CeBr_3$ Cylinder to ^{137}Cs source with simulation accounting for electron leakage and the experimental response.

7.2.2.3 Simulating Gamma-Ray Coincident Spectra

Coincident events between stilbene pillars and $CeBr_3$ cylinders were isolated both experimentally and in simulation. It was assumed in simulation that the first event

for the coincident events occurred in the stilbene pillar and the second event occurred in the $CeBr_3$ cylinder. The energy depositions for these two interactions were summed and the resulting experimental and simulated coincident energy spectra are shown in Figure 7.15. The measured energy resolution at 661.7 keV was found to be 7% for the coincident spectrum.

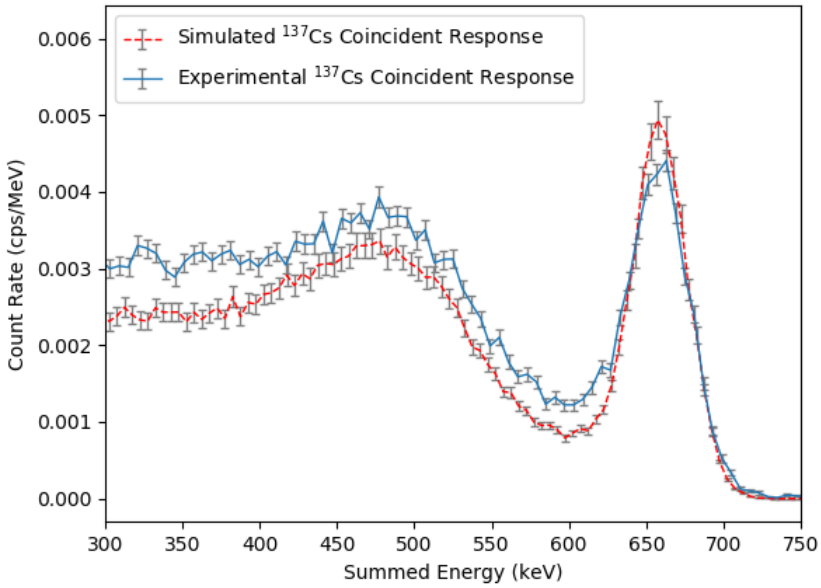

Figure 7.15: Comparison between the simulated coincident response of the prototype H2DPI to a ^{137}Cs source 58.42 cm from the center of the H2DPI.

The magnitudes of the two spectra agree well with there being a higher continuum in the experimental spectrum than in simulation. The simulated summed photopeak (energy range of 627-700 keV) slightly over predicts the magnitude of the summed photopeak by 3.17±1.88 %. The continuum is under predicted by 14.10±0.67 % in simulation. There are two likely causes responsible for the difference in the continuum. First, wiring and BNC bulkheads were not modeled in the simulation. Both of these components can cause additional scattering that would add to the continuum. The second effect could be electron cross talk between the stilbene pillars. Gamma rays that undergo high-angle Compton scattering will escape the stilbene pillars and potentially interact with other stilbene pillars. The CSDA range of a 450 keV electron

in air is 140 cm and the CSDA range of a 450 keV electron in teflon is 1.52 mm. The stilbene pillars are not wrapped in that thick of teflon, which means that electrons could escape from one pillar and potentially interact with another pillar.

7.2.3 Simulating a Fully-Populated Stilbene and $CeBr_3$ H2DPI

Incorporation of $CeBr_3$ scintillators within a fully-populated system would allow for improved gamma-ray spectroscopic capabilities and Compton imaging without the need for approximating the energy of incident gamma rays to reconstruct coincident events. To demonstrate the capability of a fully populated system containing $CeBr_3$, a simulation model was made with four cylindrical pillars of $CeBr_3$ ($50.5\times6\text{Ø}$ mm^3) placed one pixel in from each corner of the system. An image of the active volume of this simulation is shown in Figure 7.16.

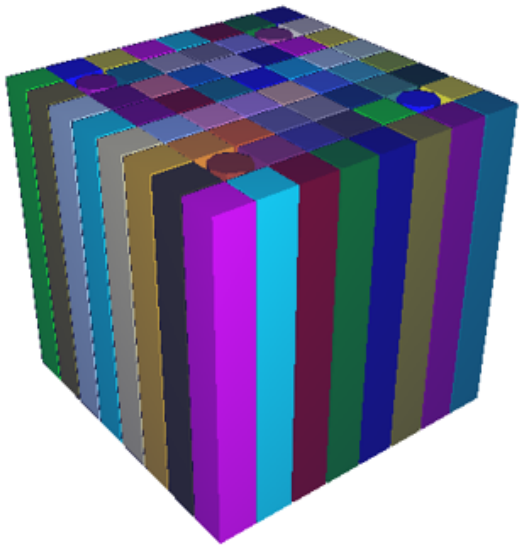

Figure 7.16: 3D rendering of the scintillators in the fully populated H2DPI using Vised. The pillars are stilbene ($6\times6\times50.5$ mm^3) and the cylindrical pillars are $CeBr_3$ ($50.5\times6\text{Ø}$ mm^3).

The following two simulations were performed using this system: simulation of an 88.6 μCi ^{137}Cs source at 1 m and simulation of the BeRP ball at 5 m. The methodology detailed in Sections 7.2.2.1-7.2.2.3 were applied to the data set. It was

assumed that the Z position reconstruction for the $CeBr_3$ was the same as for the average stilbene pillar and that the energy resolution of the $CeBr_3$ cylindrical pillars was the same as the ($6\times6\varnothing$ mm^3) cylinders.

Figure 7.17 shows the simulated coincident spectrum from an 88.6 μCi ^{137}Cs source at 1 m for a simulated measurement time of 59.9 minutes. The projection bounds shown in Figure 7.17 were used to define the imaging region that was used to generate the SBP image shown in Figure 7.18. This image is composed of 7404 cone projections; giving this fully-populated system an intrinsic gamma-ray imaging efficiency of 0.31 % for the defined energy range of 661.7±37.56 keV. The energy range was defined as plus or minus two standard deviations based on the summed-coincident spectrum resolution of 7% at 661.7 keV.

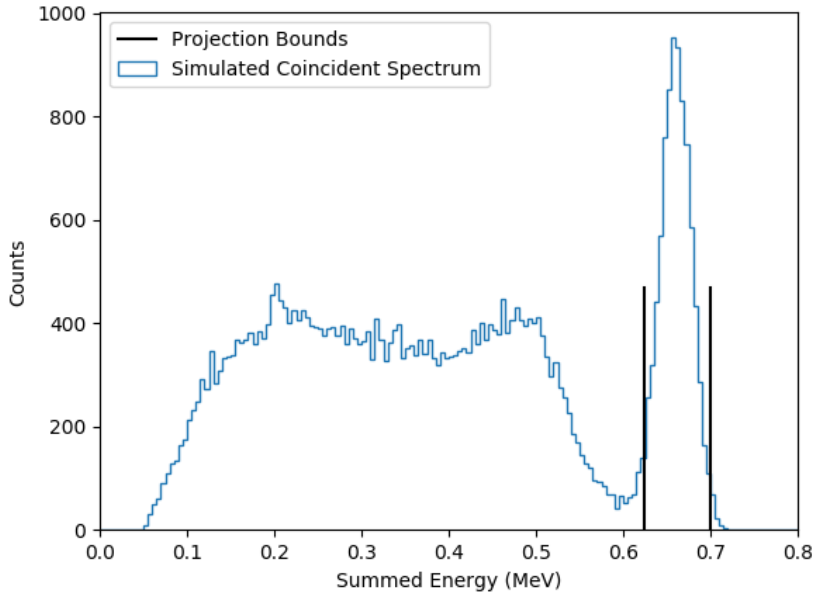

Figure 7.17: Simulated summed-coincident spectrum for an 88.6 μCi ^{137}Cs source at 1 m using the fully-populated H2DPI. The simulated measurement time is 59.9 minutes.

Simulating and imaging a mono-energetic source like ^{137}Cs can yield a good basis for imaging capabilities, however, the resulting spectrum and image do not demonstrate the capabilities of the system when a more complex spectrum is present. To

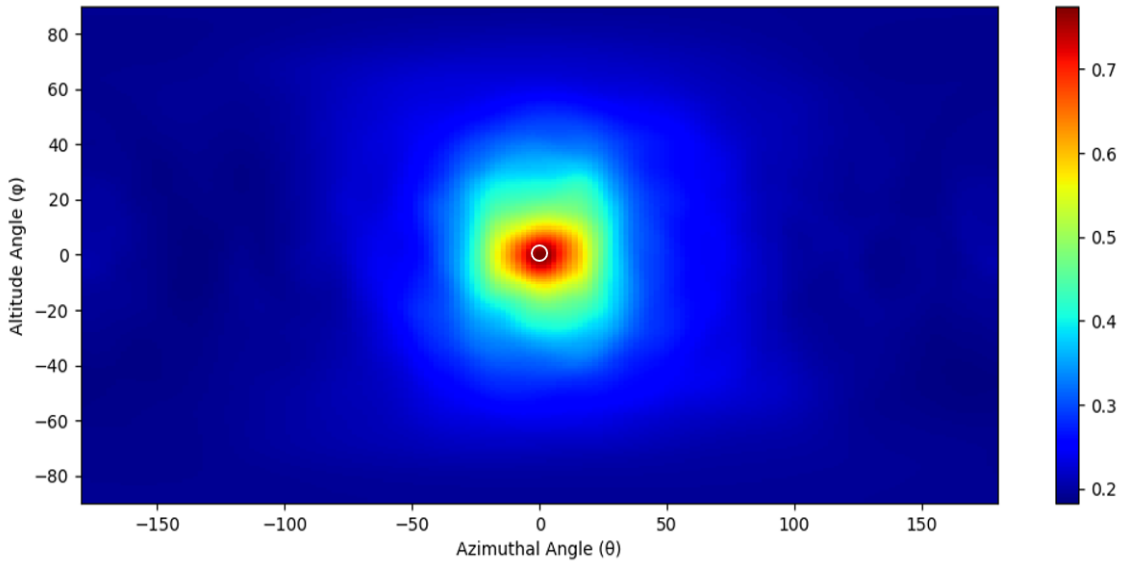

Figure 7.18: SBP image of an 88.6 μCi ^{137}Cs source at 1 m at an angular location of (0^o,0^o) generated using the events within the projection bounds shown in Figure 7.17.

further test the capabilities of the fully-populated H2DPI, the BeRP ball was simulated at 5 m from the center of the H2DPI. An initial source isotopic composition was assumed [63] with the following three assumptions to reduce computational time: only gamma rays with intensities greater than 3.7×10^4 $\frac{\gamma}{s}$ were included in the simulation, x-rays were not included in the simulation and only the exterior two centimeters of the BeRP ball were simulated. Figure 7.19 shows the resulting summed-coincident spectrum for a simulated measurement time of 27.9 minutes. Imaging the region of 0.3-0.5 MeV shown within the projection bounds in Figure 7.19 for 2.4 minutes yields the SBP image composed of 50 cone projections shown in Figure 7.20.

The neutron response of the fully-populated H2DPI was also simulated using the BeRP ball. Spontaneous fissioning of ^{238}Pu, ^{240}Pu and ^{242}Pu were simulated in the BeRP ball using MCNPX-PoliMi given an initial isotopic concentration of the BeRP ball [63]. The neutron flux emitted by the BeRP ball was estimated to be 8.4×10^5 $\frac{n}{s}$. Figure 7.21 shows the resulting SBP image of 50 cone projections acquired in a

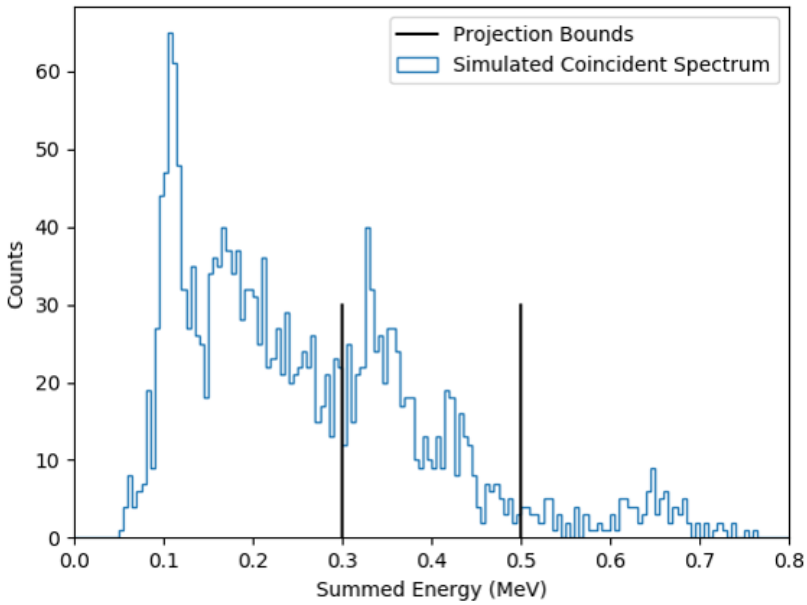

Figure 7.19: Simulated summed-coincident spectrum for the BeRP ball at 5 m using the fully-populated H2DPI. This simulation corresponds to a measurement time of 27.9 minutes

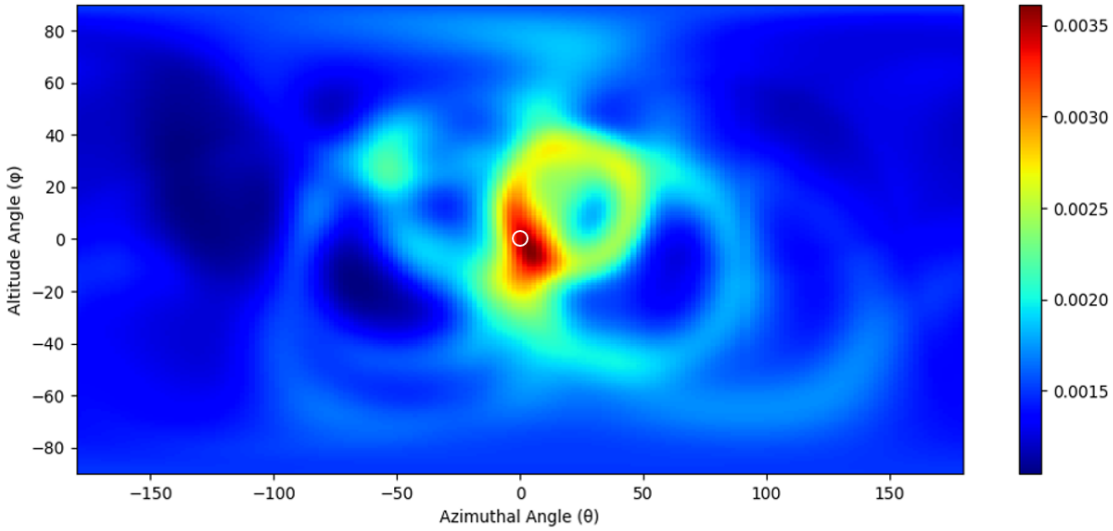

Figure 7.20: SBP image composed of 50 cone projections of the BeRP ball at 5 m at an angular location of (0^o,0^o) generated using the events within the projection bounds shown in Figure 7.19.

simulated time of 10 minutes. Incorporation of the four $CeBr_3$ pillars does decrease the intrinsic neutron-imaging efficiency from 1.25% to 1.12%.

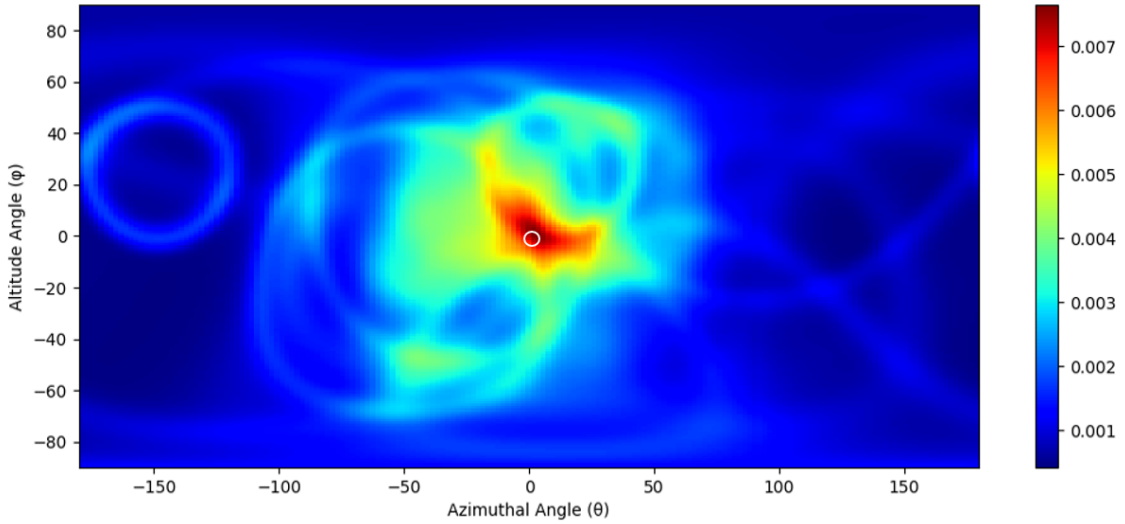

Figure 7.21: Simulated neutron SBP image of the BeRP ball at 5 m at an angular location of (0^o,0^o) composed of 50 cone projections acquired in a corresponding measurement time of 10 minutes.

7.3 Conclusions

A substantial amount of research has focused on determining the intrinsic efficiency of a NSC composed of pillars of organic scintillators coupled to photodetectors. Ruch et al. estimated an intrinsic neutron-imaging efficiency for a Watt spectrum to be 0.66% for a stilbene-based imaging system [53]. Weinfurther et al. estimated about a 10% intrinsic neutron-imaging efficiency for events above 200 keV threshold for a Watt spectrum using a system composed of EJ-204 pillars ($1\times1\times20$ cm^3) coupled to MCP-PMTs [44]. The efficiency reported by Weinfurther et al., however, was simulated for a pencil beam of fission spectrum neutrons incident on the center of the detector. This efficiency is then not directly comparable to the results presented in this work or obtained by Ruch. A prototype optically segmented single volume NSC composed of EJ-204 coupled to SensL J-series SiPMs has been built and is being tested. The intrinsic neutron-imaging efficiency, however, has not yet been published [98].

This research presents the first validated simulation model used to estimate the intrinsic neutron imaging efficiency of a NSC composed of optically-segmented pillars of organic scintillator coupled to SiPMs. The intrinsic neutron efficiency for a stilbene-based NSC composed of pillars ($6 \times 6 \times 50.5$ mm^3) was determined to be 0.94 to 1.25 % depending on the orientation of the stilbene crystals. The following thresholds were set to obtain these intrinsic efficiencies: 50-1500 keV light-output range, 217-8825 ps time difference range and neutron removal probability corresponding to a 0.1% gamma-ray misclassification rate. This intrinsic efficiency range is higher than what was predicted by Ruch et al. [53] and much lower than what was predicted by Weinfurther et al. [44].

By replacing four of the stilbene pillars with pillars of $CeBr_3$ where each pillar is surrounded by pixels coupled to stilbene and are placed symmetrically in the system, accurate Compton imaging can be achieved. Results presented estimate a gamma-ray imaging efficiency of 0.31% for gamma-rays emitted by ^{137}Cs. The incorporation of inorganic scintillators allows for an additional accurate imaging mode. Compton imaging of the BeRP ball can be achieved in 2.4 minutes with the source at 5 m with a minor impact on the intrinsic neutron imaging efficiency; where the efficiency is reduced from 1.25% to 1.12%.

CHAPTER VIII

Conclusions and Future Work

8.1 Conclusions

National security missions require versatile detector systems to be able to detect SNM under a wide range of conditions, including complex shielding scenarios. In these cases, any information that can be acquired from a source can be useful to detect and localize it. For instance, being able to detect and image both gamma rays and fast neutrons allows for multiple methods to determine the location and verify a source of plutonium.

A prototype H2DPI composed of eight stilbene pillars coupled to SensL C-series SiPMs successfully imaged the neutrons and gamma-rays emitted by the BeRP ball; a 4.5 kg sphere of WGPu. Comparing the gamma-ray images to the neutron images for this initial system shows that there are significantly more artifacts in the gamma-ray images. These artifacts are most likely due to a combination of incorrect sequencing and incorrect determination of the incident energy of the gamma ray. This eight-pillar prototype, however, proved that a compact imaging system could image kilogram-quantities of SNM.

Inorganic scintillators were thoroughly tested and incorporated into the design to allow for Compton imaging of gamma rays without the need to assume the energy or sequencing by timing. The two inorganic scintillators that yielded the best energy

resolution and highest photopeak efficiency were $CeBr_3$ and LYSO(Ce) respectively.

Miniaturized imaging systems were built composed of each scintillator and stilbene cubes to test the imaging response with the incorporated scintillators. Results showed a signal to background ratio for the $CeBr_3$ of 131±40 compared to the value of 1.80±0.22 found with the LYSO(Ce) system. LYSO(Ce), while more efficient, contains ^{176}Lu that produces an irreducible background in Compton imaging. This non-negligible background increases the minimal detectable activity of a source and could result in imaging artifacts that overshadow a true source location. This result was then used to design a sixteen-pillar iteration of the H2DPI composed of stilbene pillars and $CeBr_3$ cylinders coupled to SensL J-series SiPMs. The placement of the $CeBr_3$ cylinders was optimized using a structural similarity technique and the optimized configuration was built and characterized.

Incorporation of $CeBr_3$ scintillators into the 16-pillar prototype H2DPI greatly improved spectroscopic capabilities and Compton imaging performance relative to the previous iteration of the H2DPI. The 16-pillar H2DPI accurately localized a mock HEU source and a plutonium disk when both sources were in the same field of view. This result also demonstrates the improvement in Compton imaging methodology; most Compton imaging systems cannot image the 185.7 keV gamma ray emitted by ^{235}U due to uncertainty in sequencing of events. The H2DPI does not have this limitation because of the assumed sequencing for the combination of inorganic and organic scintillators. In addition, the H2DPI is a neutron spectrometer that is capable of isolating and identifying the (α,n) from a PuBe source from the Watt spectrum from a ^{252}Cf source.

Accurate characterization is paramount for source isolation, identification and accurately simulating the system response. Of particular note, the anisotropic response of stilbene has a particularly high impact on the simulated system response, while not having a substantial impact on experimental imaging performance. The reason

the anisotropic response significantly impacts simulations is because it shifts the light output for events either making them above or below a defined threshold. This effect can greatly shift the simulated efficiency since the anisotropic response causes a 30-35 % difference in light output between the L_a and $L_{c'}$ crystal planes. Experimentally, since these events already occurred above a threshold and have already been recorded, the reconstruction only impacts the value of the energy deposited. Uncertainty for the system is then dominated by the TOF of the neutrons, which makes the relative change in the energy deposition negligible.

Validated simulation models were applied to a fully-populated H2DPI composed of 64 stilbene pillars ($6 \times 6 \times 50.5$ mm^3). The intrinsic neutron efficiency for this system was determined to be 0.94 to 1.25 % depending on the orientation of the stilbene crystals. This is the first validated simulation model used to estimate the intrinsic neutron imaging efficiency of a NSC composed of optically-segmented pillars of organic scintillator coupled to SiPMs. Comparing to previous work, the intrinsic efficiency range is higher than what was predicted by Ruch et al. [53] and much lower than what was predicted by Weinfurther et al. [44].

Accurate Compton imaging can be achieved with a 64-pillar system by replacing four of the stilbene pillars with pillars of $CeBr_3$, where each pillar is surrounded by pixels coupled to stilbene and are placed symmetrically in the system. Results presented estimate a gamma-ray imaging efficiency of 0.31% for gamma-rays emitted by ^{137}Cs. The incorporation of inorganic scintillators allows for an additional accurate imaging mode. Compton imaging of a source like the BeRP ball can be achieved in 2.4 minutes with the source at 5 m with a minor impact on the intrinsic neutron imaging efficiency.

8.2 Future Work

Three key areas exist to further improve the development of compact scatter-based imaging systems such as the H2DPI.

The first area is with regards to the gamma-ray simulations. MCNP under predicted the electron leakage from the scintillators when modeling the system response. This under prediction is due to inaccuracies in the electron transport model. While this effect was accounted for in simulation, this adds a level of uncertainty into the analysis. Simulating the electron leakage using Geant4 or other codes that are more refined to transport charged particles may yield more accurate results and allow for improved modeling of the system response.

The second area for improvement is with regards to the type of scintillator and geometry of scintillator used for this research. Cylinders of $CeBr_3$ with dimensions of (6×6 Ø mm^3) were incorporated into the design due to manufacturing limitations on the tolerance of the length of the pillars of $CeBr_3$ that were acquired. A next step in this design process would be to incorporate full pillars of $CeBr_3$ that are within length tolerance and validate the system response with the incorporation of those pillars. In addition, alternative organic scintillators could be tested such as organic glass. Organic glass is an inexpensive PSD capable organic scintillator that has shown to have higher light output and better time resolution than stilbene. This scintillator could be an excellent candidate for use in a fully-realized system.

Finally, the electronics must be realized to field a compact system. This work made advancements towards a compact dual-particle imaging system, but without consideration for the electronics. The active volume of the H2DPI is portable and compact, but the v1730 digitizers, low-voltage power supply and data acquisition system make it so the system is not easily portable. The digitizers could be converted to an on-board field-programmable gate array to process the data without the need for digitizing and storing the raw data, and the low-voltage power supply could be

converted into a battery system. Both of these changes would make the system significantly more compact and easier to transport.

BIBLIOGRAPHY

[1] Nathan P. Giha et al. Readout electronics of a handheld dual particle imager. *IEEE Nuclear Science Symposium, Atlanta, Georgia*, 2015.

[2] Robert A. Weldon et al. Characterization of stilbene's scintillation anisotropy for recoil protons between 0.56 and 10 mev. *Nuclear Instruments and Methods in Physics Research Section A*, 2020.

[3] Gomez W. Wright. Correct uranium sealed source reference documentation for radiological signature training devices. *Oak Ridge National Laboratory*, 2014.

[4] C. L. Painter D. S. Coffey. Certificate of conformance, pacific northwest national laboratory. *Pu Sealed Source Project, Design Drawing H-3-310767*, 2013.

[5] Otto R. Frisch and John A. Wheeler. The discovery of fission. 1967.

[6] Treaty on the non-proliferation of nuclear weapons. 1970.

[7] Treaty between the united states of america and the russian federation on measures for the further reduction and limitation of strategic offensive arms. 2010.

[8] International Atomic Energy Agency. Iaea safeguards glossary. 2001.

[9] Los Alamos National Laboratory A. GAVRON. Nondestructive assay techniques applied to nuclear materials.

[10] Mehrdad Gholami Daryoush Shahbazi-Gahrouei and Samaneh Setayandeh. A review on natural background radiation. *Advanced Biomedical Research*, 2:65, 2013.

[11] Y.-F. Wang et al. Predicting neutron production from cosmic-ray muons. *Phys. Rev. D*, 64:013012, 2001.

[12] T. Douglas Reilly. 11. useful nuclear data for nda.

[13] S. Majety J. Y. Lin H. X. Jiang J. Li, R. Dahal. Hexagonal boron nitride epitaxial layers as neutron detector materials. *Nuclear Instruments and Methods in Physics Research Section A: Accelerators, Spectrometers, Detectors and Associated Equipment*, 2011.

[14] K C Huang N LiCausi R Dahal J J Q Lu Y Danon, J Clinton and I Bhat. Towards high efficiency solid-state thermal and fast neutron detectors. *Journal of Instrumentation*, 2012.

[15] N. Zaitseva et al. Scintillation properties of solution-grown trans-stilbene single crystals. *Nuclear Instruments and Methods in Physics Research Section A*, 789:8–15, 2015.

[16] N. Zaitseva et al. Recent developments in plastic scintillators with pulse shape discrimination. *Nuclear Instruments and Methods in Physics Research Section A*, 889:97–104, 2018.

[17] P. L. Feng J. S. Carlson. Melt-cast organic glasses as high-efficiency fast neutron scintillators. *Nuclear Instruments and Methods in Physics Research Section A: Accelerators, Spectrometers, Detectors and Associated Equipment*, 2016.

[18] T. A. Laplace et al. Comparative scintillation performance of ej-309, ej-276, and a novel organic glass. *Journal of Instrumentation*, 2020.

[19] F.D. Brooks et al. Development of organic scintillators. *Nucl. Instrum. Methods*, 162:477–505, 1979.

[20] V. V. Verbinski et al. The response of some organic scintillators to fast neutrons. *J. Greenborg (Ed.), Proc. Spec. Sess. Fast Neutron Spectrosc., American Nuclear Society, San Francisco, CA*, 1964.

[21] F.D. Brooks. A scintillation counter with neutron and gamma-ray discriminators. *NUCLEAR INSTRUMENTS AND METHODS 4*, 1959.

[22] D. Ress et al. Neutron imaging of inertial confinement fusion targets at nova. *Review of Scientific Instruments*, 59, 1998.

[23] P. A. Hausladen et al. Fast-neutron coded-aperture imaging of special nuclear material configurations. *53rd INMM Annual Meeting,Orlando, Fla.*, 2012.

[24] Peter Marleau et al. Time encoded fast neutron/gamma imager for large standoff snm detection. *2011 IEEE Nuclear Science Symposium Conference Record*, 2011.

[25] N. Mascarenhas et al. Development of a neutron scatter camera for fission neutrons. *IEEE Nuclear Science Symposium Conference Record*, 2(2):185–188, 2006.

[26] James M. Ryan et al. Development and performance of the fast neutron imaging telescope for snm detection. *Optics and Photonics in Global Homeland Security IV*, 2008.

[27] Mark D. Gerling et al. Miner - a mobile imager of neutrons for emergency responders. *2014 IEEE Nuclear Science Symposium and Medical Imaging Conference (NSS/MIC)*, pages 1–4, 2015.

[28] Alexis Poitrasson-Rivière. Dual-particle imaging system based on simultaneous detection of photon and neutron collision events. *Nuclear Instruments and Methods in Physics Research Section A*, 760:40–45, 2014.

[29] L.Tagawa et al. Development of novel neutron camera to estimate secondary particle dose for safe proton therapy. *Nuclear Instruments and Methods in Physics Research Section A*, 2018.

[30] Jason S. Legere et al. A field deployable imaging neutron detector (find) for snm. *IEEE Nuclear Science Symposium Conference Poster*, 2015.

[31] Amanda C. Madden et al. An imaging neutron/gamma-ray spectrometer. *Chemical, Biological, Radiological, Nuclear, and Explosives (CBRNE) Sensing XIV,*, 2013.

[32] Marc L. Ruch. *Silicon Photomultipliers for Compact Neutron Scatter Cameras*. PhD thesis, Department of Nuclear Engineering and Radiological Sciences in the University of Michigan, 2017.

[33] M.C.Hamel et al. Localization and spectral isolation of special nuclear material using stochastic image reconstruction. *Nuclear Instruments and Methods in Physics Research Section A*, 841, 2017.

[34] John Kyle Polack. *A Maximum-Likelihood Approach for Localizing and Characterizing Special Nuclear Material with a Dual-Particle Imager*. PhD thesis, Department of Nuclear Engineering and Radiological Sciences in the University of Michigan, 2016.

[35] R. W. Todd et al. A proposed γ camera. *Nature*, 1974.

[36] G. W. Phillips. Applications of compton imaging in nuclear waste characterization and treaty verification. *Nuclear Science Symposium Conference Record, IEEE*, 1997.

[37] Y. Du et al. Evaluation of a compton scattering camera using 3-d position

sensitive cdznte detectors. *Nuclear Instruments and Methods in Physics Research Section A*, 457, 2001.

[38] Kenneth L. Matthews et al. An electronically-collimated portable gamma-ray detector for locating environmental radiation sources. *Proc. SPIE 6319, Hard X-Ray and Gamma-Ray Detector Physics and Penetrating Radiation Systems VIII*, 63190H, 2006.

[39] A. Poitrasson-Rivière et al. Angular-resolution and material-characterization measurements for a dual-particle imaging system with mixed-oxide fuel. *Nuclear Instruments and Methods in Physics Research Section A*, 797, 2015.

[40] J. K. Polack et al. Spectrum isolation in multi-source image reconstruction using a dual-particle imager.

[41] D.J. Herbert et al. Study of sipm as a potential photodetector for scintillator readout. *Nuclear Instruments and Methods in Physics Research Section A*, 567:356–359, 2006.

[42] M. L. Ruch et al. Pulse shape discrimination performance of stilbene coupled to low-noise silicon photomultipliers. *Nuclear Instruments and Methods in Physics Research Section A*, 793, 2015.

[43] M. L. Ruch et al. Time resolution of stilbene coupled to silicon photomultipliers for use in a handheld dual particle scatter camera. *IEEE Nucl. Sci. Symp. Conf., San Diego, CA*, pages 1–3, 2015.

[44] Kyle Weinfurther et al. Model-based design evaluation of a compact, high-efficiency neutron scatter camera. *Nuclear Instruments and Methods in Physics Research Section A*, 2018.

[45] M. Sweany et al. Interaction position, time, and energy resolution in organic scintillator bars with dual-ended readout. *Nuclear Instruments and Methods in Physics Research Section A*, 927:451–462, 2019.

[46] Joshua Braverman et al. Single-volume neutron scatter camera for high-efficiency neutron imaging and spectroscopy. *Preprint submitted to Nuclear Instruments and Methods in Physics A*, 2018.

[47] Marc A. Wonders et al. Characterization of a mixed-sinusoid multiplexing scheme with silicon photomultipliers and an inorganic scintillator. *Nuclear Instruments and Methods in Physics Research Section A*, 959, 2020.

[48] Juan J. Manfredi et al. The single-volume scatter camera. *SPIE Optical Engineering + Applications*, Proceedings Volume 11494, Hard X-Ray, Gamma-Ray, and Neutron Detector Physics XXII, 2020.

[49] William M. Steinberger et al. Imaging special nuclear material using a handheld dual particle imager. *Scientific Reports*, 10:1–11, 2020.

[50] William M. Steinberger et al. Optimizing the position of inorganic scintillators in a handheld dual particle imager. *2020 IEEE Nuclear Science Symposium and Medical Imaging Conference (NSS/MIC)*, 2020.

[51] William M. Steinberger et al. Anisotropic neutron response of trans-stilbene and impact on a handheld dual particle imager. *Nuclear Instruments and Methods in Physics Research Section A*, 1003, 2021.

[52] M. L. Ruch et al. Position sensitivity within a bar of stilbene coupled to silicon photomultipliers. *IEEE Nuclear Science Symposium, Strasbourg, France*, 2016.

[53] M. L. Ruch et al. Proof of principle simulation of a handheld neutron scatter camera. *Adv. Nucl. Nonproliferation Technol. Policy Conf*, pages 1–25, 2016.

[54] SensL. Silicon Photomultiplier (SiPM) 4-Side Scaleable Arrays. *Datasheet, 2018, https://www.onsemi.com/pdf/datasheet/arrayc-series-d.pdf.*

[55] ELJEN Technology. Silicone rubber optical interface ej-560. *Datasheet, 2018.*

[56] Daniel Shy et al. Gamma-ray tracking for high energy gamma-ray imaging in pixelated CdZnTe. *Nuclear Instruments and Methods in Physics Research Section A*, 2018.

[57] Glenn F. Knoll. *Radiation Detection and Measurement, 4th Edition.* 2010.

[58] J.B. BIRKS. The theory and practice of scintillation counting. *A volume in International Series of Monographs in Electronics and Instrumentation*, 1964.

[59] Andreas Enqvist et al. Neutron light output response and resolution functions in ej-309 liquid scintillation detectors. *Nuclear Instruments and Methods in Physics Research Section A*, 715:79–86, 2013.

[60] H. H. Barrett et al. List-mode likelihood. *Journal of the Optical Society of America A*, 14:2914, 1997.

[61] S. Wilderman et al. Improved modeling of system response in list mode EM reconstruction of Compton scatter camera images. *IEEE Transactions on Nuclear Science*, 48:111–116, 2001.

[62] S. Pozzi et al. Mcnpx-polimi for nuclear nonproliferation applications. *Nuclear Instruments and Methods in Physics Research Section A*, 694:119–125, 2012.

[63] John Mattingly. Polyethylene-reflected plutonium metal sphere: Subcritical neutron and gamma measurements. *SANDIA REPORT, Sandia National Laboratories*, 2009.

[64] David Loaiza. Neptunium-237 sphere surrounded by hemispherical shells of highly enriched uranium. *Los Alamos National Laboratory*, VII, 2009.

[65] Alex McSpaden et al. Fy2018 preparation for the neso subcritical experiment. *Los Alamos National Laboratory*, 2019.

[66] Shawn R. Tornga et al. Three-dimensional compton imaging using list-mode maximum likelihood expectation maximization. *IEEE Transactions on Nuclear Science*, 56, 2009.

[67] M. Kolstein et al. Evaluation of list-mode ordered subset expectation maximization image reconstruction for pixelated solid-state compton gamma camera with large number of channels. *Journal of Instrumentation*, 9, 2014.

[68] SensL. J-Series High PDE and Timing Resolution, TSV Package. *Datasheet, 2015, http://sensl.com/downloads/ds/DS-MicroJseries.pdf.*

[69] Zhou Wang et al. Image quality assessment: from error visibility to structural similarity. *IEEE Transactions on Image Processing*, 13, 2004.

[70] A. Hore and D. Ziou. Image quality metrics: Psnr vs. ssim. *IEEE Int. Conf. on Pattern Recognition*, 2010.

[71] R. Kumar and M. Rattan. Analysis of various quality metrics for medical image processing. *International Journal of Advanced Research in Computer Science and Software Engineering*, 2, 2012.

[72] A. Hore and D. Ziou. Vmaf reproducibility: Validating a perceptual practical video quality metric. *2017 IEEE International Symposium on Broadband Multimedia Systems and Broadcasting (BMSB)*, 2017.

[73] Marta et al., Orduna. Video multimethod assessment fusion (vmaf) on 360vr contents. *IEEE Trans. Consumer Electronics*, 66, 2020.

[74] J. G. Ok G. Kim H. S. Kim, M. Na and S. Ye. Development of the hemispherical

rotational modulation collimator imaging system. *IEEE Transactions on Nuclear Science*, 2019.

[75] Seoryeong et al., Park. Impact of aperture-thickness on the real-time imaging characteristics of coded-aperture gamma cameras. *Nuclear Engineering and Technology*, 2020.

[76] T. A. Laplace et al. Scintillator light yield measurements with waveform digitizers. *Nuclear Instruments and Methods in Physics Research Section A*, 2020.

[77] Mark A. Norsworthy et al. Evaluation of neutron light output response functions in ej-309 organic scintillators. *Nuclear Instruments and Methods in Physics Research Section A*, 842:20–27, 2017.

[78] M. A. Nelson et al. Analysis of digital timing methods with BaF_2 scintillators. *Nuclear Instruments and Methods in Physics Research Section A*, 505:324–327, 2003.

[79] W. M. Steinberger et al. Timing performance of organic scintillators coupled to silicon photomultipliers. *Nucl. Instruments Methods Phys. Res. Sect. A Accel. Spectrometers, Detect. Assoc. Equip*, 922:185–192, 2019.

[80] L. F. Miller et al. Digital pulse shape discrimination. *Radiation Protection Dosimetry*, 126:253–255, 2007.

[81] M. Flaska et al. Identification of shielded neutron sources with the liquid scintillator bc-501a using a digital pulse shape discrimination method. *Nuclear Instruments and Methods in Physics Research Section A*, 577:654–663, 2007.

[82] D. Cester et al. Pulse shape discrimination with fast digitizers. *Nuclear Instruments and Methods in Physics Research Section A*, 748:33–38, 2014.

[83] N. V. Kornilov et al. Total characterization of neutron detectors with a 252cf source and a new light output determination. *Nuclear Instruments and Methods in Physics Research Section A*, 599:226–233, 2009.

[84] Natalia Zaitseva et al. Plastic scintillators with efficient neutron/gamma pulse shape discrimination. *Nuclear Instruments and Methods in Physics Research Section A*, 668:88–93, 2012.

[85] K. Tsukada et al. Directional anisotropy in the characteristics of the organic-crystal scintillators, ii. *Nuclear Instruments and Methods*, 37:69–76, 1965.

[86] F. D. Brooks et al. Directional anisotropy in organic scintillation crystals. *Nuclear Instruments and Methods*, 121:69–76, 1974.

[87] P. Schuster et al. Characterization of the scintillation anisotropy in crystalline stilbene scintillator detectors. *Nuclear Instruments and Methods in Physics Research Section A*, 859:95–101, 2017.

[88] R. A. Weldon Jr et al. High-precision characterization of the neutron light output of stilbene along the directions of maximum and minimum response. *Nuclear Instruments and Methods in Physics Research Section A*, 927:313–319, 2019.

[89] E. Brubaker et al. Neutron imaging using the anisotropic response of crystalline organic scintillators. *IEEE Nuclear Science Symposuim Medical Imaging Conference*, 2010.

[90] Robert A. Weldon. *Characterization of the Anisotropic Scintillation Response of Stilbene and an Application for Neutron Source Localization.* PhD thesis, Department of Nuclear Engineering at North Carolina State University, 2019.

[91] Robert A. Weldon et al. Exploiting stilbene's scintillation anisotropy for neu-

tron source localization. *Nuclear Instruments and Methods in Physics Research Section A*, 967, 2020.

[92] Andreas Enqvist et al. Calculation of the light pulse distributions induced by fast neutrons in organic scintillation detectors. *Nuclear Instruments and Methods in Physics Research Section A*, 618:266–274, 2010.

[93] T. H. Shin et al. Measured neutron light-output response for trans-stilbene and small-molecule organic glass scintillators. *Nuclear Instruments and Methods in Physics Research Section A*, 939:36–45, 2019.

[94] N. V. Kornilov et al. Total characterization of neutron detectors with a 252cf source and a new light output determination. *Nuclear Instruments and Methods in Physics Research Section A*, 599:226–233, 2009.

[95] Sara A. Pozzi et al. Monte carlo and analytical models of neutron detection with organic scintillation detectors. *Nuclear Instruments and Methods in Physics Research Section A: Accelerators, Spectrometers, Detectors and Associated Equipment*, 582, 2007.

[96] C. S. Sosa et al. Energy resolution experiments of conical organic scintillators and a comparison with geant4 simulations. *Nuclear Instruments and Methods in Physics Research Section A: Accelerators, Spectrometers, Detectors and Associated Equipment*, 898, 2018.

[97] David A. Dixon and H. Grady Hughes. Validation of the mcnp6 electron-photon transport algorithm: multiple-scattering of 13- and 20-mev electrons in thin foils. *ICRS-13 RPSD-2016, 13th International Conference on Radiation Shielding 19th Topical Meeting of the Radiation Protection and Shielding Division of the American Nuclear Society - 2016*, 153, 2017.

[98] A. Galindo-Tellez et al. Design and calibration of an optically segmented single volume scatter camera for neutron imaging. *Instrumentation and Detectors*, 2021.